QSO MUSEUM I: a sample of 61 extended Ly α-emission nebulae surrounding $z \sim 3$ quasars

Fabrizio Arrigoni Battaia [ID],[1,2]★ Joseph F. Hennawi,[2,3] J. Xavier Prochaska,[4,5] Jose Oñorbe,[6] Emanuele P. Farina [ID],[3] Sebastiano Cantalupo[7] and Elisabeta Lusso [ID][8]

[1]*European Southern Observatory, Karl-Schwarzschild-Str. 2, D-85748 Garching bei München, Germany*
[2]*Max-Planck-Institut für Astronomie, Königstuhl 17, D-69117 Heidelberg, Germany*
[3]*Department of Physics, Broida Hall, University of California, Santa Barbara, CA 93106-9530, USA*
[4]*Department of Astronomy and Astrophysics, University of California, 1156 High Street, Santa Cruz, CA 95064, USA*
[5]*University of California Observatories, Lick Observatory, 1156 High Street, Santa Cruz, CA 95064, USA*
[6]*Institute for Astronomy, University of Edinburgh, Royal Observatory Blackford Hill, Edinburgh EH9 3HJ, UK*
[7]*Department of Physics, ETH Zurich, CH-8093 Zurich, Switzerland*
[8]*Centre for Extragalactic Astronomy, Department of Physics, Durham University, South Road, Durham DH1 3LE, UK*

ABSTRACT

Motivated by the discovery of rare enormous Lyman α nebulae (ELAN) around $z \sim 2$ quasars, we initiated a long-term campaign with the MUSE/VLT instrument to directly uncover the astrophysics of the gas around quasars. We present here the first 61 targets under the acronym QSO MUSEUM. These quasars are characterized by a median redshift $z = 3.17$, absolute i magnitude in the range $-29.67 \leq M_i(z = 2) \leq -27.03$, and different levels of radio-loudness. This sample unveils diverse specimens of Ly α nebulosities extending for tens of kpc around these quasars (average maximum projected distance of 80 kpc) above a surface brightness SB $> 8.8 \times 10^{-19}$ erg s^{-1} cm^{-2} arcsec$^{-2}(2\sigma)$. The bulk of the Ly α emission is within $R < 50$ kpc, and is characterized by relatively quiescent kinematics, with average velocity dispersions $\langle \sigma_{\mathrm{Ly}\alpha} \rangle < 400$ km s^{-1}. Therefore, the motions within all these Ly α nebulosities have amplitudes consistent with gravitational motions expected in dark matter haloes hosting quasars at these redshifts, possibly reflecting the complexity in propagating a fast wind on large scales. Our current data suggest a combination of photoionization and resonant scattering as powering mechanisms of the Ly α emission. We discover the first $z \sim 3$ ELAN, confirming a very low probability (~ 1 per cent) of occurrence of such systems at these redshifts. Finally, we discuss the redshift evolution currently seen in extended Ly α emission around radio-quiet quasars from $z \sim 3$ to $z \sim 2$, concluding that it is possibly linked to a decrease of cool gas mass within the circumgalactic medium of quasars from $z \sim 3$ to $z \sim 2$, and thus to the balance of cool versus hot media. Overall, QSO MUSEUM opens the path to statistical surveys targeting the gas phases in quasars' haloes along cosmic times.

Key words: galaxies: haloes – galaxies: high-redshift – intergalactic medium – quasars: emission lines – quasars: general – cosmology: observations.

1 INTRODUCTION

In the current paradigm of structure formation, most of the baryons at high redshift ($z \gtrsim 1.5$; Meiksin 2009 and references therein) are distributed in a web of diffuse filamentary structures in which galaxies form and evolve. The complex interplay between this rich reservoir of gas and the galaxies themselves is still a matter of

investigation, e.g. importance and strength of feedback from active galactic nuclei (AGNs), existence of a cold mode of accretion on to galaxies, astrophysics of galactic outflows, build up of supermassive black holes in short time-scales, angular momentum evolution (e.g. Brooks et al. 2009; Dekel et al. 2009; Di Matteo et al. 2012; Dubois et al. 2013; Shen et al. 2013; Anglés-Alcázar et al. 2014; Feng et al. 2014; Woods et al. 2014; Nelson et al. 2016; Stewart et al. 2017; Obreja et al. 2018). Intergalactic and circumgalactic large-scale structures thus encode fundamental information to test our current galaxy evolution theories.

★ E-mail: farrigon@eso.org

So far, whether one focuses on large scales, i.e. on the inter-galactic medium (IGM), or on smaller scales, i.e. on the hundreds of kpc close to galaxies often referred to as the circumgalactic medium (CGM), the strongest constraints on the physical properties of these diffuse gas phases are obtained by analysing absorption features along background sightlines (e.g. Bergeron et al. 2002; Croft et al. 2002; Hennawi et al. 2006a; Hennawi & Prochaska 2007; Tumlinson et al. 2011; Farina et al. 2013; Rudie et al. 2013; Prochaska, Hennawi & Simcoe 2013a; Farina et al. 2014; Lee et al. 2014; Turner et al. 2014). Direct imaging of the same gas phases greatly complement these absorption studies, allowing a spatial, morphological, physical, and kinematical characterization, which is simply not possible with sparse 1D information inherent to the absorption technique. Yet, predicted to be diffuse, the IGM and CGM are expected to be hard to detect in emission ($SB_{Ly\alpha} \sim 10^{-20}$ erg s^{-1} cm^{-2} arcsec^{-2}; e.g. Lowenthal et al. 1990; Gould & Weinberg 1996; Bunker, Marleau & Graham 1998; Rauch et al. 2008).

Nevertheless, recently, the deployment of new advanced integral field spectrographs on 10-m class telescopes, i.e. the Multi-Unit Spectroscopic Explorer (MUSE; Bacon et al. 2010) on the ESO/VLT (European Southern Observatory/Very Large Telescope) and the Keck Cosmic Web Imager (KCWI; Morrissey et al. 2012), opened up the possibility of routinely performing such an experiment by targeting very low levels of surface brightness (SB). Indeed, the latest observations are able to directly studying in emission at least the CGM of galaxies with reasonable observational times (~tens of hours). In particular, these observations usually show extended Lyα emission on scales of tens of kpc around the targeted $z \gtrsim 1.7$ galaxies (Wisotzki et al. 2016; Leclercq et al. 2017), opening up a new parameter space for the study of the CGM gas phases, and ultimately of galaxy evolution.

Even before the advent of the current new instrumentations, it has been shown that such extended Lyα emission on CGM scales is more easily detected around high-redshift quasars or AGNs. In this case, the Lyα emission was detected around most of the objects (50−70 per cent) on $R < 50$ kpc (e.g. Hu & Cowie 1987; Heckman et al. 1991a,b; Fynbo, Møller & Warren 1999; Møller et al. 2000; Weidinger et al. 2005; Christensen et al. 2006; Zafar et al. 2011; North et al. 2012; Hennawi & Prochaska 2013; Arrigoni Battaia et al. 2016), extending up to $R > 100$ kpc in a few rare bright cases known as Enormous Lyman α Nebulae (ELAN; Cantalupo et al. 2014; Hennawi et al. 2015; Cai et al. 2017; Arrigoni Battaia et al. 2018; Cai et al. 2018). The ELAN are indeed structures characterized by high observed surface brightnesses ($SB_{Ly\alpha} > 10^{-17}$ erg s^{-1} cm^{-2} arcsec^{-2}) spanning continuously out to hundreds of kpc, and thus resulting in luminosities $L_{Ly\alpha} > 10^{44}$ erg s^{-1} (Cai et al. 2017). The comparison between all these pioneering observations however is hampered by (i) the heterogeneity of the technique used (longslit spectroscopy, narrow-band imaging, integral-field spectroscopy), (ii) by the lower and different sensitivities inherent to the previous observational instruments ($SB_{limit} >$ few $\times$ 10^{-18} erg s^{-1} cm^{-2} arcsec^{-2} for some works and $SB_{limit} \gtrsim 10^{-17}$ erg s^{-1} cm^{-2} arcsec^{-2} for others), (iii) by uncertainties in the redshift of the targeted quasars, and (iv) by the difficulties in achieving a clean removal of the unresolved emission from the quasar, which can easily outshine the faint large-scale emission (e.g. Møller 2000).

The advent of the aforementioned new sensitive IFU (integral field unit) instruments together with the discoveries of the ELAN have motivated intense research on quasar haloes, and have resulted in frequent new clear detections of the cool CGM gas.

Overall, mainly due to the new sensitivities achieved ($<10^{-18}$ erg s^{-1} cm^{-2} arcsec^{-2}), recent studies now routinely show detections on $R \sim 50$ kpc around $z \gtrsim 3$ quasars (e.g. Husband et al. 2015; Borisova et al. 2016; Fumagalli et al. 2016; Ginolfi et al. 2018), i.e. the redshift range for which Lyα is visible with MUSE. In very rare cases these newly discovered Lyα nebulosities at $z \sim 3$ match the observed SB and extent of the ELAN previously unveiled at $z \sim 2$ (Arrigoni Battaia et al. 2018).

In the presence of a quasar, the detected Lyα emission on halo scales has been usually explained as (i) recombination radiation produced after quasar photoionization (a.k.a. fluorescence; e.g. Weidinger, Møller & Fynbo 2004; Weidinger et al. 2005; Hennawi & Prochaska 2013; Cantalupo et al. 2014; Arrigoni Battaia et al. 2015; Borisova et al. 2016), and/or (ii) Lyα photons resonantly scattered within the gas distribution surrounding the quasar (e.g. Hennawi & Prochaska 2013; Cantalupo et al. 2014; Borisova et al. 2016), and/or (iii) recombination radiation produced after photoionization by several sources, e.g. quasar and active companions (e.g. Husband et al. 2015; Arrigoni Battaia et al. 2018; Husemann et al. 2018). A clear determination of the contribution from the different mechanisms cannot be easily achieved by using only the information enclosed in the Lyα emission. Indeed Lyα photons within the CGM gas are likely affected by resonant scattering (e.g. Dijkstra 2017; Gronke et al. 2017 and references therein), which could lead to strong modification of the Lyα spectral shape (e.g. Dijkstra 2017 and references therein), and the relative strength of the Lyα line with respect to other diagnostics (e.g. Neufeld 1990). Notwithstanding these challenges, observations of the extended Lyα emission – together with the aforementioned absorption studies (e.g. Prochaska & Hennawi 2009; Prochaska et al. 2013a; Prochaska, Lau & Hennawi 2014; Lau, Prochaska & Hennawi 2018) – currently paint a scenario in which quasar's haloes are hosting a large reservoir of cool ($T \sim 10^4$ K) gas. This gas is possibly tracing a complex set of astrophysical processes: gas/substructures infalling on to the central quasar (e.g. Hu et al. 1991; Weidinger et al. 2004; Arrigoni Battaia et al. 2018); strong turbulences or outflows (e.g. Ginolfi et al. 2018); interactions between substructures (e.g. Hu et al. 1991; Husband et al. 2015; Arrigoni Battaia et al. 2018; Husemann et al. 2018); large-scale filaments (Cantalupo et al. 2014).

Further, in the case of ELANe there are evidences that the Lyα emitting gas on hundreds of kpc is composed by a population of cool and dense (volume density $n_H > 1$ cm^{-3}) clumps (Cantalupo et al. 2014). Indeed, if one assumes an ELAN to be powered by the radiation from the associated brightest quasar, the high levels of Lyα emission together with the current stringent limits on the He II/Lyα ratio can be matched by photoionization models only if very high densities ($n_H \gtrsim 3$ cm^{-3}; thus low ionization parameters $\log U \lesssim -2$), and low column densities ($N_H \lesssim 10^{20}$ cm^{-2}) are used (Arrigoni Battaia et al. 2015, 2018). The same framework thus requires the clumps to have compact sizes $R \equiv N_H/n_H \lesssim 20$ pc (Arrigoni Battaia et al. 2015; Hennawi et al. 2015; Arrigoni Battaia et al. 2018). Current simulations are not able to achieve the resolutions needed to resolve such clumps in the CGM of galaxies, predicting low densities ($n_H \sim 10^{-2}$–10^{-3} cm^{-3}) for such a medium (see discussions in Cantalupo et al. 2014; Hennawi et al. 2015). This tension between observations and simulations motivated new research on hydrodynamical instabilities (e.g. Mandelker et al. 2016). In particular, very high resolution idealized hydrodynamical (Mc-Court et al. 2018) and magneto-hydrodynamical (Ji, Oh & McCourt 2018) simulations have shown that a mist of cool gas clouds could

form and survive in the halo of galaxies, possibly explaining the high densities required by the observed levels of Ly α emission around quasars.

Also, the effects of the quasar activity (e.g. radiation, outflows) on the diffuse gas phases and on the production of Ly α photons is not fully understood, and could lead to effects on the morphology and physical properties of the surrounding gas distribution. Extreme examples of what a powerful AGN can do are the high-redshift radio galaxies (HzRGs), whose powerful radio jet and UV radiation clearly alter the surrounding gas (e.g. Nesvadba et al. 2017; Silva et al. 2018). These objects show extended Ly α emission with active kinematics (FWHM > 1000 km s^{-1}) associated with the radio emission, but a more extended (100 kpc scales) quiescent (FWHM < 700 km s^{-1}) gas phase consistent with gravitational motions (e.g. van Ojik et al. 1997; Villar-Martín et al. 2002; Humphrey et al. 2007; Villar-Martín et al. 2007), and/or large-scale structures (Vernet et al. 2017). This quiescent large-scale gas phase is similar to what is seen around quasars (Husband et al. 2015; Borisova et al. 2016; Arrigoni Battaia et al. 2018). Understanding the effects of AGN disruption mechanisms is fundamental given that these are invoked in cosmological simulations to modify the gas properties around and within massive galaxies to match observational constraints, e.g. star formation, halo mass versus stellar mass relation (e.g. Silk & Rees 1998; Sijacki et al. 2007; Booth & Schaye 2009; Richardson et al. 2016).

In this context, we have started to survey the $z \sim 3$ quasar population with the main aim to characterize (i) the physical properties of the CGM/IGM in emission associated with such expected massive dark-matter haloes ($M_{DM} \sim 10^{12.5}$ M$_\odot$, White et al. 2012; Trainor & Steidel 2012a), and (ii) the frequency of detection of ELAN (SB$_{Ly\alpha}$ $\gtrsim 10^{-17}$ erg s^{-1} cm^{-2} arcsec^{-2} out to 100 kpc). In this paper we focus on presenting the observations at the Ly α transition for the first 61 targeted quasars under the acronym QSO MUSEUM (*Q*uasar *S*napshot *O*bservations with *MU*se: *S*earch for *E*xtended *U*ltraviolet e*M*ission). This work is part of an ongoing multitechnique and multiwavelength effort to unveil any dependence on the nature of each system (e.g. geometry, environment, radio activity, luminosity) in the detection and properties of extended gaseous structures.

This work is structured as follows. In Section 2, we describe our observations and data reduction. In Section 3 we explain our analysis procedures, and the current uncertainties on the systemic redshifts of the quasars in our sample. In Section 4, we present the observational results. In particular, we reveal the discovery of extended Ly α emission around our targeted quasars, and show their diverse morphologies, individual radial profiles, stacked profiles, average covering factor for the Ly α emission, compact line emitters associated with the targeted systems, kinematics, and spectral shape of the Ly α emission. In Section 5 we discuss our results in light of the current statistics for extended Ly α emission around quasars, and the usually invoked powering mechanisms. Finally, Section 6 summarizes our findings.

Throughout this paper, we adopt the cosmological parameters $H_0 = 70$ km s^{-1} Mpc^{-1}, $\Omega_M = 0.3$ and $\Omega_\Lambda = 0.7$. In this cosmology, 1 arcsec corresponds to about 7.6 physical kpc at $z = 3.17$ (median redshift for our sample). All magnitudes are in the AB system (Oke 1974), and all distances are proper, unless otherwise specified.

2 OBSERVATIONS AND DATA REDUCTION

The survey QSO MUSEUM has been designed to target the population of $z \sim 3$ quasars with the aim of (i) uncovering additional ELANe, similar to Cantalupo et al. (2014) and Hennawi et al.

(2015), (ii) conducting a statistical census to determine the frequency of the ELAN phenomenon, (iii) studying the size, luminosity, and covering factor of the extended Ly α emission, and any relationship with quasar properties (e.g. luminosity, radio activity), (iv) looking for any evolutionary trend by comparing this sample with the $z \sim 2$ quasar population (e.g. Arrigoni Battaia et al. 2016). We have selected the targets from the last edition (13th) of the catalogue by Véron-Cetty & Véron (2010), and SDSS-DR12 Quasar catalogue (Pâris et al. 2017), starting from the brightest quasars with $z < 3.4$ not targeted by the MUSE Guaranteed Time Observation (GTO) team (i.e. Borisova et al. 2016). In addition, to facilitate detection of the expected low surface brightness features, we require our targeted fields (i) to have low extinction, i.e. $A_V < 0.2$ mag, computed from the maps of Schlegel, Finkbeiner & Davis (1998),[1] and (ii) to be devoid of stars brighter than 13 mag. Also, we gave higher priority for observations to the less crowded fields. For this purpose, we have visually inspected the density of sources using the optical catalogues available at the time of selection, in particular, SDSS-DR12 (Alam et al. 2015), DSS2 (Lasker et al. 1996), and USNO-A2/B1 (Monet 1998; Monet et al. 2003) catalogues.

To conduct the survey QSO MUSEUM, we have been awarded so far a total of 111 h, of which 68 per cent have been executed. The current resulting sample comprises 61 quasars[2] with *i*-band magnitude in the range $17.4 < i < 19.0$ (median 18.02), or absolute *i*-band magnitude normalized at $z = 2$ (Ross et al. 2013) in the range $-29.67 \leq M_i (z = 2) \leq -27.03$ (or absolute magnitude at rest frame 1450 Å in the range $-28.29 \leq M_{1450} \leq -25.65$), and the redshift spanning $3.03 < z < 3.46$ (median 3.17). Our survey thus expands on the work by Borisova et al. (2016), both in number of targeted sources (19 versus 61) and by encompassing fainter sources.[3] In Table 1 we summarize the information for our obtained sample. Of the 61 quasars targeted, 15 (or 25 per cent) are detected in radio, and fulfill the most used radio-loudness criteria $R = f_{\nu, 5\,GHz}/f_{\nu, 4400} > 10$ (Kellermann et al. 1989).[4] Some of these radio-loud objects have been covered by the Faint Images of the Radio Sky at Twenty-centimeters (FIRST) survey (Becker, White & Helfand 1994) with a resolution of 5 arcsec. This resolution is sufficient to start comparing the location/morphology of extended Ly α emission and radio emission (see Section 5.3 and Appendix B).

The observations for QSO MUSEUM have been acquired in service-mode under the ESO programmes 094.A-0585(A), 095.A-0615(A/B), and 096.A-0937(B) with the MUSE (Bacon et al. 2010) on the VLT 8.2m telescope YEPUN (UT4) during 'dark time'. All the observations consisted of exposures of 900 s each, rotated by 90 deg with respect to each other. The survey has been designed to get a total exposure time on source per object of 45 min. However, SDSS J0817+1053 and SDSS J1342 + 1702 have only two usable exposures. In addition, we integrated longer on UM 683 (180 min)

---

[1] We are aware of new extinction maps obtained by Schlafly & Finkbeiner (2011). However, here we decided to rely on Schlegel et al. (1998) as their values are on average 14 per cent higher for our sample, thus making our selection more conservative.

[2] Additional four fields have been observed during our programmes, i.e. Q 1346 + 001, Q 0106-4137, Q 0029-3857, Q 0153-3951, but these sources happen to be stars and not quasars as listed in the last edition (13th) of the catalogue by Véron-Cetty & Véron (2010).

[3] The faintest target in Borisova et al. (2016) has $M_i(z = 2) = -28.23$.

[4] The fraction of radio-loud objects in our sample is thus larger than the value for the overall quasar population ($\sim 10 - 20$ per cent; Kellermann et al. 1989; Ivezić et al. 2002). We initially aimed at building a characteristic sample of the quasar population, but our project has not been fully completed.

Table 1. QSO MUSEUM: the sample.

ID	Quasar	$z_{systemic}^a$	$z_{peak QSO Ly\alpha}^b$	$z_{peak Ly\alpha}^c$	i^d (mag)	$M_i(z=2)^e$ (mag)	M_{1450} (mag)	Radio flux^f (mJy)	A_V^g (mag)
1	SDSS J2319-1040	3.166	3.166	3.172	18.17	−28.61	−27.22	<0.396	0.09
2	UM 24	3.133	3.161	3.163	17.08	−29.67	−28.29	<0.396	0.10
3	J 0525-233	3.110	3.114	3.123	17.71	−29.04	−27.64	398.0*	0.10
4	Q-0347-383	3.219	3.227	3.230	17.63	−29.18	−27.80	<0.210*	0.03
5	SDSS J0817+1053	3.320	3.323	3.336	18.08	−28.82	−27.43	<0.381	0.08
6	SDSS J0947+1421	3.029	3.039	3.073	17.04	−29.65	−28.25	<0.423	0.09
7	SDSS J1209+1138	3.117	3.117	3.126	17.63	−29.12	−27.73	<0.432	0.08
8	UM683	3.132	3.125	3.132	18.59	−28.17	−26.78	<0.450*	0.09
9	Q-0956+1217	3.301	3.306	3.316	17.48	−29.40	−28.01	<0.414	0.11
10	SDSS J1025+0452	3.227	3.244	3.243	17.92	−28.89	−27.51	<0.435	0.07
11	Q-N1097.1	3.078	3.101	3.099	18.81	−27.92	−26.52	<0.180*	0.07
12	SDSS J1019+0254	3.376	3.384	3.395	18.26	−28.66	−27.29	<0.432	0.12
13	PKS-1017+109	3.164	3.166	3.167	18.13	−28.65	−27.26	<0.438	0.10
14	SDSS J2100-0641	3.126	3.138	3.136	18.29	−28.46	−27.07	<0.471	0.10
15	SDSS J1550+0537	3.141	3.143	3.147	18.08	−28.68	−27.29	<1.458	0.19
16	SDSS J2348-1041	3.142	3.186	3.190	18.17	−28.58	−27.20	<0.426	0.16
17	SDSS J0001-0956	3.340	3.349	3.348	18.56	−28.35	−26.97	<0.447^l	0.10
18	SDSS J1557+1540	3.265	3.276	3.288	18.46	−28.38	−27.00	<0.429	0.13
19	SDSS J1307+1230	3.188	3.213	3.229	17.58	−29.20	−27.83	<0.408	0.12
20	SDSS J1429-0145	3.395	3.419	3.425	17.90	−29.02	−27.66	<0.786	0.08
21	CT-669	3.219	3.219	3.218	18.13	−28.68	−27.30	<0.990*	0.16
22	Q-2139-4434	3.176	3.229	3.229	17.95	−28.82	−27.45	–	0.11
23	Q-2138-4427	3.061	3.143	3.142	18.13	−28.57	−27.18	–	0.06
24	SDSS J1342+1702	3.062	3.055	3.053	18.55	−28.17	−26.76	<0.414	0.06
25	SDSS J1337+0218	3.307	3.342	3.344	18.37	−28.51	−27.13	<0.432	0.05
26	Q-2204-408	3.181	3.178	3.179	17.17	−29.62	−28.23	–	0.07
27	Q-2348-4025	3.318	3.332	3.334	17.98	−28.91	−27.53	–	0.04
28	Q-0042-269	3.344	3.358	3.357	19.10	−27.81	−26.43	<0.060*	0.08
29	Q-0115-30	3.180	3.221	3.221	17.95	−28.83	−27.45	<0.540*	0.04
30	SDSS J1427-0029	3.357	3.359	3.354	18.27	−28.67	−27.27	<0.513	0.05
31	UM670	3.131	3.204	3.203	17.64	−29.10	−27.73	<0.450	0.14
32	Q-0058-292	3.069	3.098	3.101	18.53	−28.19	−26.79	<3.570*	0.12
33	Q-0140-306	3.125	3.133	3.132	18.33	−28.43	−27.03	3.7*^{m}	0.08
34	Q-0057-3948	3.223	3.242	3.251	19.49	−27.32	−25.94	<0.150*	0.05
35	CTS-C22.31	3.247	3.244	3.246	19.50	−27.33	−25.95	–	0.05
36	Q-0052-3901A	3.197	3.190	3.203	19.10	−27.69	−26.31	27.3^n	0.06
37	UM672	3.130	3.128	3.127	18.52	−28.24	−26.85	46.0*	0.04
38	SDSS J0125-1027	3.348	3.351	3.319	18.24	−28.68	−27.29	<0.438	0.04
39	SDSS J0100+2105	3.100	3.096	3.097	18.15	−28.59	−27.19	<2.22*	0.09
40	SDSS J0250-0757	3.342	3.337	3.336	18.19	−28.72	−27.34	<0.471	0.09
41	SDSS J0154-0730	3.321	3.334	3.337	18.66	−28.24	−26.85	<0.399	0.13
42	SDSS J0219-0215	3.042	3.034	3.036	18.29	−28.42	−27.01	<0.492	0.06
43	CTSH22.05	3.087	3.124	3.127	18.66	−28.06	−26.67	–	0.08
44	SDSS J2321+1558	3.197	3.233	3.241	18.29	−28.50	−27.12	<1.770*	0.08
45	FBQS J2334-0908	3.312	3.359	3.361	17.96	−28.93	−27.54	27.65	0.10
46	Q2355+0108	3.385	3.389	3.395	17.61	−29.32	−27.94	<0.423	0.09
47	6dF J0032-0414	3.156	3.154	3.162	18.88	−27.89	−26.50	34.55	0.08
48	UM679	3.197	3.204	3.215	18.77	−28.02	−26.64	<1.020*	0.14
49	PKS0537-286	3.109	3.139	3.141	18.93	−27.81	−26.42	862.2*	0.09
50	SDSS J0819+0823	3.197	3.213	3.205	18.33	−28.46	−27.08	<0.423	0.08
51	SDSS J0814+1950	3.138	3.133	3.137	18.74	−28.02	−26.63	4.45	0.08
52	SDSS J0827+0300	3.144	3.137	3.137	18.09	−28.68	−27.29	7.64	0.12
53	SDSS J0905+0410	3.149	3.152	3.165	19.73	−27.03	−25.65	194.64	0.16
54	S31013+20	3.109	3.108	3.108	19.19	−27.56	−26.16	727.01	0.12
55	SDSS J1032+1206	3.188	3.191	3.195	18.66	−28.13	−26.75	2.29	0.07
56	TEX1033+137	3.089	3.090	3.097	18.09	−28.64	−27.24	102.52^o	0.10
57	SDSS J1057-0139	3.406	3.453	3.452	18.40	−28.51	−27.16	21.13	0.11
58	Q1205-30	3.037	3.048	3.047	17.95	−28.75	−27.34	<0.660*	0.14
59	LBQS1244+1129	3.118	3.155	3.157	18.19	−28.55	−27.17	<0.408	0.19
60	SDSS J1243+0720	3.183	3.178	3.178	19.16	−27.63	−26.24	2.29	0.11
61	LBQS1209+1524	3.061	3.059	3.075	18.02	−28.69	−27.29	<0.450	0.07

Notes. ^{a}Quasar systemic redshift from peak of C IV line, correcting for the expected shift (Shen et al. 2016). The intrinsic uncertainty on this correction is ∼415 km s^{-1} and dominates the error budget ($\Delta z \approx$ 0.007).
^{b}Redshift corresponding to the peak of the Ly α emission in the observed spectrum of each quasar.
^{c}Redshift of the nebulosities estimated as flux-weighted centroid of the Ly α emission for a circular aperture with a diameter of 3 arcsec, at the peak of the SB map of each nebula. As we masked the 1 arcsec × 1 arcsec region used to normalize the PSF, the peaks are always at >1 arcsec projected distance from the quasar position.
^{d}Extracted from our data using the SDSS filter transmission curve and a circular aperture with a diameter of 3 arcsec. The average uncertainty is ∼5 per cent.
^{e}Absolute *i*-band magnitude normalized at $z = 2$ following Ross et al. (2013).
^{f}Integrated flux at 1.4 GHz from the FIRST survey for northern sources or peak flux at 1.4 GHz from the NRAO VLA Sky Survey (NVSS; Condon et al. 1998) for the southern sources (indicated by *). The six sources with Dec<−40 are currently not covered by any radio survey. For the non-detections in each survey, and thus currently considered radio-quiet objects, we report the 3 × rms in mJy beam^{-1} from each catalogue. All the detected sources are radio-loud following the most used definition by Kellermann et al. (1989), i.e. $R = f_{\nu, 5GHz}/f_{\nu, 4400} > 10$.
^{g}Extinction from Schlegel et al. (1998).
^{l}This quasar has a radio source of 50.25 mJy (integrated flux) at ≈13.5 arcsec, but likely not physically associated (Appendix B).
^{m}The radio source is at ≈8 arcsec from the quasar.
^{n}The radio source is at ≈2.3 arcsec from the quasar.
^{o}This source has two lobes separated by ≈8.5 arcsec (Appendix B). We report the sum of the integrated flux of the two lobes.

and UM 672 (90 min) motivated by the extended Ly α emission already clearly detected in the preliminary reduction using the v1.0 MUSE pipeline (Weilbacher et al. 2014) at the time of first data acquisition. For the same reason, the quasar PKS 1017 + 109 has been observed for additional 4.5 h as presented in Arrigoni Battaia et al. (2018).

The observations were carried out in weather conditions classified by ESO as clear (CL; 45 per cent of the objects), photometric (PH; 27 per cent), clear with high-wind (CL-WI; 18 per cent), photometric with high humidity (PH-WI; 5 per cent), photometric with high-wind (PH-WI; 3 per cent), and thin (TN; 2 per cent). The average (median) seeing of these obsServations is 1.07 arcsec (0.98 arcsec) (FWHM of a Moffat profile computed from the white-light image obtained by collapsing the final MUSE datacube for each target), which is great given the any-seeing nature of our programmes. In Table 2 we summarize the observation log for our survey.

We have reduced the data using the MUSE pipeline recipes v1.4 (Weilbacher et al. 2014). Specifically, we have performed bias subtraction, flat-fielding, twilight and illumination correction, and wavelength calibration using this software. In addition, the pipeline flux-calibrate each exposure using a spectrophotometric standard star observed during the same night of each individual observing block. To improve the flat-fielding and to enable the detection of very low surface brightness signals, we have performed a flat-fielding correction and subtract the sky with the procedures `CubeFix` and `CubeSharp` within the CUBEXTRACTOR package (Cantalupo, in preparation; Borisova et al. 2016). We combined the individual exposures using an average 3σ-clipping algorithm. To improve the removal of self-calibration effects, we applied a second time `Cube-Fix` and `CubeSharp`. In this way, we are left with a final science datacube and a variance datacube. The latter has been obtained by taking into account the propagation of errors for the MUSE pipeline and during the combination of the different exposures. The variance is then rescaled by a constant factor to take into account the correlated noise as done in Borisova et al. (2016). The final MUSE datacubes result in an average 2σ surface brightness limit of $SB_{Ly\alpha} = 8.8 \times 10^{-19}$ erg s^{-1} cm^{-2} arcsec^{-2} (in 1 arcsec^2 aperture) in a single channel (1.25 Å) at the wavelength of the Ly α line for the extended emission around each quasar. The deepest narrow-band (NB) studies in the literature usually use NB filters with FWHM~30 Å. For comparison, our datacubes have an average 2σ surface brightness limit of $SB_{Ly\alpha} = 4.2 \times 10^{-18}$ erg s^{-1} cm^{-2} arcsec^{-2} (in 1 arcsec^2 aperture) in NB images of 30 Å, centred at the Ly α line for the extended emission around each quasar. In Table 2 we list these SB limits for each datacube.[5]

3 DETECTING LARGE-SCALE EMISSION ASSOCIATED WITH A QUASAR

As many works in the literature have illustrated (e.g. Hu & Cowie 1987; Heckman et al. 1991a; Bergeron et al. 1999; Møller 2000; Hennawi & Prochaska 2013; Husemann et al. 2013; Arrigoni Battaia et al. 2016), the detection of extended emission around a quasar inevitably requires that one removes the unresolved emission from the quasar itself (continuum and line emission) and the contribution of any other continuum sources. To perform these operations and to

---

extract the extended emission from each of the MUSE datacubes, we rely on the same procedures described in Borisova et al. (2016), which we briefly summarize in the following section, while leaving the presentation of the results to Section 4. We use this approach to allow for a one-to-one comparison with that work, and to facilitate the creation of a homogeneous sample.

3.1 Empirical point-spread-function subtraction, continuum source subtraction, and extraction of extended emission

The point spread function (PSF) of the quasar has been subtracted with the `CubePSFSub` method within CUBEXTRACTOR (Cantalupo, in preparation). The algorithm obtains the PSF of the quasar as pseudo-NB images of user-defined wavelength ranges within the MUSE datacube. For each wavelength range, the empirical PSF is then rescaled to the flux within 5 × 5 pixels (1 arcsec × 1 arcsec) around the quasar position and subtracted from a circular region with a radius of about five times the seeing. These choices of normalization are driven by the fact that we expect the quasar to dominate the flux on 1 arcsec × 1 arcsec (comparable to the seeing of our observations), and by the fact that the quasar PSF at 5 × the seeing (or about ~40 kpc) reaches the noise level in our observations (e.g. see also Arrigoni Battaia et al. 2016; Borisova et al. 2016). Here we use the same wavelength ranges as in Borisova et al. (2016) to construct the pseudo-NB images, i.e. 150 spectral pixels (187.5 Å). This method is unsuitable for the study of emission within the region used for the PSF rescaling, as data show complex residuals on these scales (~10 kpc). In particular, this method assumes the quasar to greatly outshine the host galaxy, whose contribution in the central region is thus considered to be negligible.

Subsequently, we have applied the `CubeBKGSub` algorithm within CUBEXTRACTOR to remove any continuum source in the MUSE datacube. This procedure is based on a fast median-filtering approach described in Borisova et al. (2016), and allows us to avoid any contamination from continuum sources in the search for extended line emission associated with each quasar.

We then run CUBEXTRACTOR on each of the PSF and continuum subtracted cubes to select, if any, extended Ly α emission. Specifically, we only use the portion of the cubes at about $\pm11\,000$ km s^{-1} (±150 layers) around the quasar systemic redshift. As Borisova et al. (2016) found Ly α nebulae with a minimum 'volume' of 10 000 connected voxels (volume pixels) above a signal-to-noise ratio S/N > 2 around all of their targets, we first use such selection criteria to identify the Ly α extended emission around our sample. However, we find that some of our targets are not characterized by such large volumes. For this reason, we have then decreased the threshold on the number of connected voxels in steps of 1000 to search for detections. All our targets have a detected Ly α nebula greater than 1000 voxels. We list in Table 3 the number of connected voxels for each of them. These numbers should be considered with caution as, by construction, the extraction process is strongly dependent on the correct determination of the noise in MUSE datacubes. In this respect, we rely on the variance cube produced by our pipeline. This cube is propagated during the reduction steps and then rescaled to take into account the correlated noise (see details in Borisova et al. 2016).

CUBEXTRACTOR generates a 3D mask that includes all the connected voxels satisfying the selection criteria, and which can be used to compute several diagnostic images. First, for each quasar, the 3D mask is used to construct an 'optimally extracted' NB image for the Ly α emission by summing the flux along the wavelength direction for only the voxels selected by this 3D mask. Following Borisova

Table 2. Observation log.

ID	Quasar	RA (J2000)	Dec (J2000)	Seeing[a] (arcsec)	Weather[b]	Exp. T.[c] (min)	SB limit[d]$_{layer}$ (10^{-19} cgs)	SB limit[e]$_{30\,\text{Å NB}}$ (10^{-18} cgs)	UT date (dd/mm/yyyy)	ESO Prog.
1	SDSS J2319-1040	23:19:34.800	−10:40:36.00	1.40	CL-WI	45.	8.2	4.1	14/10/2014	094.A-0585(A)
2	UM 24	00:15:27.400	+06:40:12.00	1.62	CL	45.	8.8	4.2	14/10/2014	094.A-0585(A)
3	J 0525-233	05:25:06.500	−23:38:10.00	0.86	CL	45.	8.5	3.5	17/01/2015	094.A-0585(A)
4	Q-0347-383	03:49:43.700	−38:10:31.00	1.40	CL	45.	7.6	3.7	25/01/2015	094.A-0585(A)
5	SDSS J0817 + 1053	08:17:52.090	+10:53:29.68	1.47	CL	30.	8.0	3.9	14/02/2015	094.A-0585(A)
6	SDSS J0947 + 1421	09:47:34.200	+14:21:17.00	1.21	CL	45.	10.4	4.6	14/02/2015	094.A-0585(A)
7	SDSS J1209 + 1138	12:09:18.000	+11:38:31.00	1.22	CL	45.	8.5	4.2	14/02/2015	094.A-0585(A)
8	UM 683	03:36:26.900	−20:19:39.00	1.05	CL-PH	45.	5.0	2.0	18/02/2015	094.A-0585(A)
					PH-WI	135.			14/08-21/09/2015	095.A-0615(A)
9	Q-0956 + 1217	09:58:52.200	+12:02:45.00	1.12	PH	45.	8.4	4.2	18/02/2015	094.A-0585(A)
10	SDSS J1025 + 0452	10:25:09.600	+04:52:46.00	1.10	PH	45.	8.5	3.7	18/02/2015	094.A-0585(A)
11	Q-N1097.1	02:46:34.200	−30:04:55.00	1.18	PH-HU	45.	10.6	4.2	19/02/2015	094.A-0585(A)
12	SDSS J1019 + 0254	10:19:08.255	+02:54:31.94	1.22	PH-HU	45.	7.4	3.9	19/02/2015	094.A-0585(A)
13	PKS-1017 + 109	10:20:10.000	+10:40:02.00	0.91	PH-HU	45.	8.2	4.2	19/02/2015	094.A-0585(A)
14	SDSS J2100-0641	21:00:25.030	−06:41:45.00	0.85	CL	45.	10.5	4.9	11/06/2015	095.A-0615(B)
15	SDSS J1550 + 0537	15:50:36.806	+05:37:50.07	1.01	CL-WI	45.	10.2	4.1	17/08/2015	095.A-0615(B)
16	SDSS J2348-1041	23:48:56.488	−10:41:31.17	1.72	CL-WI	45.	8.0	3.9	17/08/2015	095.A-0615(B)
17	SDSS J0001-0956	00:01:44.886	−09:56:30.83	1.81	PH-WI	45.	7.8	3.7	17/08/2015	095.A-0615(B)
18	SDSS J1557 + 1540	15:57:43.300	+15:40:20.00	0.81	CL	45.	7.4	4.5	22/05/2015	095.A-0615(A)
19	SDSS J1307 + 1230	13:07:10.200	+12:30:21.00	0.89	CL	45.	8.3	3.8	11/06/2015	095.A-0615(A)
20	SDSS J1429-0145	14:29:03.033	−01:45:19.00	0.79	CL	45.	7.7	3.5	11/06/2015	095.A-0615(A)
21	CT-669	20:34:26.300	−35:37:27.00	0.74	CL	45.	11.9	3.8	11/06/2015	095.A-0615(A)
22	Q-2139-4434	21:42:25.900	−44:20:18.00	1.02	CL	45.	8.9	4.4	11/06/2015	095.A-0615(A)
23	Q-2138-4427	21:41:59.500	−44:13:26.00	0.81	CL	45.	7.7	3.9	17/06/2015	095.A-0615(A)
24	SDSS J1342 + 1702	13:42:33.200	+17:02:46.00	1.03	CL	30.	10.3	4.4	08/07/2015	095.A-0615(A)
25	SDSS J1337 + 0218	13:37:57.900	+02:18:21.00	0.75	CL-PH	45.	14.2	3.5	09/07/2015	095.A-0615(A)
26	Q-2204-408	22:07:34.300	−40:36:57.00	0.84	TN	45.	25.3	15.8	13/07/2015	095.A-0615(A)
27	Q-2348-4025	23:51:16.100	−40:08:36.00	0.87	CL	45.	7.2	3.4	16/07/2015	095.A-0615(A)
28	Q-0042-269	00:44:52.300	−26:40:09.00	0.80	CL	45.	6.8	3.4	25/07/2015	095.A-0615(A)
29	Q-0115-30	01:17:34.000	−29:46:29.00	0.91	CL	45.	7.1	3.6	25/07/2015	095.A-0615(A)
30	SDSS J1427-0029	14:27:55.800	−00:29:51.00	0.95	CL	45.	17.1	12.4	28/07/2015	095.A-0615(A)
31	UM 670	01:17:23.300	−08:41:32.00	0.80	CL	45.	7.5	3.6	28/07/2015	095.A-0615(A)
32	Q-0058-292	01:01:04.700	−28:58:03.00	1.42	CL-WI	45.	7.2	3.6	11/08/2015	095.A-0615(A)
33	Q-0140-306	01:42:54.700	−30:23:45.00	1.39	CL-WI	45.	8.3	3.5	11/08/2015	095.A-0615(A)
34	Q-0057-3948	00:59:53.200	−39:31:58.00	1.09	CL-WI	45.	9.2	3.3	11/08/2015	095.A-0615(A)
35	CTS-C22.31	02:04:35.500	−45:59:23.00	1.18	CL-WI	45.	7.2	3.6	11/08/2015	095.A-0615(A)
36	Q-0052-3901A	00:54:45.400	−38:44:15.00	1.25	CL-WI	45.	7.2	3.4	11/08/2015	095.A-0615(A)
37	UM672	01:34:38.600	−19:32:06.00	1.87	CL	45.	7.2	2.6	07/09/2015	095.A-0615(A)
					CL-WI	45.			04/11/2015	096.A-0937(B)
38	SDSS J0125-1027	01:25:30.900	−10:27:39.00	0.74	CL	45.	7.3	3.7	15/09/2015	095.A-0615(A)
39	SDSS J0100 + 2105	01:00:27.661	+21:05:41.57	0.73	PH	45.	9.5	4.4	17/09/2015	095.A-0615(A)
40	SDSS J0250-0757	02:50:21.800	−07:57:50.00	0.67	PH	45.	7.5	3.6	17/09/2015	095.A-0615(A)
41	SDSS J0154-0730	01:54:40.328	−07:30:31.85	0.75	PH	45.	6.7	3.5	21/09/2015	095.A-0615(A)
42	SDSS J0219-0215	02:19:38.732	−02:15:40.47	0.64	PH	45.	9.3	4.2	21/09/2015	095.A-0615(A)
43	CTSH22.05	01:48:18.130	−53:27:02.00	1.34	CL-WI	45.	7.5	3.8	02/11/2015	096.A-0937(B)
44	SDSS J2321 + 1558	23:21:54.980	+15:58:34.24	1.61	CL	45.	7.7	3.8	04/11/2015	096.A-0937(B)
45	FBQS J2334-0908	23:34:46.400	−09:08:12.24	1.18	CL	45.	7.3	3.7	04/11/2015	096.A-0937(B)
46	Q2355 + 0108	23:58:08.540	+01:25:07.20	1.23	CL	45.	7.4	3.4	04/11/2015	096.A-0937(B)
47	6dF J0032-0414	00:32:05.380	−04:14:16.21	1.59	CL	45.	9.6	3.9	04/11/2015	096.A-0937(B)
48	UM 679	02:51:48.060	−18:14:29.00	0.96	PH	45.	7.0	3.6	18/11/2015	096.A-0937(B)
49	PKS0537-286	05:39:54.267	−28:39:56.00	0.74	PH	45.	6.7	3.5	18/11/2015	096.A-0937(B)
50	SDSS J0819 + 0823	08:19:40.580	+08:23:57.98	0.73	PH	45.	7.7	3.5	15/12/2015	096.A-0937(B)
51	SDSS J0814 + 1950	08:14:53.449	+ 19:50:18.62	0.75	PH	45.	10.2	4.2	12/01/2016	096.A-0937(B)
52	SDSS J0827 + 0300	08:27:21.968	+03:00:54.74	0.96	CL	45.	7.8	3.3	14/01/2016	096.A-0937(B)
53	SDSS J0905 + 0410	09:05:49.058	+04:10:10.15	0.93	CL	45.	7.1	3.2	14/01/2016	096.A-0937(B)
54	S31013 + 20	10:16:44.319	+20:37:47.29	0.92	PH	45.	7.9	3.7	14/01/2016	096.A-0937(B)
55	SDSS J1032 + 1206	10:32:12.886	+12:06:12.83	0.89	CL-WI	45.	7.7	3.7	16/01/2016	096.A-0937(B)
56	TEX1033 + 137	10:36:26.886	+13:26:51.75	0.70	PH	45.	9.0	4.2	17/01/2016	096.A-0937(B)
57	SDSS J1057-0139	10:57:13.250	−01:39:13.79	1.31	PH	45.	11.2	5.4	19/01/2016	096.A-0937(B)
58	Q1205-30	12:08:12.730	−30:31:07.00	0.63	PH	45.	9.2	4.3	09/02/2016	096.A-0937(B)
59	LBQS1244 + 1129	12:46:40.370	+11:13:02.92	1.45	PH	45.	9.8	4.6	04/03/2016	096.A-0937(B)
60	SDSS J1243 + 0720	12:43:53.960	+ 07:20:15.47	1.29	PH	45.	8.5	3.9	08/03/2016	096.A-0937(B)
61	LBQS1209 + 1524	12:12:32.040	+ 15:07:25.63	1.42	PH	45.	8.9	4.1	17/03/2016	096.A-0937(B)

Notes. [a]Seeing computed from the 'white-light' image of the final MUSE datacubes as FWHM of a Moffat profile.

[b]Sky conditions during observations as from the ESO observations log: PH-photometric; CL-clear; WI-windy; TN-thin cirrus; HU-humid

[c]Exposure time on source (i.e. without overheads).

[d]2σ SB limit in 1 arcsec^2 computed for the layer (1.25 Å) at the redshift of the Ly α emission for each target. The cgs units are erg s^{-1} cm^{-2} arcsec^{-2}.

[e]2σ SB limit in 1 arcsec^2 computed for the 30 Å NB image centred at the redshift of the Ly α emission for each target. The cgs units are erg s^{-1} cm^{-2} arcsec^{-2}.

et al. (2016), a layer of the MUSE cube corresponding to the peak of the Ly α emission has been added as 'background' layer to each 'optimally extracted' NB image. In other words, as the projected field-of-view (FOV) described by the 3D mask does not cover the whole MUSE FOV, we replaced the empty pixels with values from the respective pixels in the layer at the peak of the Ly α emission.

In addition, the 3D masks – and thus only the voxels selected – are also used to compute the first and second moments (in velocity space) of the flux distribution at each spatial location around each quasar. Finally, we have also constructed NB images of 30 Å by collapsing the MUSE cubes centred at the Ly α peak of each nebulosity. Although all this analysis approach can be used to extract

Table 3. QSO MUSEUM: properties of the extended Ly α emission.

ID	Quasar	Luminosity (10^43 erg s^−1)	Area (arcsec^2)	Δλ^a (Å)	Max. Distance^b (arcsec kpc^−1)	α^c	d_{QSO−Neb}^d (arcsec kpc^−1)	φ_{NE}^e (deg)	Voxels^f
1	SDSS J2319-1040	3.17	102.4	36.2	7.37/55.8	0.80	0.29/2.2	−38.8	12 059
2	UM 24	2.57	156.7	32.5	10.32/78.2	0.77	1.17/9.0	−30.4	10 812
3	J 0525-233	1.17	79.5	30.0	9.21/70.1	0.84	1.11/8.4	−1.7	6406
4	Q-0347-383	4.11	177.5	27.5	12.12/91.2	0.80	0.40/3.0	−60.0	16 760
5	SDSS J0817 + 1053	4.99	147.3	36.2	12.98/96.6	0.80	1.43/10.7	−22.9	17 726
6	SDSS J0947 + 1421	2.04	86.2	33.8	11.71/89.5	0.34	3.14/24.1	−83.8	8936
7	SDSS J1209 + 1138	2.32	93.0	32.5	7.97/60.6	0.90	1.71/13.0	−27.8	8793
8	UM683	7.92	274.0	43.8	19.09/145.1	0.64	3.83/29.1	23.9	44 094
9	Q-0956 + 1217	5.34	158.4	50.0	12.50/93.2	0.73	1.78 / 13.3	−80.0	16 921
10	SDSS J1025 + 0452	18.66	288.9	51.2	14.97/112.5	0.78	1.37/10.3	19.2	50 282
11	Q-N1097.1	2.96	103.1	26.2	10.83/82.6	0.70	0.39 / 3.0	16.8	10 313
12	SDSS J1019 + 0254	3.09	76.7	33.8	10.35/76.6	0.45	1.12/8.3	63.4	9643
13	PKS-1017 + 109	24.87	466.6	47.5	27.28/206.6	0.49	8.50 / 64.4	−28.7	74 865
14	SDSS J2100-0641	2.14	63.0	48.8	8.63/65.6	0.60	0.84/6.4	−82.6	13 645
15	SDSS J1550 + 0537	5.63	133.6	35.0	10.35 / 78.5	0.61	0.61 / 4.7	−41.9	19 547
16	SDSS J2348-1041	2.28	115.6	32.5	8.53/64.5	0.71	0.99/7.5	−8.8	11 316
17	SDSS J0001-0956	10.80	243.1	40.0	13.11/97.5	0.76	1.52/11.3	19.6	34 978
18	SDSS J1557 + 1540	21.83	161.5	52.5	11.33/84.8	0.84	1.10/8.3	68.9	32 057
19	SDSS J1307 + 1230	6.98	189.4	41.2	12.15/91.5	0.87	1.12 / 8.4	−45.3	28 534
20	SDSS J1429-0145	3.55	90.6	41.2	8.61/63.5	0.65	1.60/11.8	84.1	13 666
21	CT-669	10.95	129.7	41.2	9.29/70.0	0.76	0.74 / 5.6	4.0	20 077
22	Q-2139-4434	10.36	172.5	56.2	11.14 / 83.8	0.88	0.68/5.1	−50.3	26 745
23	Q-2138-4427	4.65	91.3	38.8	8.47/64.3	0.82	1.52/ 1.6	−9.1	13 164
24	SDSS J1342 + 1702	2.41	134.5	23.8	15.47/118.5	0.40	2.31/17.7	−44.3	6820
25	SDSS J1337 + 0218	0.52	36.7	27.5	12.41/92.3	0.37	6.91/51.6	−11.8	3235
26	Q-2204-408	1.10	12.5	15.0	3.40/25.7	0.36	0.84 / 6.3	22.5	1192
27	Q-2348-4025	5.13	149.4	40.0	9.44/70.3	0.79	1.14/8.5	−23.6	16 359
28	Q-0042-269	0.96	53.7	22.5	7.94/59.0	0.65	0.77/5.7	69.0	3925
29	Q-0115-30	0.33	28.9	22.5	5.73/43.1	0.65	1.65 / 12.5	79.5	2580
30	SDSS J1427-0029	4.11	34.6	17.5	5.26/39.1	0.71	0.28/2.0	76.3	2676
31	UM670	2.79	115.6	30.0	10.04/75.7	0.75	2.14/16.3	−5.2	11 133
32	Q-0058-292	3.77	161.6	40.0	11.82/90.2	0.60	3.11/23.8	31.2	19 912
33	Q-0140-306	5.10	174.3	37.5	11.74/89.3	0.73	0.58/4.4	−3.8	19 124
34	Q-0057-3948	5.06	160.2	42.5	10.84/81.4	0.69	1.56/11.7	−0.3	19 711
35	CTS-C22.31	5.01	141.7	33.8	11.71/88.0	0.53	1.83/13.7	54.9	18 334
36	Q-0052-3901A	9.81	198.5	40.0	12.31/92.9	0.63	2.56/19.3	40.3	30 792
37	UM672	6.51	117.9	47.5	7.92/60.2	0.95	1.22/ 9.3	−82.6	23 973
38	SDSS J0125-1027	2.25	26.0	21.2	6.65/49.6	0.98	0.45/3.4	61.3	3000
39	SDSS J0100 + 2105	5.02	59.8	38.8	6.42/49.0	0.79	0.38/2.9	−41.4	8969
40	SDSS J0250-0757	2.88	103.9	38.8	11.58/86.2	0.68	0.57/4.3	−78.2	10 602
41	SDSS J0154-0730	3.27	97.2	42.5	9.89/73.6	0.62	0.92/6.9	68.5	13 112
42	SDSS J0219-0215	3.51	101.7	35.0	8.92/68.5	0.53	0.92/7.0	0.3	10 631
43	CTSH22.05	7.36	205.2	47.5	15.60/118.6	0.75	1.51/11.6	−53.0	26 134
44	SDSS J2321 + 1558	0.89	69.2	21.2	9.78/73.5	0.68	1.33/10.0	37.0	5248
45	FBQS J2334-0908	0.67	39.1	25.0	8.67/64.4	0.68	1.11/8.3	−83.0	3382
46	Q2355 + 0108	5.37	208.4	42.5	12.63/93.5	0.75	0.85/6.3	−49.5	24 127
47	6dF J0032-0414	35.73	305.0	47.5	15.28/115.8	0.90	1.09/8.3	−84.0	60 203
48	UM679	4.49	123.1	37.5	10.70/80.6	0.91	0.72/5.4	−40.4	18 594
49	PKS0537-286	4.63	170.0	38.8	10.85/82.4	0.81	0.29/2.2	−26.1	20 509
50	SDSS J0819 + 0823	38.70	342.7	58.8	17.20/129.8	0.56	0.56/4.2	74.4	73 149
51	SDSS J0814 + 1950	2.58	33.8	21.2	6.24/47.4	0.48	0.52/3.9	−2.0	4995
52	SDSS J0827 + 0300	0.84	43.5	21.2	5.53/42.0	0.72	0.85/6.5	81.6	2277
53	SDSS J0905 + 0410	2.79	131.8	41.2	12.01/91.0	0.80	1.23/9.3	−12.7	15 633
54	S31013 + 20	5.63	163.0	47.5	10.74/81.8	0.70	1.10/8.4	−75.1	21 659
55	SDSS J1032 + 1206	1.54	45.6	32.5	5.84/44.1	0.70	0.81/6.2	−1.3	5293
56	TEX1033 + 137	12.67	202.4	37.5	14.16/108.0	0.68	1.37/10.4	−56.3	31 894
57	SDSS J1057-0139	1.70	61.8	33.8	8.92/65.7	0.64	1.28/9.5	34.1	6488
58	Q1205-30	5.78	86.8	40.0	8.92/68.4	0.64	1.88/14.4	−53.2	12 046
59	LBQS1244 + 1129	5.21	138.1	48.8	10.62/80.6	0.73	0.83/6.3	−48.4	17 614
60	SDSS J1243 + 0720	5.07	107.4	45.0	8.66/65.5	0.86	0.23/1.7	−49.1	14 714
61	LBQS1209 + 1524	3.21	156.9	43.8	13.67/104.5	0.60	0.26/2.0	8.7	15 957

Notes. ^a Maximum spectral width of the '3D mask' extracted above the 2σ threshold (see Section 3.1)

^b Maximum distance from the quasar spanned by the Ly α emission within the 2σ isophote.

^c Ratio between the semiminor axis b and semimajor axis a obtained from the second-order moments of the Ly α emission within the 2σ isophote.

^d Distance between the position of the quasar and the flux-weighted centroid of the Ly α emission within the 2σ isophote.

^e Position angle (East of North) of the major axis a obtained from the second-order moments of the Ly α emission within the 2σ isophote.

^f Number of connected voxels above the threshold of S/N = 2 used for the extraction of the nebulosities.

and present any line-emission covered by the MUSE datacubes for our sample (e.g. C IV, He II), in this work we focus only on the Ly α emission and we leave to a future paper (Arrigoni Battaia et al., in preparation) the analysis of additional extended line diagnostics.

3.2 The quasars' systemic redshift

Having an accurate systemic redshift for the targeted quasars is a first fundamental step towards the understanding of the geometry and kinematics of each system (e.g. Weidinger et al. 2005). In particular, a precise determination of the systemic redshift would allow (i) to say if the detected extended line emission is physically related to the studied quasars, or if it is a structure at larger distances in the foreground or background; and (ii) to compare the kinematic information available from observations to simulation studies. However, such precise estimates of the systemic redshift of $z > 2$ quasars are difficult to determine (e.g. Gaskell 1982; Tytler & Fan 1992; Hewett & Wild 2010), and require expensive campaigns of follow-up observations in the near-IR (e.g. McIntosh et al. 1999) or molecular tracers to bring the uncertainties down to the order of few tens of km s^{-1} (e.g. Venemans et al. 2017).

For our sample, at the moment we can only rely on the systemic redshift estimated from the C IV line after correcting for the known luminosity-dependent blueshift of this line with respect to systemic (Richards et al. 2002, 2011; Shen et al. 2016). We have estimated the peak of the C IV line for each of the quasars from our MUSE sample, as specified in Shen et al. (2016), and added to the estimated redshift the luminosity-dependent velocity shift determined following the relation in Shen et al. (2016). In Table 1 we list such systemic redshifts for our targeted quasars. With an intrinsic uncertainty of 415 km s^{-1} for the empirical calibration in Shen et al. (2016), these estimates are not optimal for a detailed studied of our systems in which we expect velocities of the order of hundreds of km s^{-1} to be in place (e.g. Goerdt & Ceverino 2015; Borisova et al. 2016; Arrigoni Battaia et al. 2018). Future efforts are surely needed to better constrain this fundamental parameter. We have indeed initiated a survey in molecular tracers to obtain the systemic redshift of these quasars down to few tens of km s^{-1} uncertainties.

4 RESULTS: DIVERSE SPECIMENS OF EXTENDED LY α EMISSION

In this section we present the results of our QSO MUSEUM survey concerning the detection of extended Ly α emission around the targeted quasars. We stress once again that our data do cover the wavelengths of additional emission lines and continuum diagnostics of which we will present the data in dedicated papers.

4.1 The morphology of the extended Ly α emission

In Fig. 1 we show the atlas of the 61 'optimally extracted' NB images for the Ly α nebulae extracted from the PSF and continuum subtracted datacubes following the procedure mentioned in Section 3.1. In this atlas, each image represents 30 arcsec × 30 arcsec (or about 230 kpc × 230 kpc) around each quasar, whose position before PSF subtraction is indicated by the white crosshair. For simplicity, we identify each target by the index from Table 1, and we report this number in the bottom-right corner of each image.

As it is not feasible to visually assess the noise level in these 'optimally extracted' images, we overlay the S/N contours computed from the propagated variance and taking into account the number of spaxels contributing to each spatial pixel. Specifically, we show the contours for S/N = 2, 4, 10, 20, and 50.

Qualitatively, Fig. 1 shows extended Ly α emission around each system however with different extents, geometries, and substructures. All the objects are characterized by Ly α emission on radii $R \lesssim 50$ kpc (magenta circle on ID 38 in Fig. 1), which appears to be

mostly symmetric on such scales. The average maximum projected distance at which we detect Ly α emission from the targeted quasar down to the 2σ SB limit is 81 kpc or 10.7 arcsec (see Table 3). Objects with asymmetric extended Ly α emission appear to be very rare in our sample. Indeed, we discover only 1 ELAN (around the quasar with ID 13 or PKS 1017 + 109; Arrigoni Battaia et al. 2018).

In all our targets, we are confident that the extended Ly α emission is not due to a systematic effect in underestimating the PSF of each quasar (see also Appendix A). Indeed, in each case, the extended Ly α emission is characterized by a much narrower line profile than the broad Ly α emission of the quasar itself. We show these differences in Fig. 2, where we compare the normalized Ly α line features for each quasar (black) and surrounding nebulosity (red). The quasar and nebulosity spectra reported in these figures have been extracted in circular apertures with 1.5 arcsec radius, and centred at the peak of the unresolved quasar or at the peak of the extended Ly α emission, respectively.

From Fig. 2, it is also evident that some of the extended nebulosities appear to have a shift in redshift with respect to the current uncertain estimate for the quasar systemic. Specifically, we have estimated the redshift for the nebulosities as the location of the flux-weighted centroid of the Ly α emission in these 1D spectra. In Fig. 3 we show the histogram[6] of such velocity shifts between the quasar systemics and the nebulosities, which cover the range $-2000 \text{ km s}^{-1} \leq \Delta v \leq 5980 \text{ km s}^{-1}$, with the quasars with ID 38 (or SDSSJ0125-1027) and ID 23 (or Q-2138-4427) having the bluest and the reddest shift, respectively. Overall, 75 per cent of the nebulosities have their peaks at positive velocity shifts with respect to the systemic of the quasar, making the median value of such shift $\Delta v_{\text{median}} = 782 \text{ km s}^{-1}$.

Additionally, if we instead compute the velocity shift between the nebulosities and the observed peak of the Ly α emission of the quasars themselves ($z_{\text{peak QSO Ly}\alpha}$), we find definitely smaller shifts (orange histogram in Fig. 3). Such velocity displacements cover the range $-2205 \text{ km s}^{-1} \leq \Delta v \leq 2524 \text{ km s}^{-1}$ with the quasars with ID 38 (or SDSSJ0125-1027) and ID 6 (or SDSSJ0947 + 1421) being two outliers with the bluest and the reddest shift, respectively. The median value is $\Delta v_{\text{median}} = 144 \text{ km s}^{-1}$. Thus, intriguingly, even though the peak of the Ly α line of the quasars is highly affected by the presence of multiple absorption features, it appears close in wavelength to the Ly α nebulosities. This occurrence highlights the importance of a precise determination of the quasar systemic, and might be related to the physical mechanism producing the Ly α emission within the nebulosities, and/or to the overall kinematics of the observed gas (see discussion in Section 5.3). We report all the estimates of the redshifts used for this plot in Table 1.[7]

We compared the nebulae here discovered with the work by Borisova et al. (2016), finding an overall agreement with our results. Borisova et al. (2016) also found mainly spatially symmetric nebulosities and only two of their targets (ID 1 and 3 in their work) show asymmetric extended nebulosities. Overall, this result is consistent with the expectations from previous works in the literature that showed that 50–70 per cent of the targeted quasars have extended Ly α emission in their surroundings on radii < 50 kpc (see Section 1). It is important to stress that previous works targeting $z \sim$ 3 quasars were achieving SB limits of the order of $\sim 10^{-17}$ erg s^{-1}

---

[6]We use bins with the same size as the intrinsic uncertainty on the estimate of the quasars redshift, i.e. 415 km s^{-1}.

[7]Our calculation of the quasar systemic redshifts gives consistent results with works in the literature (e.g. Weidinger et al. 2005; see Appendix C).
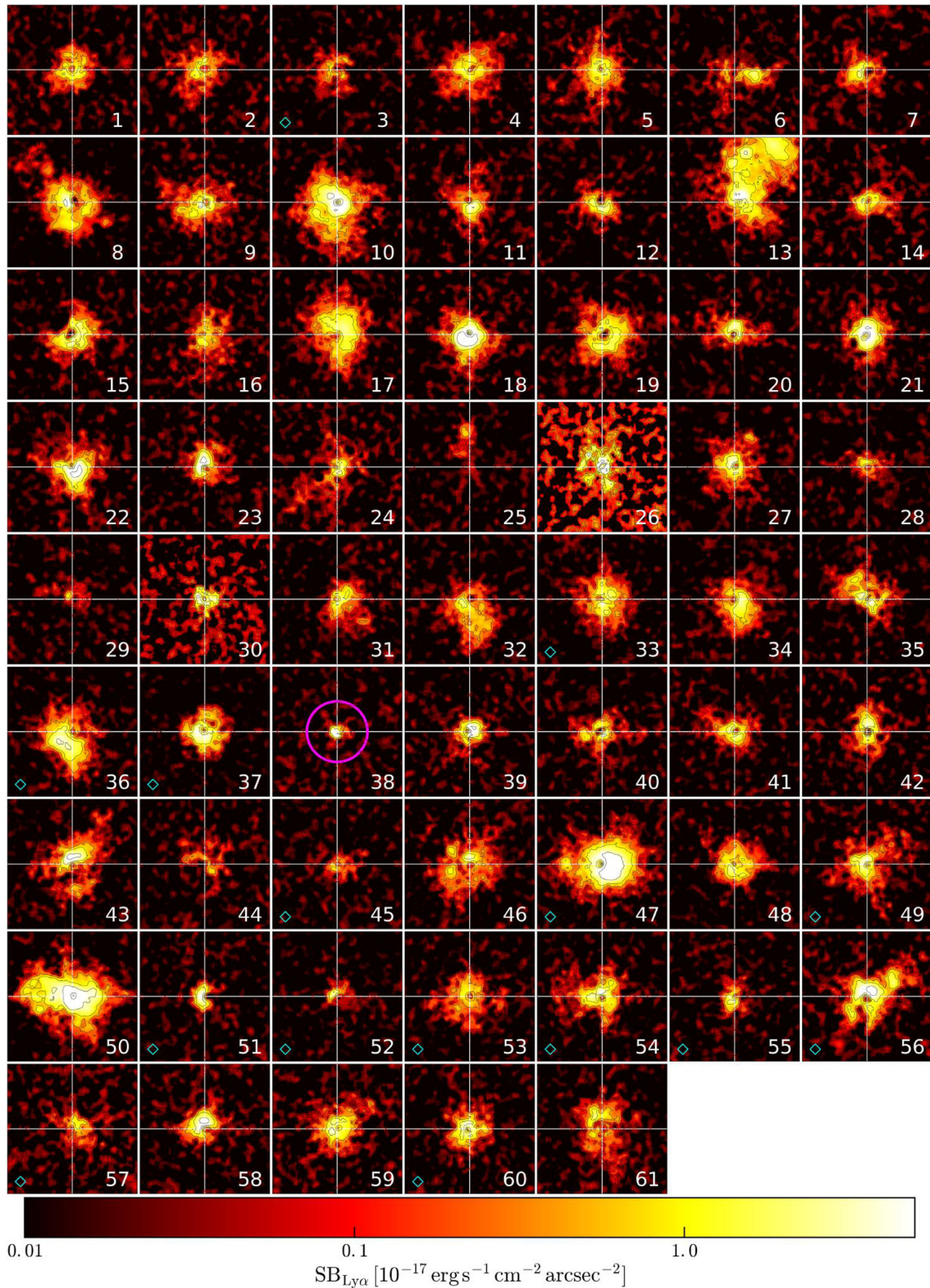
Figure 1. Atlas of the 61 'optimally extracted' NB images for the Ly α emission around the quasars in the QSO MUSEUM sample. Each image shows the SB maps of 30 arcsec $\times$ 30 arcsec (or about 230 kpc $\times$ 230 kpc) centred on each quasar after PSF and continuum subtraction (see Section 3.1 for details). Each of the system is numbered following Table 1. In each image the white crosshair indicates the position of the quasar prior to PSF subtraction. For reference, we overlay a magenta circle with a radius of 50 kpc on the image with ID 38. To highlight the significance of the detected emission, for each SB map we indicate the contours for S/N = 2, 4, 10, 20, and 50. A cyan diamond in the bottom left corner indicates when the quasar is radio-loud. The detected extended Ly α emission shows a diversity of extents, geometries, and substructures. North is up, east is to the left.
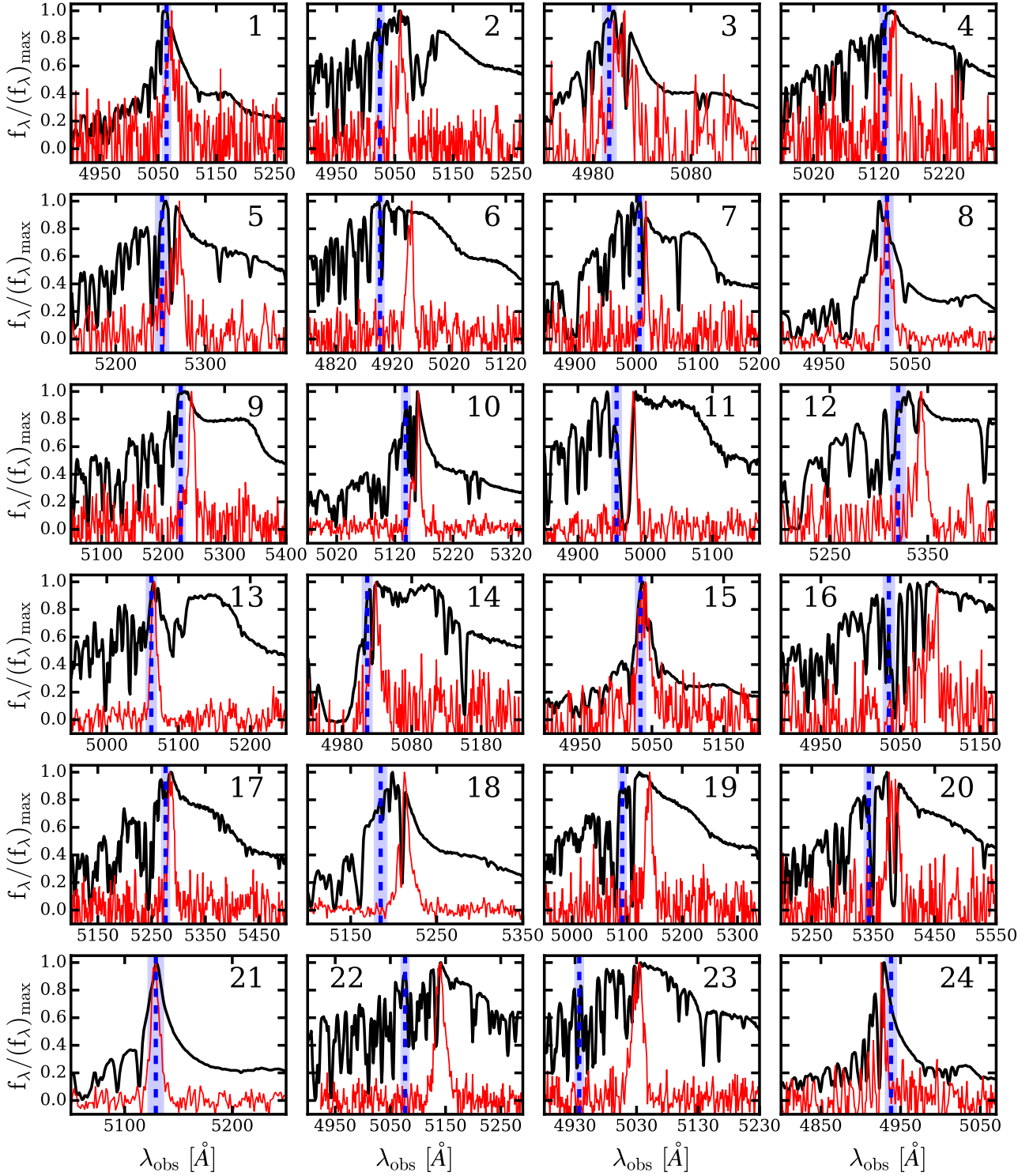
Figure 2. 1D spectra for the quasars in our sample (black) and discovered nebulosities (red) at the location of the Ly α emission, in the observed frame. Each spectrum has been extracted in a circular aperture of 1.5 arcsec radius, and it is normalized to its peak in this wavelength range. The dashed blue lines indicate the systemic redshift of the quasars as listed in Table 1, and the blue shaded regions indicate the calibration uncertainty on these estimates (415 km s^{-1}). Following Table 1, we report the quasars' ID numbers in each panel. The nebulosities show a much narrower line profile than quasars, and appear to be shifted from the current estimate for the quasars' systemic redshift.
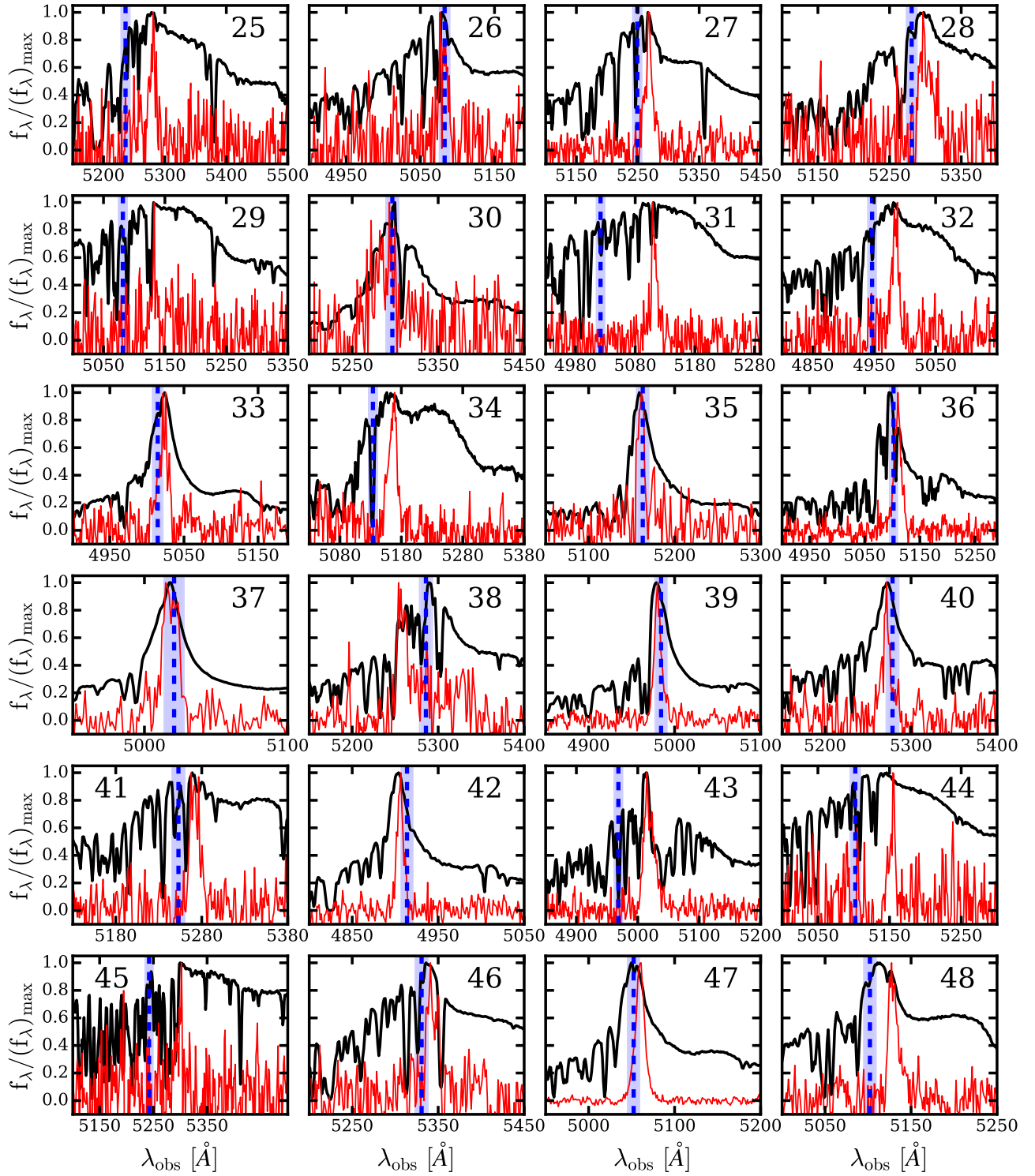
Figure 2. – *continued*
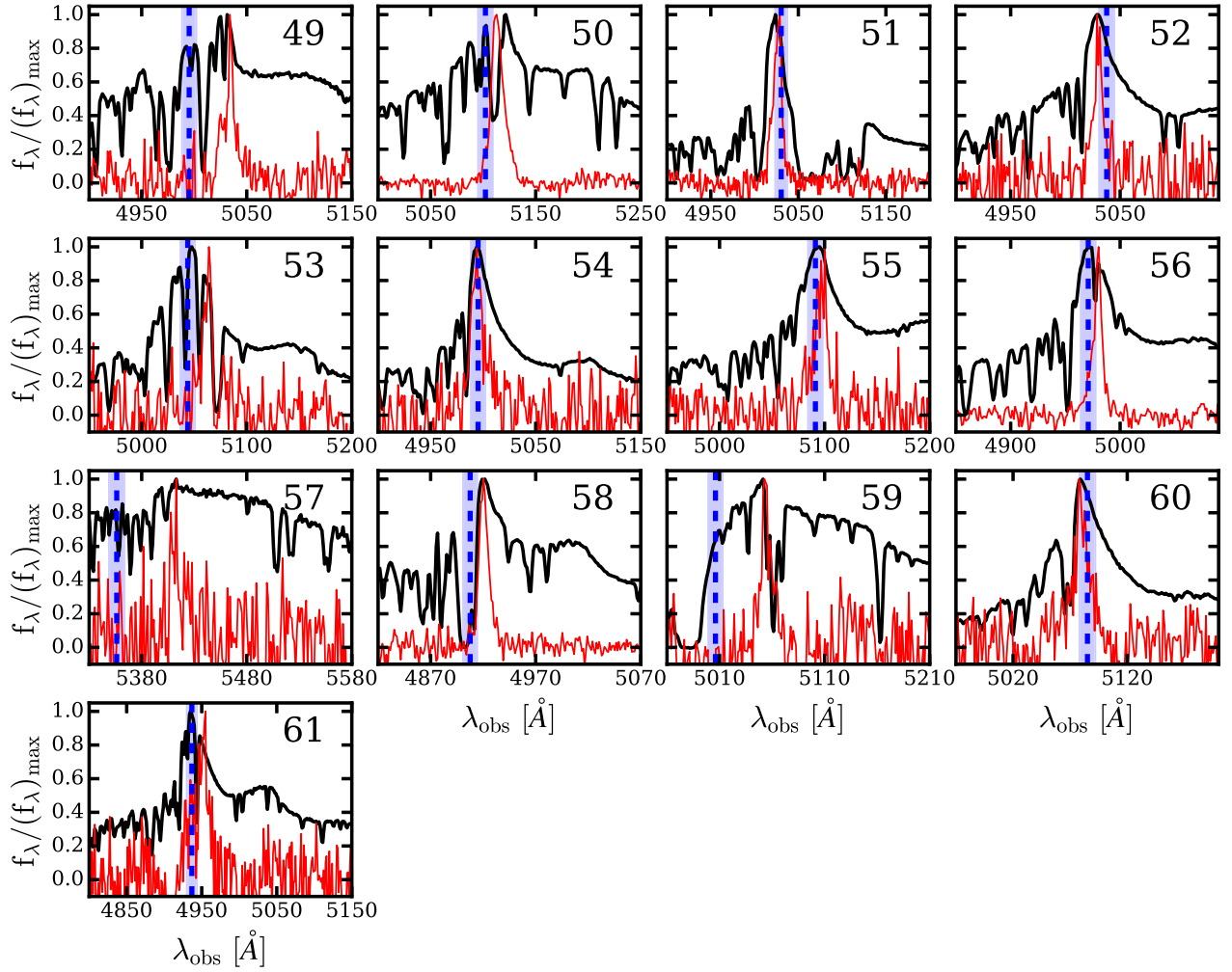
Figure 2. *– continued*

cm^{-2} arcsec^{-2} evaluated for equivalent 60 Å NB filters (e.g. Heckman et al. 1991a; Christensen et al. 2006), which is much poorer (at least one order of magnitude) than any recent MUSE data, including our work.

Regarding the velocity shift between the Lyα nebulosities and the quasars systemic, the values reported in Borisova et al. (2016) (their Table 2) show that all nebulosities have positive velocity shifts in the range 959 km s^{-1} $\leq \Delta v \leq$ 4011 km s^{-1}, and with a median value of $\Delta v_{\rm median} = 1821$ km s^{-1}.[8] However, while looking at their fig. 2 it appears that the peak of the Lyα emission from the nebulosities is closer to the peak of the Lyα emission of the quasars themselves, being sometimes also blueshifted from the quasar's systemic (e.g. their ID 14, 16). The closer association between the nebulosities and the peak of the Lyα emission of the quasars themselves seems thus in agreement with our analysis.

4.1.1 Quantifying the spatial asymmetry of the emission

A better understanding of the discovered Lyα nebulae requires quantitative information also on their morphology and on the level of asymmetry of the structures above our current detection limits. Indeed, this information should be used to infer the physical properties, geometry, and scales of the Lyα emitting gas both observationally and in comparison to current cosmological simulations post-processed with radiative transfer codes (e.g. Weidinger et al. 2005; Cantalupo et al. 2014). We have thus quantified the asymmetry of the Lyα light distribution in the discovered nebulosities by estimating (i) the distance between the quasar and the flux-weighted centroid of the emission within the 2σ isophote of each nebulosity, $d_{\rm QSO-Neb}$; (ii) the asymmetry of the emission within the 2σ isophote using the second-order moments of each nebulosity's light.

In particular, after estimating the flux-weighted centroid for each nebulosity ($x_{\rm Neb}$, $y_{\rm Neb}$) within the 2σ isophote in the 2D image shown in Fig. 1,[9] we have measured the flux-weighted second-order moments following for example Stoughton et al. (2002). These moments are defined as

$$M_{xx} \equiv \left\langle \frac{(x - x_{\rm Neb})^2}{r^2} \right\rangle_f , \quad M_{yy} \equiv \left\langle \frac{(y - y_{\rm Neb})^2}{r^2} \right\rangle_f ,$$

$$M_{xy} \equiv \left\langle \frac{(x - x_{\rm Neb})(y - y_{\rm Neb})}{r^2} \right\rangle_f , \tag{1}$$

---

[8]The quasars' systemic redshift in Borisova et al. (2016) is obtained as in this work. Thus, it is similarly uncertain.

[9]Also for this analysis the 1 arcsec × 1 arcsec region around each quasar, and used for the PSF rescaling, has been masked.
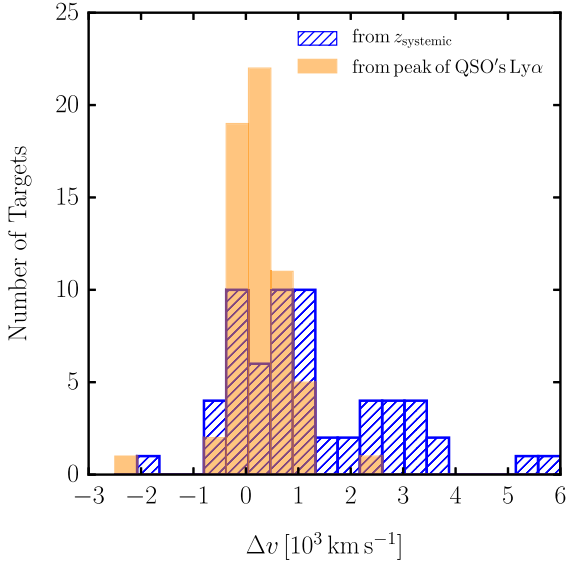
Figure 3. Histogram of the velocity shifts between the flux-weighted centroid of the Ly α emission peak of the nebulosities $z_{\text{peak Ly}\alpha}$ and the systemic redshift of the quasars z_{systemic} (blue), both listed in Table 1. We compare this histogram with the histogram of the velocity shifts between $z_{\text{peak Ly}\alpha}$ and the Ly α emission peak of the quasar itself $z_{\text{peak QSO Ly}\alpha}$ (orange, see Table 1). The Ly α nebulosities appear to be closer to $z_{\text{peak QSO Ly}\alpha}$ than to the current (uncertain) z_{systemic} of the quasars.

where r is the distance of a point (x, y) from the flux-weighted centroid. Using the second-order moments one can define the so-called 'Stokes parameters'

$$Q \equiv M_{xx} - M_{yy}, \quad U \equiv 2M_{xy}, \qquad (2)$$

and derive the asymmetry (or the ratio between the semiminor and semimajor axis b and a), and the position angle describing the light distribution:

$$\alpha = b/a = \frac{(1 - \sqrt{Q^2 + U^2})}{1 + \sqrt{Q^2 + U^2}}, \quad \phi = \arctan\left(\frac{U}{Q}\right). \qquad (3)$$

In particular, the angle ϕ is the angle between the semimajor axis and the closest x- or y-axis. In Table 3 we list the obtained parameters following this formalism: distance between each quasar and the centre of the nebulosity $d_{\text{QSO-Neb}}$, the asymmetry α, and the angle ϕ after converting it to the more common angle East of North.

In Fig. 4 we plot the distance $d_{\text{QSO-Neb}}$, and the asymmetry α versus the area enclosed by the 2σ isophote of each Ly α nebulosity in the top and bottom panels, respectively. To help the visualization of the data we also show the histogram for each quantity. This figure clearly shows that most of the nebulae have their flux-weighted centroid in close proximity of the targeted quasar, $(d_{\text{QSO-Neb}})_{\text{median}} = 8.3$ kpc (or 1.1 arcsec), and that appear to have a more circular shape, $\alpha_{\text{median}} = 0.71$. On the contrary, there are a handful of cases for which the centroid of the nebulosity is clearly separated from the quasar (>20 kpc), with ID 13 (or PKS 1017 + 109) being the extreme case ($d_{\text{QSO-Neb}} = 64.4$ kpc). Also, seven nebulosities show an asymmetry $\alpha < 0.5$. However, while most of these small asymmetries are driven by features on small scales, ID 13 (or PKS 1017 + 109) appear to be a clear outlier with the small asymmetry driven by structures on large scales, i.e. encompassing an area $\geq 3.4 \times$ that of the other six nebulosities with $\alpha < 0.5$. These characteristics are probably pieces of evidence of the powering mechanism for the Ly α emission (see Section 5.3), of the local environment of the system studied (e.g.
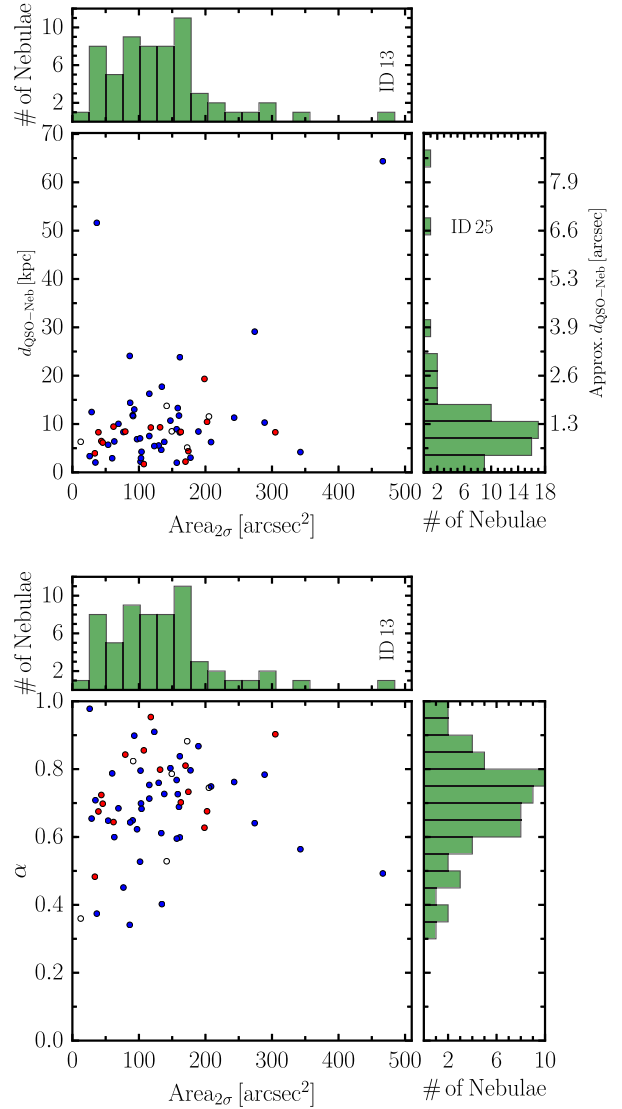
Figure 4. Top panel: plot of the distance between the quasar position and the flux-weighted centroid of the Ly α nebulosity, $d_{\text{QSO-Neb}}$, versus the area enclosed by the 2σ isophote. Most of the nebulosities are centred at small separations from the quasar, with ID 13 (or PKS 1017 + 109) being a clear outlier. Lower panel: plot of the asymmetry α, i.e. the ratio between the semiminor axis b and semimajor axis a, versus the area enclosed by the 2σ isophote. ID 13 (or PKS 1017 + 109) appears to be a clear outlier with the small asymmetry driven by structures on large scales. In both panels, blue circles indicate the radio-quiet systems, red circles the radio-loud, and the open circles the six cases where no radio data are available.

Hennawi et al. 2015; Arrigoni Battaia et al. 2018), and possibly encode information on the different orientations of the systems with respect to our observational vantage point. In Fig. 4 we also indicate weather a quasar is radio-quiet (blue) or radio-loud (red), showing that the two populations do not differ on these plots.

4.1.2 Individual circularly averaged surface brightness profiles

In this section we compute the radial SB profiles for the discovered Ly α nebulosities as commonly done in the literature. Such profiles provide additional information on the diverse morphologies of the nebulosities, while can shed light on the mechanism powering the

Ly α line and on the cool gas distribution around quasars at this redshift. In particular, we aim to obtain an average profile for our sample, and compare it to the average profile of Ly α seen from the quasar CGM at different redshifts (e.g. Arrigoni Battaia et al. 2016).

First, to use the full information contained in the MUSE datacubes we decided not to use the 'optimally extracted' images. Indeed these images are obtained by cutting the data with an S/N threshold that would inevitably result in the loss of information at large distances from the quasar. From Table 3 – where we report the maximum projected distance reached by each Ly α structure from the quasar position – it is evident that 32 nebulosities do not have emission above 2σ extending at distances >80 kpc from the quasar. In addition, the noise characterization in the 'optimally extracted' images is not trivial and would introduce an additional uncertainty in the estimate of the profiles (as explained in Borisova et al. 2016).

For these reasons we extracted the circularly averaged SB profiles from NB images with fixed width (30 Å) obtained from the PSF and continuum subtracted datacubes, and centred at the Ly α peak of each nebulosity. For each of these NB images, we have propagated the corresponding subsection of the variance cube to obtain a variance image. As anticipated in Section 2, in Table 2 we list the 2σ SB limit for each of these NB images, which are roughly $5\times$ higher than for a single layer (1.25 Å). While such a fixed width does not enclose the whole Ly α emission above the S/N = 2 threshold used to extract the 3D mask, it is a good compromise to include most of the bright Ly α emission while being still sensitive to emission at very low SB levels on large scales ($\sim$100 kpc). Also, this width is similar to the wavelength range spanned by the NB filter used in the literature to detect Ly α emission, and thus enables a more direct comparison with those studies. Fig. 5 shows all the NB images obtained from the PSF and continuum subtracted datacubes together with the white-light images and the 'optimally extracted' images. This figure clearly displays the higher noise level in comparison to the single layer (1.25 Å) used as background in the 'optimally extracted' NB images (see Section 3.1).

Before proceeding with the extraction of the profiles, we further prepared the NB images by masking artefacts and compact sources, which would otherwise contaminate the profiles. In particular, even though we have subtracted the continuum using the CubeBKGSub algorithm within CUBEXTRACTOR, our images are affected by residuals (both positive or negative) especially at the position of bright continuum sources, i.e. stars or galaxies. To avoid such contamination, we constructed a mask for the continuum sources using the white-light image of each field. This approach is very conservative as the subtraction of the continuum has been tested in previous works (e.g. Borisova et al. 2016). In particular, in analogy to what was done in Arrigoni Battaia et al. (2016), we run CUBEXTRACTOR to identify all the continuum sources above S/N = 2 and down to very small objects (five pixels minimum) within the white-light images. CUBEXTRACTOR produces a 'segmentation' image that is then used to create a mask, after removing the region corresponding to the quasar that otherwise would hide the emission of interest here.

In addition, to avoid the detection of signal from compact line emitters around the quasars, i.e. objects that do not have a continuum detection, we obtain a similar mask using the NB image itself. However, at this step we only identify compact sources, with area between 5 and 20 pixels (roughly a seeing disc). By combining the two individual masks, we then obtained a final mask that allow us to neglect in our analysis both pixels from artefacts and compact sources. Overall this masking procedure reduces the fraction of the FOV that is usable around each quasar to an average of 88 per cent.

This analysis and the final available FOV is similar to what has been used to extract radial SB profiles around quasars in NB images of similar depth (Arrigoni Battaia et al. 2016).

We then calculated the circularly averaged SB profile for each quasar in radial logarithmic bins centred at the quasar positions with an unweighted average of all the not-masked pixels within each annulus. We then consistently propagated the errors from the variance images. To facilitate the visualization of the profiles and the comparison with the NB images, we overplot on the 'optimally extracted' images in Fig. 5 the annuli within which we calculate the radial SB profiles. In the same figure we show the SB profiles for each of the discovered Ly α nebulosities (blue data points with errors), together with the 2σ error estimates expected within each aperture in the case one assumes a perfect sky and continuum subtraction (grey shaded area).[10] In addition, to compare such profiles with the 'optimally extracted' NB images, we compute the profiles within the same annuli, but only using the emission enclosed by the 2σ isophote (red data points). By construction, these profiles do not extend further than the contour enclosing the maximum distance defined by the 2σ isophote.[11] While extracting both radial profiles, we masked the central 1 arcsec $\times$ 1 arcsec region around the quasar position used for the PSF rescaling. For this reason the radial profiles in Fig. 5 are shown for radii $R > 10$ kpc.

Overall, this analysis once again shows the diversity of the morphologies and extents of the Ly α emission around the targeted quasars, while emphasizing the differences in SB between the different objects. In particular, consistently with the 2D images, the profiles extend out to the maximum annulus that includes the 2σ isophote, and beyond this radius they appear to monotonically decrease. This decrease is not driven by the current depth of the data as otherwise we would have had larger nebulae in the 'optimally extracted' images than in the NB images. This can be clearly seen by comparing the data points from the NB images (blue) and the data points from the 'optimally extracted' images (red). The decrease is visible in both symmetric and asymmetric nebulosities. Further, we do not see any particular difference between the individual profiles of the radio-quiet and radio-loud objects.

4.1.3 The average surface brightness profiles

In this section we present average SB profiles for our sample. We have obtained three different stacked profiles by averaging with equal weights the profiles obtained from the NB images of (i) all the 61 quasars, (ii) the radio-quiet sample (39 quasars), and (iii) the radio-loud sample (15 quasars).[12]

The left-hand panel of Fig. 6 shows these three SB profiles versus the physical radius of the annuli used for the profile extraction. In particular, we indicate the whole sample in blue (large data points), while the subsamples of the radio-quiet and radio-loud objects in pink and green (small data points), respectively. We note that there

---

[10]This is obtained using the formula $SB_{limit}(area) = SB_{limit}^{1\,arcsec^2}/\sqrt{area}$ where $SB_{limit}^{1\,arcsec^2}$ is the SB limit in 1 arcsec^2 reported in Table 2. This formula is true only if a perfect sky and continuum subtraction is performed. For this reason the shaded region has to be regarded as only indicative.

[11]The last data point in some of the profiles extracted using the 3D mask (red crosses) is driven to high SB values because of the small portion of nebula within the last ring.

[12]We remind the reader that currently we do not have information on the radio emission for six quasars in our sample, which are thus excluded from both the radio-quiet and radio-loud sample.
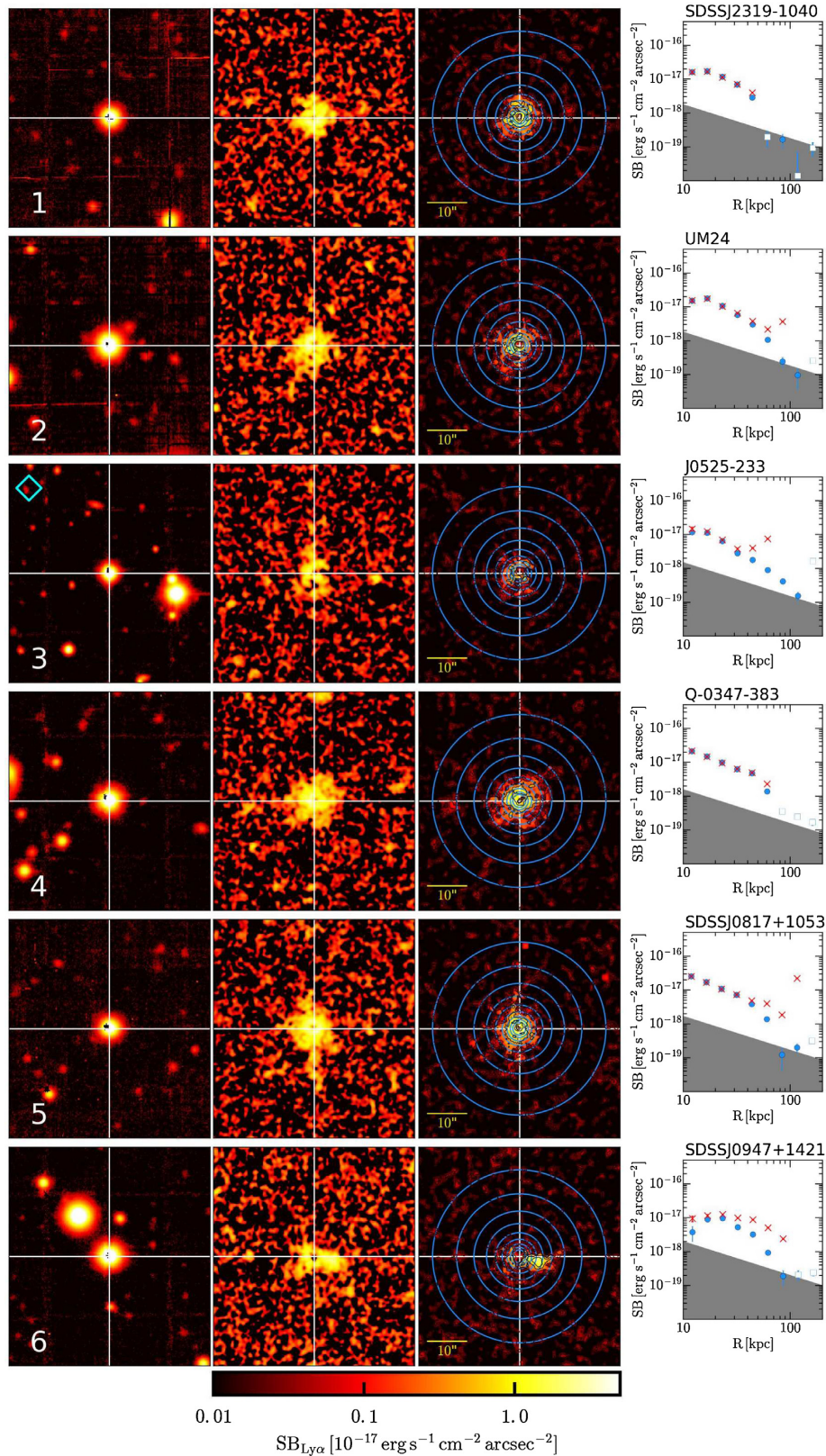
Figure 5. Each row shows 50 arcsec × 50 arcsec (or approx. 380 kpc × 380 kpc) images (white-light image, 30 Å NB image, 'optimally extracted' NB image) and the circularly average SB profiles for the targets in our QSO MUSEUM survey. A cyan diamond in the top left corner of the white-light image indicates that the quasar is radio-loud. For comparison, the NB images and 'optimally extracted' NB images are shown on the same colour scheme and the position of the quasar prior to PSF subtraction is indicated by the white crosshair in all images. We overlay on the 'optimally extracted' images the circular apertures used for the extraction of the profiles. In the right-most panel we show the circularly average SB profile extracted from the NB image (blue) and from the 'optimally extracted' NB image (red) (see Section 4.1.2 for details). The grey shaded region represents the 2σ SB limit expected within each aperture in the case it is assumed a perfect sky and continuum subtraction. North is up, east is to the left.
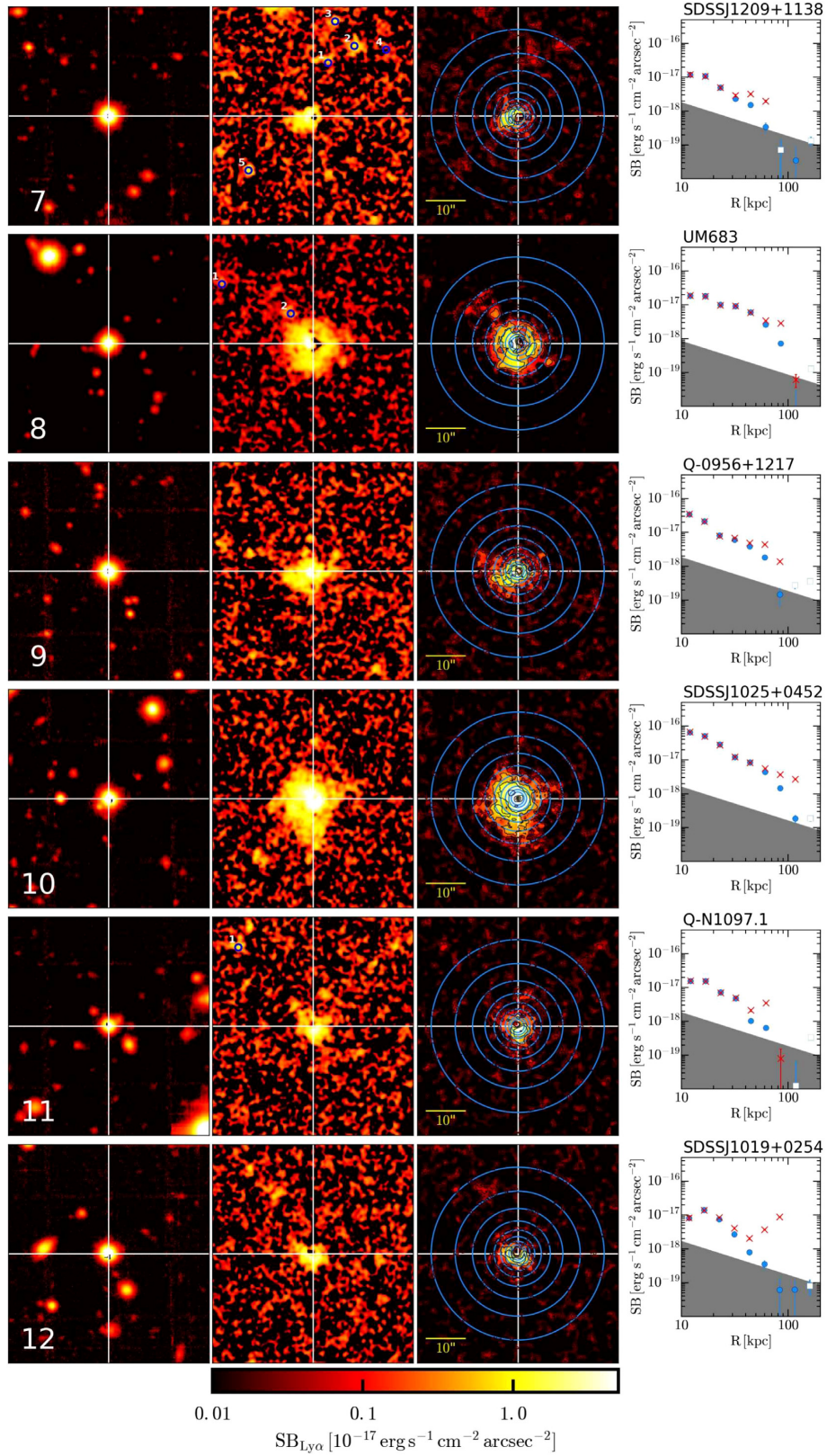
Figure 5 – *continued*
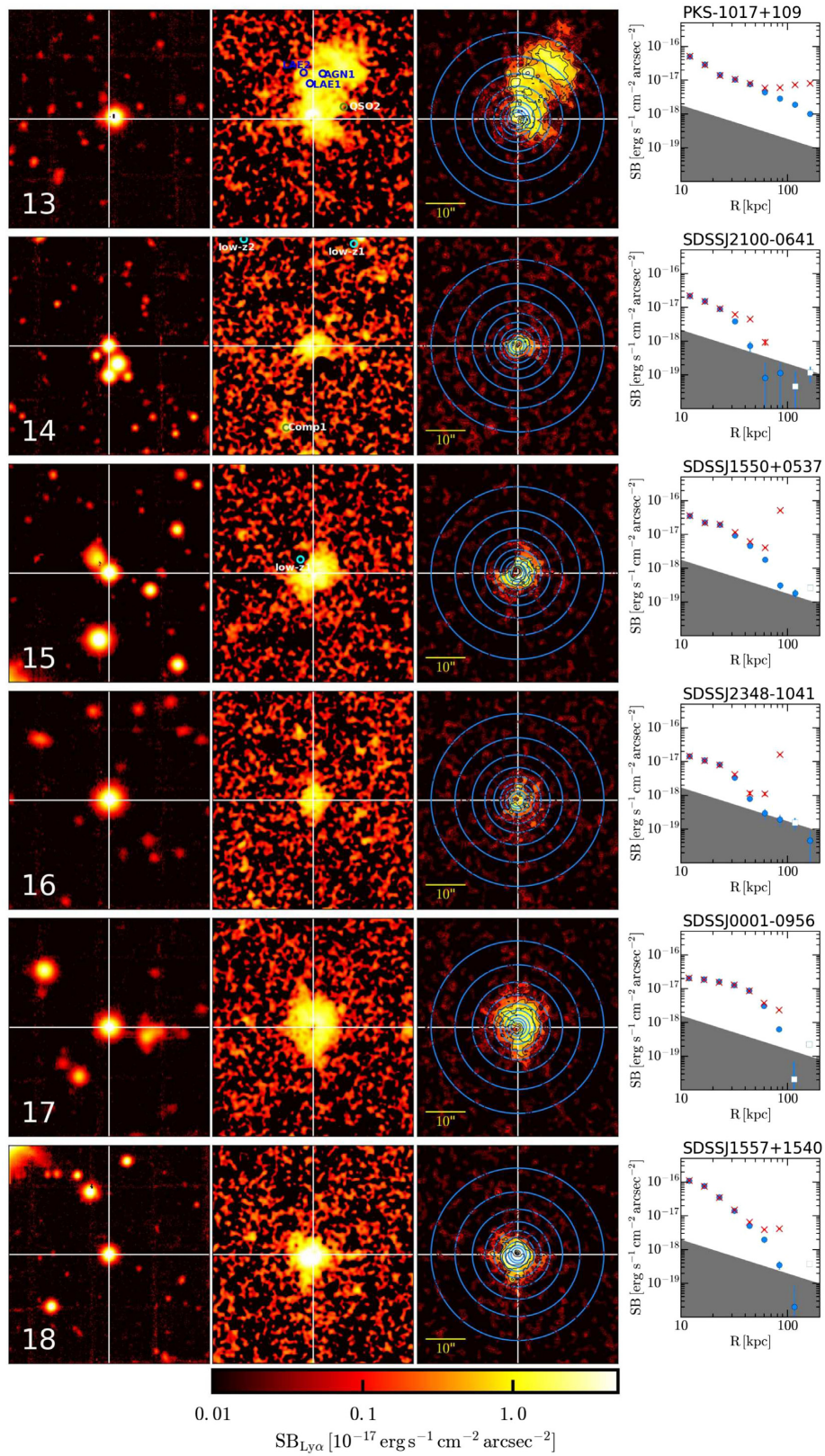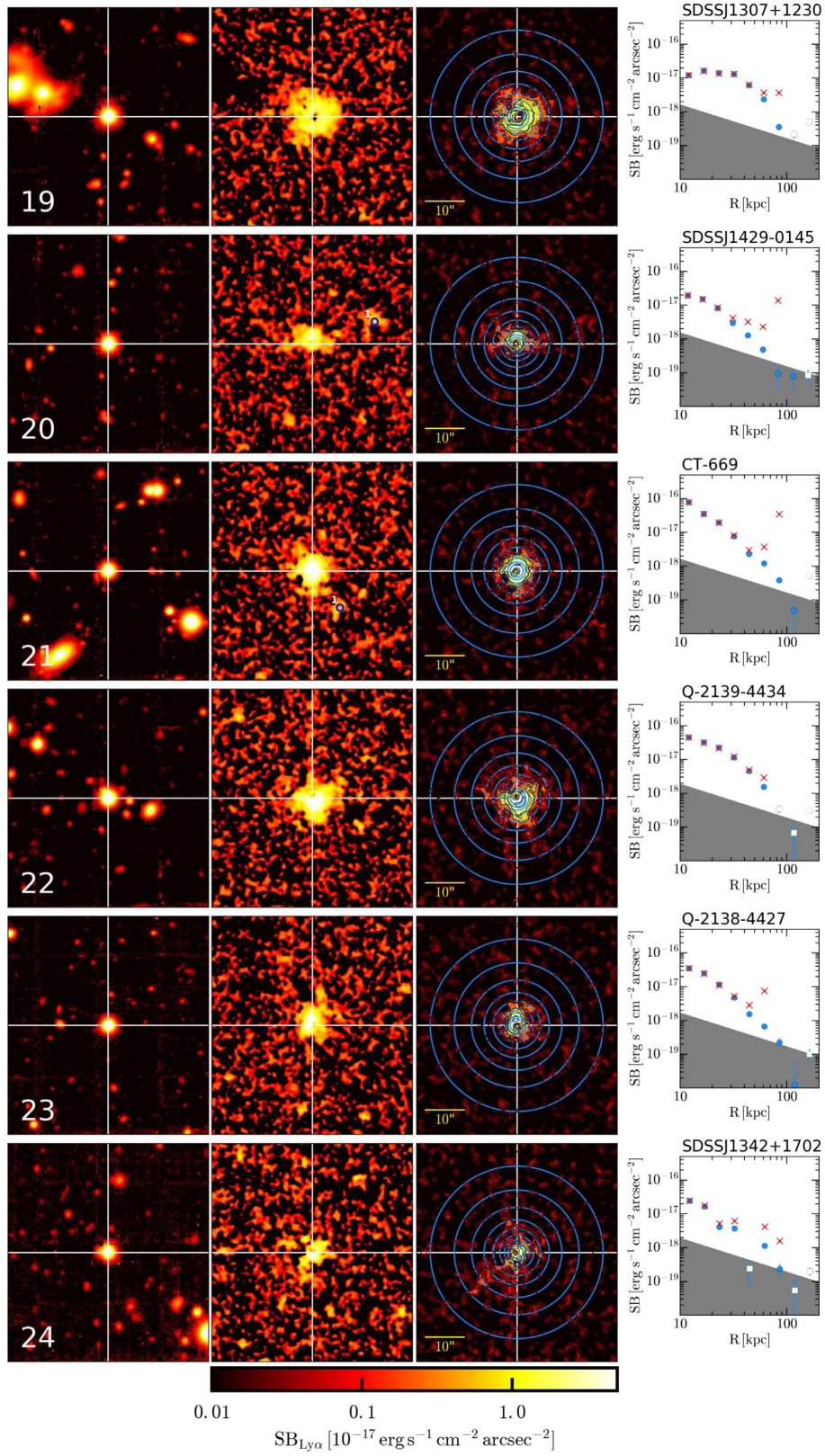
Figure 5 *– continued*
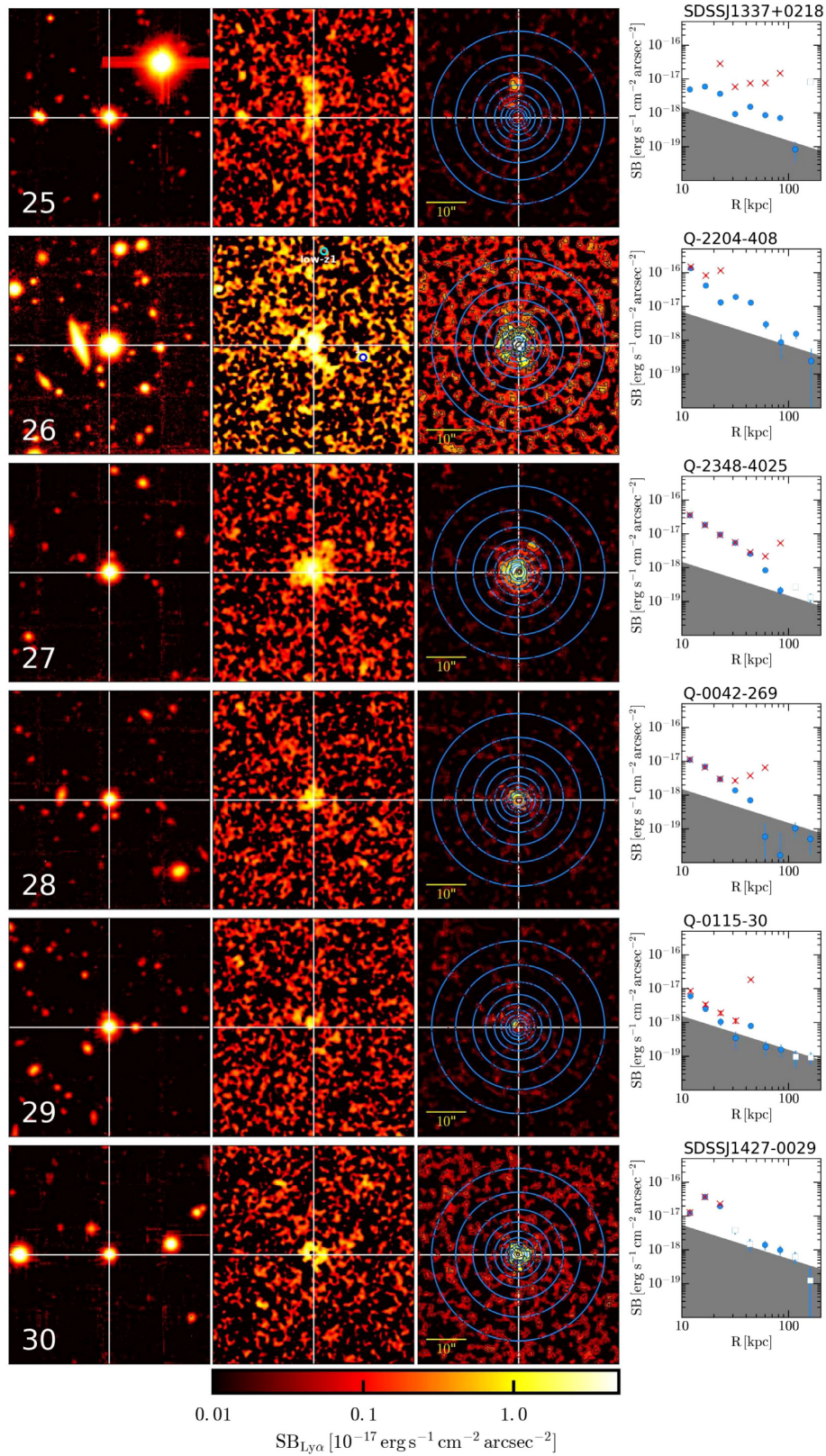
Figure 5 – *continued*
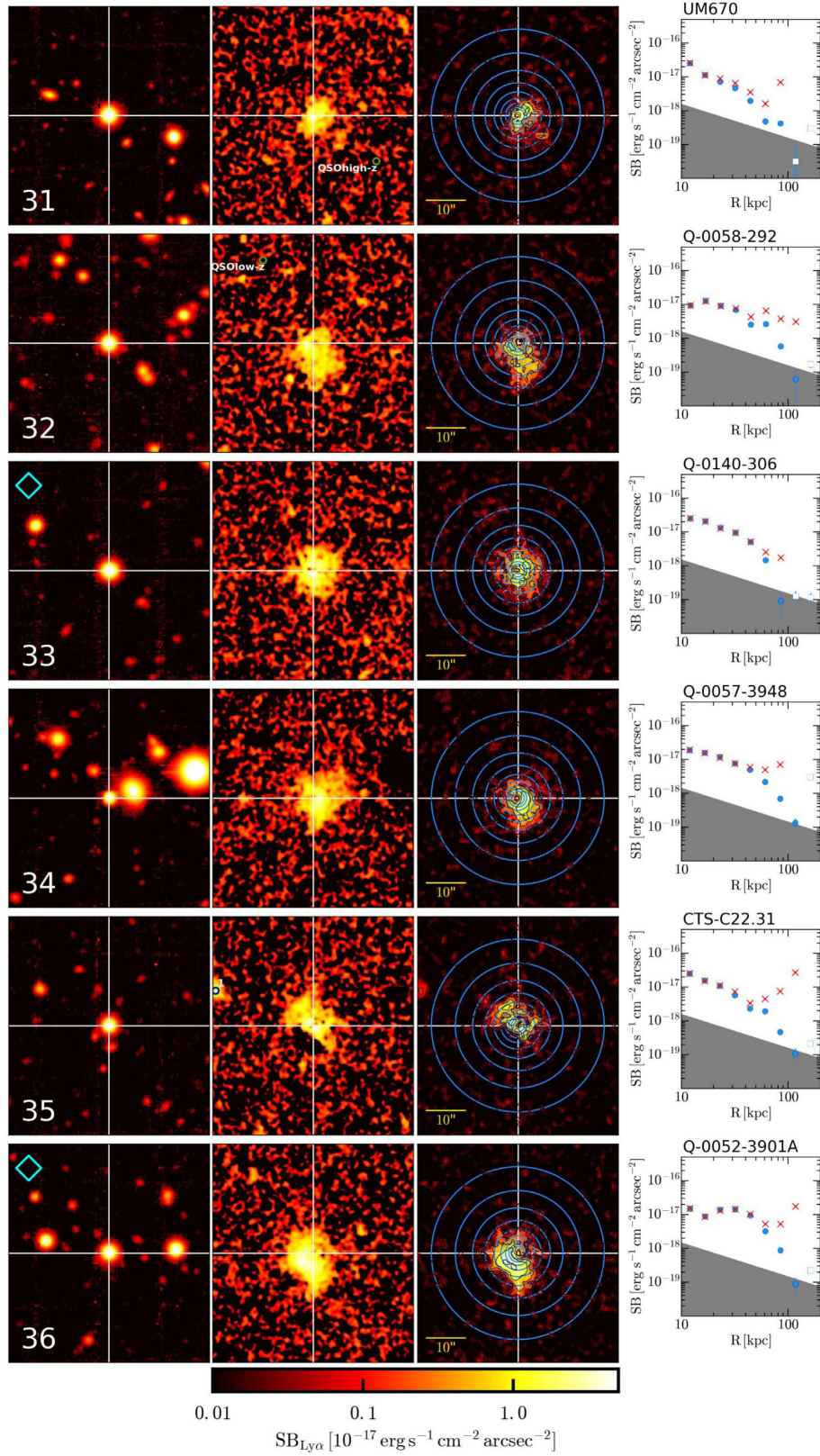
Figure 5 *– continued*

Figure 5 – *pccontinued*
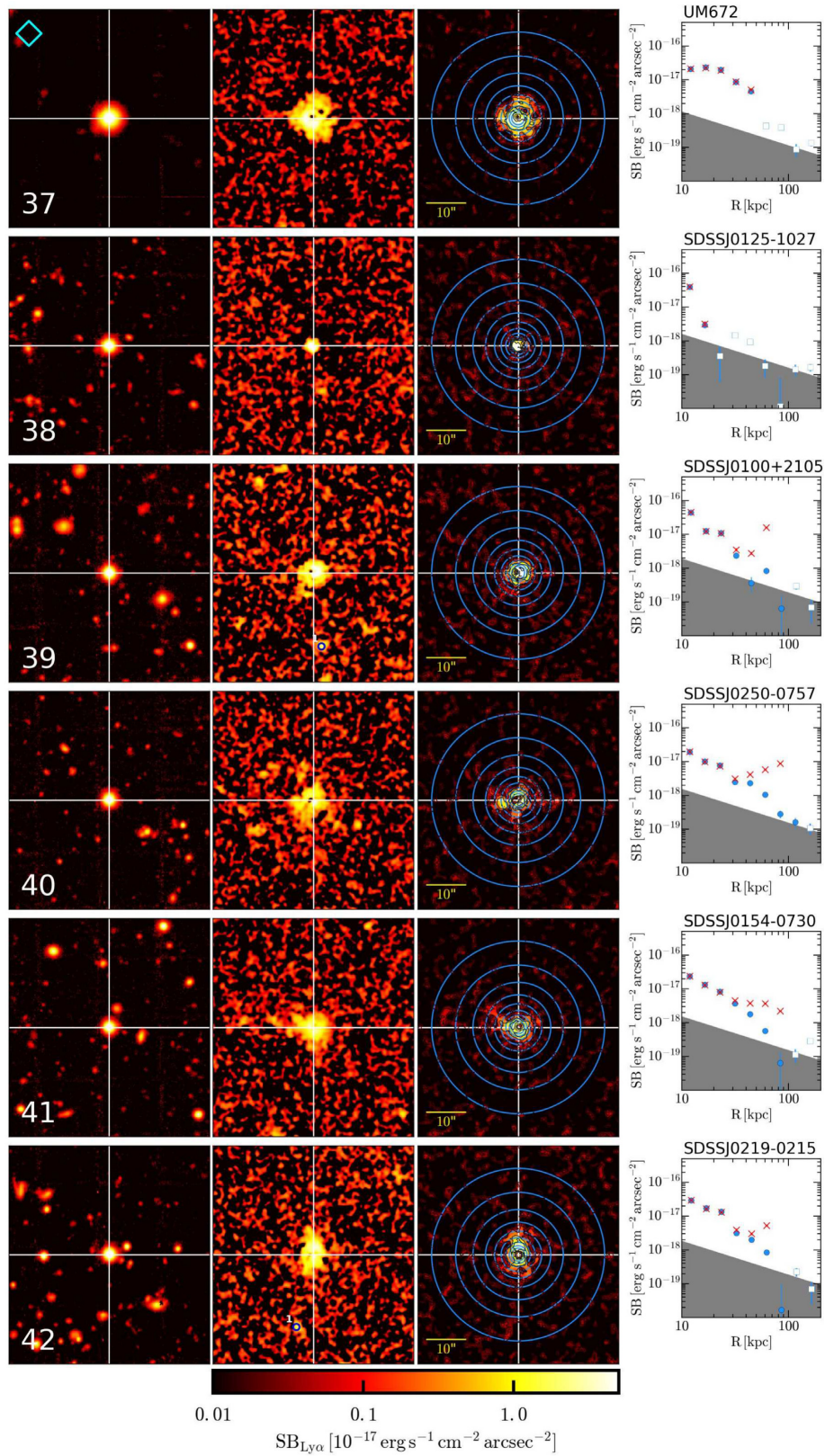
Figure 5 – *continued*

Figure 5 *–continued*

Figure 5 *–continued*

$SB_{Ly\alpha} [10^{-17} \, erg \, s^{-1} \, cm^{-2} \, arcsec^{-2}]$
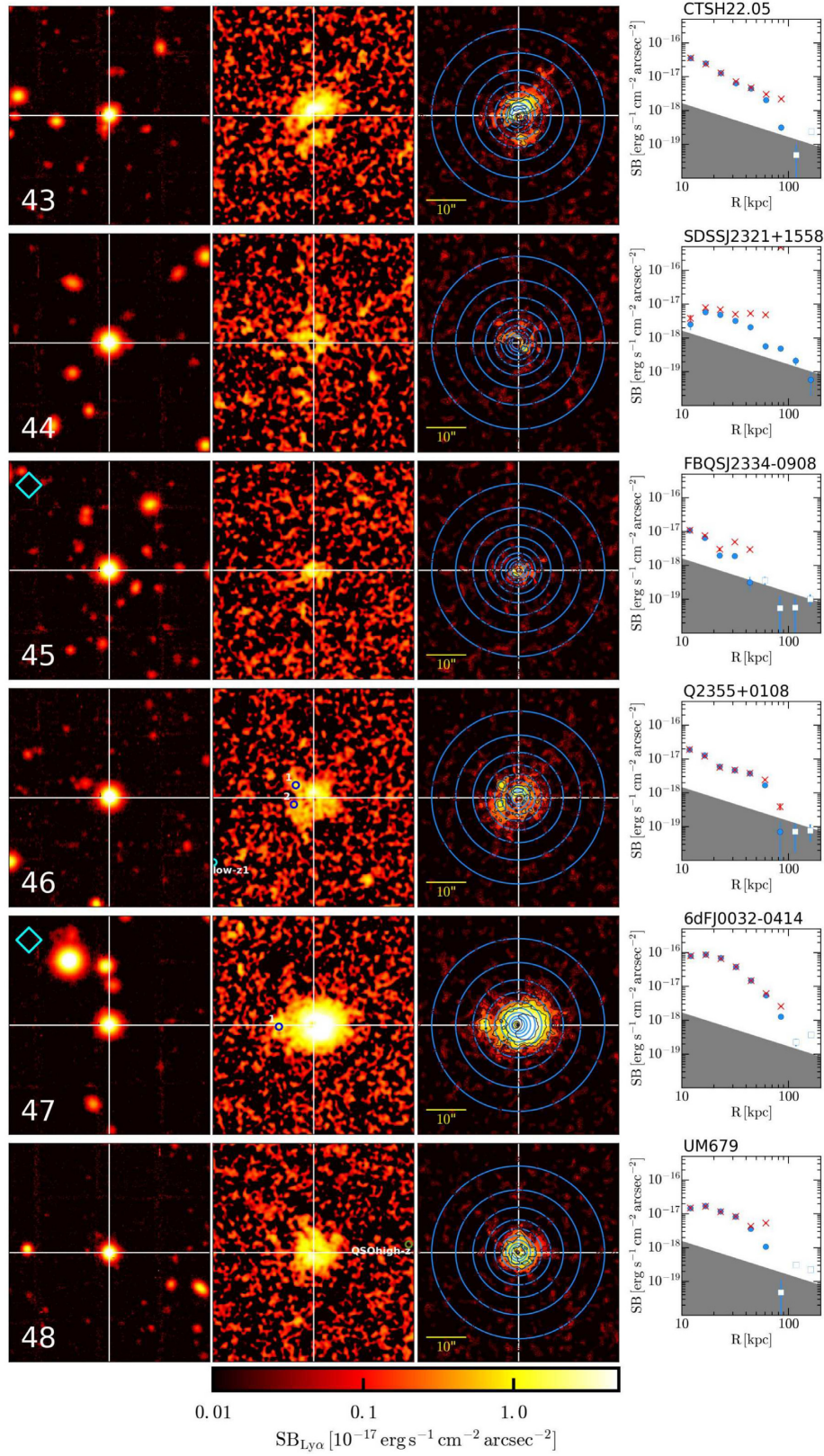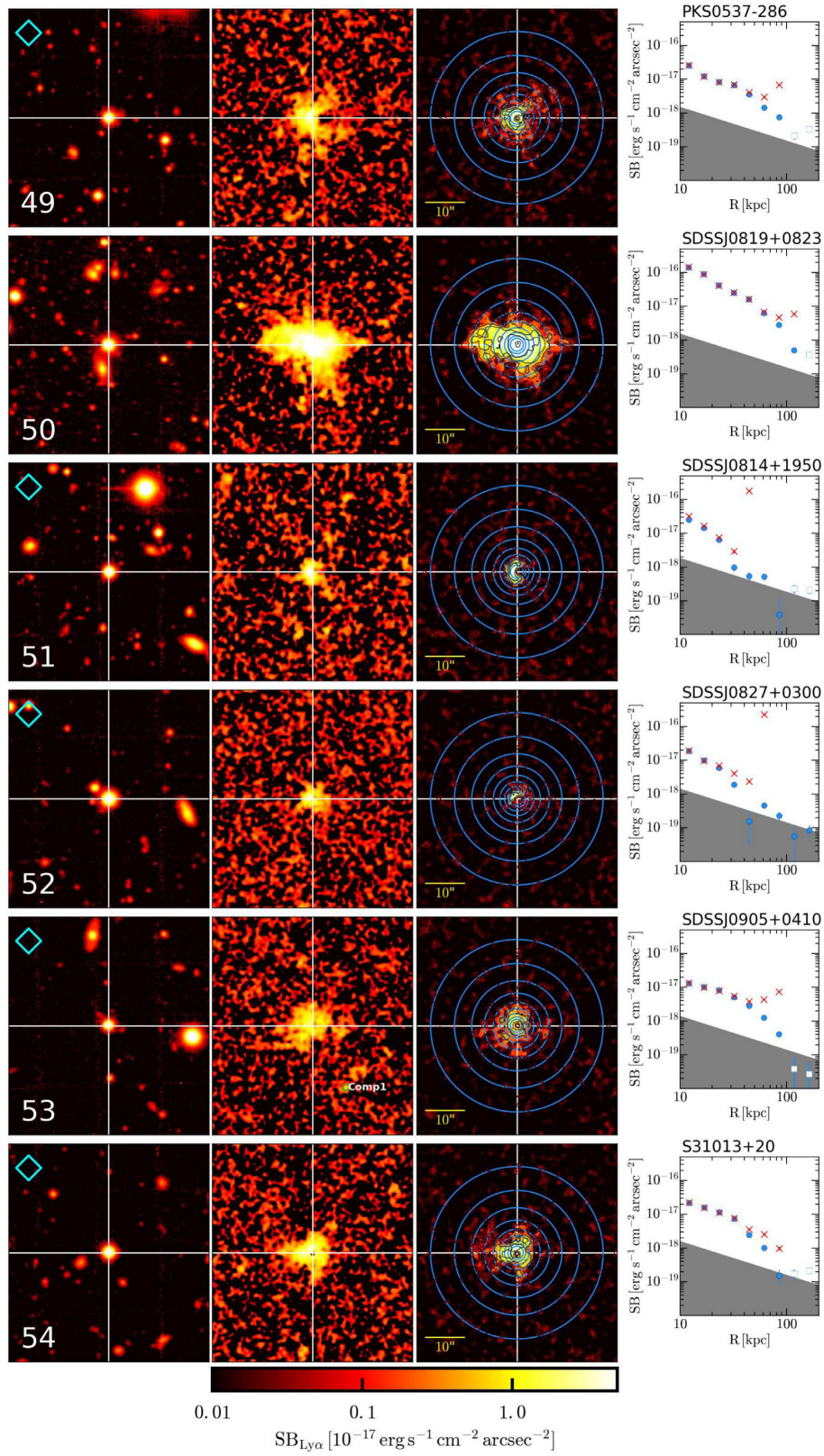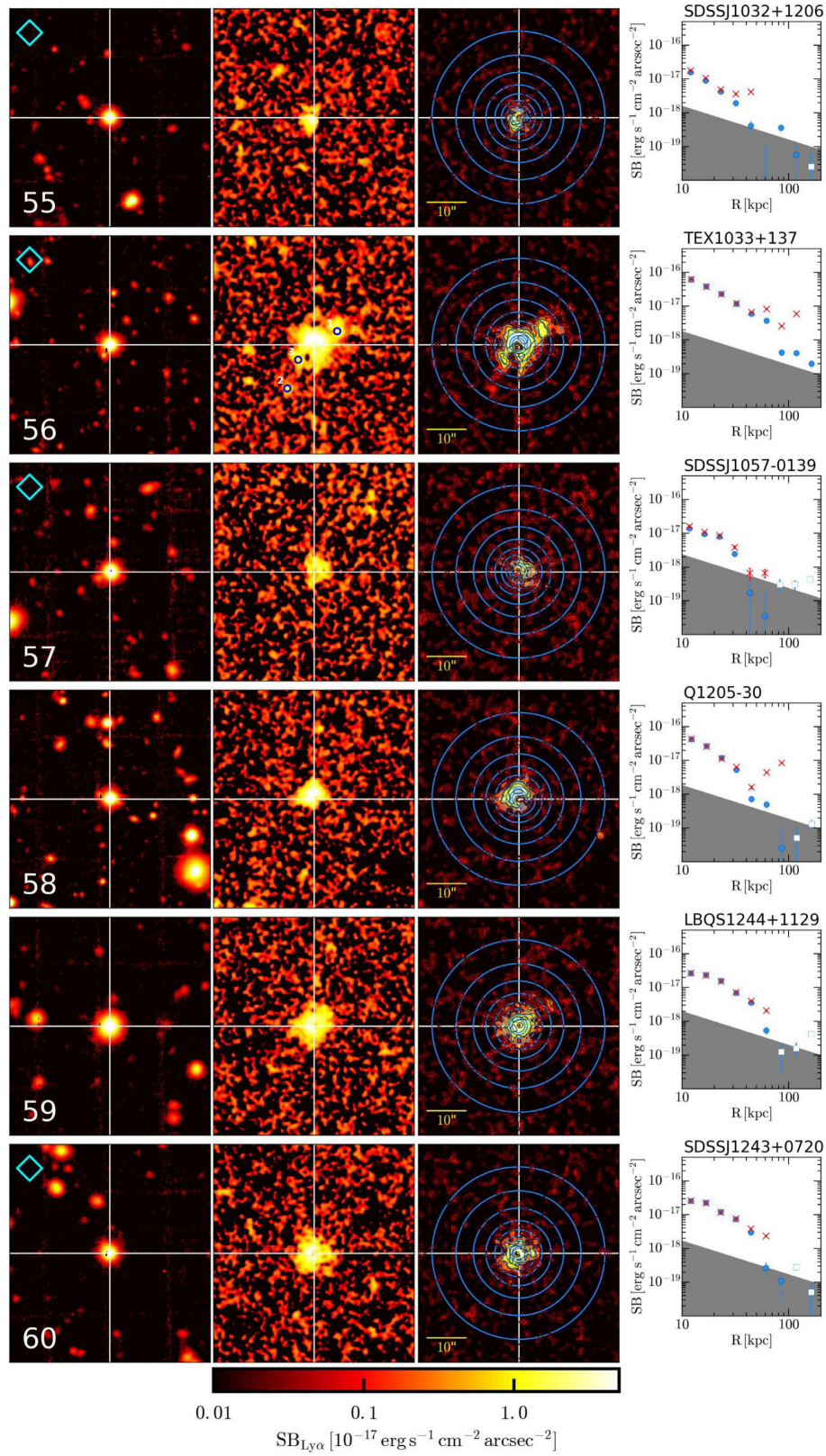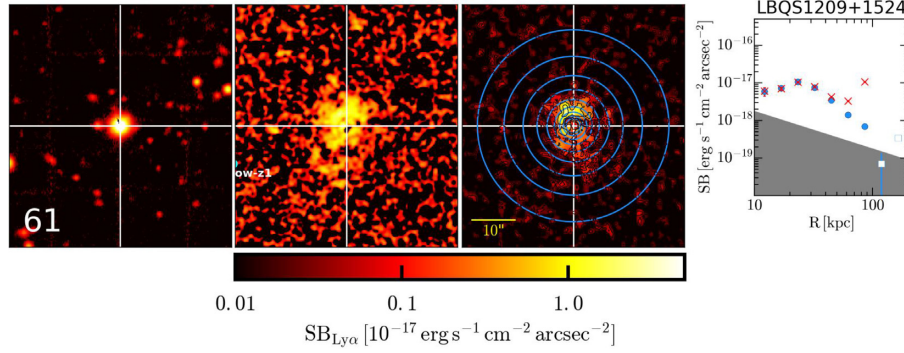
Figure 5 *–continued*

Figure 5 *–continued*
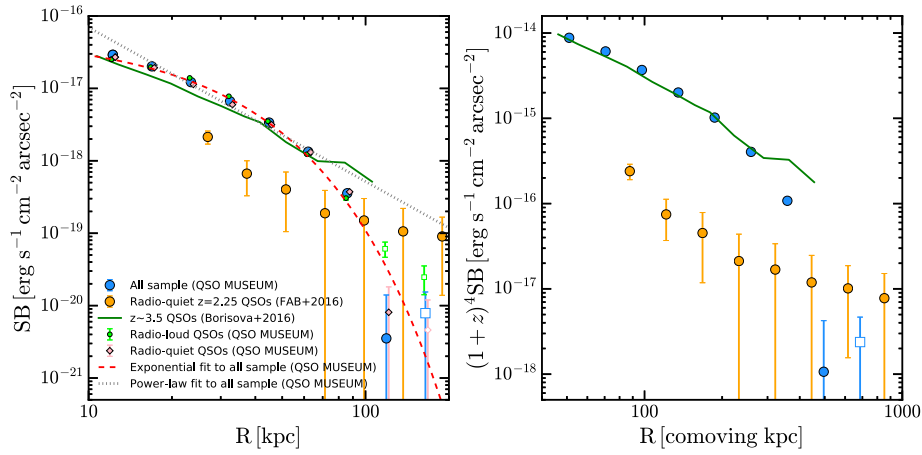
Figure 6. Average Ly α SB profiles for the nebulosities discovered in our QSO MUSEUM survey. Left-hand panel: we show the average profile for the whole sample (large blue; 61 targets), the radio-quiet subsample (pink diamond; 39 quasars), and radio-loud subsample (small green; 15 quasars) in observed SB units versus the physical radius. For the radio-quiet and radio-loud subsamples we slightly shifted the data points along the *x*-axis to allow a better visualization. For each profile, open squares indicate negative data points. For the whole sample we show the best exponential fit (dashed red line) and the best power-law fit (dotted grey line). In addition, we compare our data set with the average profile for (i) $z \sim 2.25$ quasars by Arrigoni Battaia et al. (2016), and for (ii) $z \sim 3.5$ quasars by Borisova et al. (2016). Right-hand panel: the average profile for the QSO MUSEUM sample is compared to the average profiles by Arrigoni Battaia et al. (2016), and Borisova et al. (2016) after correcting for the cosmological dimming and using comoving units for the radii. By comparing these data sets it appears that $z \sim 3$ quasars are surrounded by a brighter glow in the Ly α line (see Sections 4.1.3 and 5.2 for details and discussion).

is only a marginal difference between the radio-quiet and radio-loud subsamples at radii 20 kpc $< R <$ 50 kpc, with the radio-loud objects showing a slightly higher SB. For comparison with Borisova et al. (2016), we fit these stacked profiles with an exponential SB$(r) = C_e \exp^{-r/r_h}$ or a power law SB$(r) = C_p r^\alpha$. We found that the obtained stacked profiles are better fit by an exponential profile with scale length $r_h = 15.7 \pm 0.5$ kpc, $r_h = 15.5 \pm 0.5$ kpc, and $r_h = 16.2 \pm 0.3$ kpc, for the whole sample, the radio-quiet, and the radio-loud objects, respectively. The aforementioned excess in SB at intermediate scales for the radio-loud sample thus determine the small tentative difference in scale length between the two subsamples. Further, our quasars are surrounded by Ly α nebulosities characterized by scale lengths roughly 3 × larger than those for LAEs at similar redshifts (e.g. Leclercq et al. 2017), probably reflecting the different halo masses, and also the ability of the QSOs to power observable Ly α emission further out.

We note that our best-fitting power laws have slopes of $\alpha = -1.96$, $\alpha = -1.93$, and $\alpha = -1.81$, for the whole sample, the radio-quiet and the radio-loud objects, respectively. These values are consistent

with the power-law slope reported by Borisova et al. (2016) for their average profile, i.e. $\alpha = -1.8$. However in our case the best-fitting profile appears to be the exponential. For comparison purposes, the average profile from Borisova et al. (2016) is shown in Fig. 6 (solid green line), together with our best exponential fit (dashed red), and best power-law fit (dotted grey) to our whole sample.

For completeness, we have then computed the average SB profile of the whole sample and of the radio-quiet subsample both excluding the quasar with ID 13 (or PKS 1017 + 109), which shows a rare ELAN with multiple AGN companions (see Section 5.1; Arrigoni Battaia et al. 2018). The scale lengths for the profiles slightly shrinks $r_h = 15.4 \pm 0.7$ kpc and $r_h = 15.2 \pm 0.7$ kpc, respectively, for the whole sample and for the radio-quiet sample. However the uncertainties are larger than the variations. The brightness and extent of an ELAN thus seems to affect the average SB profiles even with a large sample of objects. Table 4 lists all the details of the profile fitting.

We then compare our stacked SB profile with the work by Arrigoni Battaia et al. (2016). This work produced a stacked Ly α

Table 4. Fit of the average Ly α surface brightness profile.

Sample	#	$\langle z_{\mathrm{Ly}\,\alpha}\rangle$	C_e^a (10^{-18})	r_h^a (kpc)	$\chi_e^{2\ b}$	C_p^c (10^{-18})	α^c (kpc)	$\chi_p^{2\ d}$
All	61	3.209	56.8	15.7	5.1	5124.3	−1.96	40.1
All but ID13^e	60	3.210	56.6	15.4	4.8	4103.7	−1.90	35.1
RQ^f	39	3.221	54.4	15.5	8.2	4250.6	−1.93	38.7
RQ but ID13^e	38	3.223	55.0	15.2	7.5	3596.5	−1.88	33.5
RL^f	15	3.174	56.2	16.2	0.6	3240.4	−1.81	45.2

Notes. ^{a}Best-fitting parameters assuming SB profile SB$(r) = C_e \exp(-r/r_h)$. C_e is in unit of 10^{-18} erg s^{-2} cm^{-2} arcsec^{-2}.

^{b}Reduced chi square for the exponential fit.

^{c}Best-fitting parameters assuming SB profile SB$(r) = C_p r^\alpha$. C_p is in unit of 10^{-18} erg s^{-2} cm^{-2} arcsec^{-2}.

^{d}Reduced chi square for the power-law fit.

^{e}ID13 (PKS-1017 + 109) is not included as it is surrounded by an ELAN.

^{f}RQ and RL stand for radio-quiet and radio-loud. Note that six targets currently do not have information in radio.

SB profile for the $z \sim 2$ quasar's CGM by targeting 15 $z \sim 2.253$ radio-quiet quasars with the NB technique, and achieving similar depths to our extracted NB data. Indeed, those NB data are a factor of ~ 2 less deep than our MUSE NB images, but the cosmological SB dimming of the form $(1 + z)^{-4}$ should compensate this difference. Those quasars are characterized by an average $M_i(z = 2) = -27.21$, and are thus slightly fainter than the quasar in this study [average $M_i(z = 2) = -28.05$; see Table 1]. However 8 out of 15 of those quasars have luminosities similar to quasars in the current sample. In particular two have magnitudes $M_i(z = 2) = -28.75$ (SDSS J093849.67 + 090509.7), and $M_i(z = 2) = -28.06$ (SDSS J084117.87 + 093245.3), which are comparable also to quasars in the sample of Borisova et al. (2016). Notwithstanding such differences in luminosity, Arrigoni Battaia et al. (2016) did not report any dependence of the individual profiles of the extended Ly α emission with respect to the luminosity of the quasar themselves.

As discussed in Arrigoni Battaia et al. (2016), the NB imaging technique could be affected by flux losses if the Ly α line is in reality at a different wavelength (thus redshift) than expected, and thus falls outside or at the edge of the used filter. Arrigoni Battaia et al. (2016) have shown that only error distributions on the redshift with width comparable to the width of the NB filter (in this case about 2500 km s^{-1}) can result in significant flux losses (see their appendix B), and concluded that flux losses should be of the order of 3 per cent for their sample. Before proceeding with the comparison, we discuss an additional piece of evidence suggesting that flux losses are indeed unlikely to dominate the observations in Arrigoni Battaia et al. (2016). In Section 4.1 we have shown that the Ly α extended emission around the targets of our QSO MUSEUM survey peaks at wavelengths close to the maximum of the Ly α emission of the targeted quasars. We have thus checked the velocity separation between the quasar's systemic redshift[13] and the peak of the Ly α line for each of the quasars in Arrigoni Battaia et al. (2016). We have found a median (mean) shift of $\Delta v = -92$ km s^{-1} (-250 km s^{-1}), with only two quasars having a large displacement, $\Delta v = -1468$ km s^{-1} (SDSS J131433.84 + 032322.0) and $\Delta v = -1789$ km s^{-1} (SDSS J085233.00 + 082236.2). Since the quasar's systemic redshifts were chosen to conservatively fit within the NB

[13]In Arrigoni Battaia et al. (2016), the quasar's systemic redshifts are more robust than here (uncertainty of ~ 270 km s^{-1}).
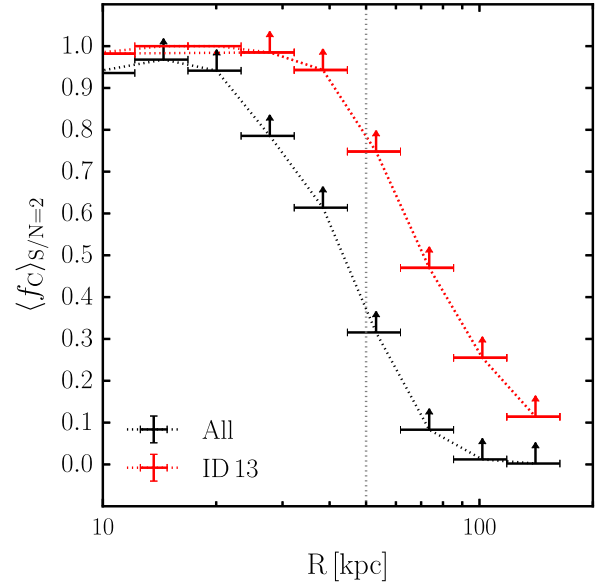

Figure 7. Covering factor of the Ly α emission above S/N > 2 in logarithmic bins around the quasars. To obtain this plot, we use the same circular apertures used for the profiles extraction (see Section 4.1.2). Given that we are not sensitive to very faint Ly α emission (SB$_{\mathrm{Ly}\alpha} \lesssim 10^{-18}$ erg s^{-1} cm^{-2} arcsec^{-2}), we show the data as lower limits: for our whole sample (black) and for the target with ID 13 (or PKS 1017 + 109) (red). For reference, the grey vertical line indicates $R = 50$ kpc.

filter, this occurrence indicates that those observations should not be significantly affected by flux losses at least for 13/15 of the quasars in their sample.

We thus show in Fig. 6 the average profile for the Ly α emission around $z \sim 2.253$ quasars as determined by Arrigoni Battaia et al. (2016) (large orange data points). It appears that $z \sim 3$ quasars are surrounded by a brighter glow in the Ly α line. This is even more evident if we correct the SB of the two data sets for the cosmological dimming, and use the comoving distances instead of the physical ones. We show this comparison in the right-hand panel of Fig. 6. This result has to be verified with more statistical studies of the $z \sim 2$ population, e.g. with KCWI. Nevertheless we discuss the implications of such a finding in Section 5.2.

4.1.4 Averaging covering factor of detected extended Lyman α emission

Given the diversity in morphology of the discovered nebulosities, it is difficult to visually assess which fraction of the area around the quasars contributes to the aforementioned profiles. We have thus complemented the previous analysis by estimating the covering factor in logarithmic bins for the extended Ly α emission above the S/N = 2 threshold used to extract the 3D mask in Section 3.1. Specifically, for each logarithmic bin used for the extraction of the radial profiles in Section 4.1.2, we have simply defined the covering factor f_C as the ratio between the area spanned by the Ly α emission above the S/N = 2 threshold and the total area of that radial bin. We have thus obtained radial profiles for f_C for each discovered Ly α nebulosity.

The average covering factor for our whole sample $\langle f_C\rangle_{\mathrm{S/N}=2}$ is then estimated by averaging with equal weights the information from each individual target. In Fig. 7 we thus show $\langle f_C\rangle_{\mathrm{S/N}=2}$ in logarithmic bins of radius R from the quasar. This covering factor

has to be treated with caution. Indeed, by construction, it depends on the depth of the data set and on the S/N threshold used for the analysis. In addition, close to the quasar position, the morphology of the nebulosities, and thus the area covered by the Ly α emission, are uncertain due to the PSF subtraction. For these reasons, in Fig. 7 the estimated values are formally regarded as a lower limit for the area covered by Ly α emitting gas around our sample of quasars.

Fig. 7 shows that the detected extended Ly α emission covers a fraction >30 per cent for radii $R < 50$ kpc (vertical grey line), while it quickly decreases to lower values at larger distances. For comparison, we show in red the profile of the covering factor for the target with ID 13 (or PKS 1017 + 109), which is associated with an ELAN. This object is clearly characterized by a larger covering factor than the average population, with $f_C > 0.8$ for $R < 50$ kpc, and $f_C > 0.1$ at $R = 140$ kpc (our last bin).

The Quasar Probing Quasar (QPQ) series of papers (e.g. Hennawi et al. 2006b; Hennawi & Prochaska 2013) studied the $z \sim 2$ quasar CGM by using bright background sightlines of higher z quasars as a probe of the foreground quasar halo. These studies have shown that the $z \sim 2$ quasar CGM is permeated by optically thick gas with high covering factor >0.4 out to 200 projected kpc in a ±1500 km s⁻¹ velocity interval (Prochaska et al. 2013a,b). A direct comparison between these absorption studies and our current work is complicated by the differences inherent to these two techniques. Indeed the absorption experiment can only rely on a 1D probe piercing through the studied foreground system. The seeing, the uncertainty on cloud sizes, the fact that one probes the quasar ionizing luminosity or n_H^2 in emission, but optical depth in absorption (Hennawi & Prochaska 2013), and (possibly) the different redshift targeted (see Section 5.2), all hamper a statistical one-to-one comparison. Notwithstanding these uncertainties, our data suggests that the optically thick gas – if present also at $z \sim 3$ in similar quantities – is not responsible for the Lyman α emission at >50 kpc distance from the central quasar as its covering factor is much higher than the one of the emitting gas (at least down to the current SB limits), and such optically thick phase should be bright enough (if illuminated by the quasar) to be detected in our observations as demonstrated in Hennawi & Prochaska (2013). To get similar lower limits on the covering factor at 50 kpc or larger distances as in our data, one would have to consider only the lowest column density systems observed in the QPQ series. We will focus on a detailed comparison between absorption and emission studies (also in individual systems at $z \sim 3$) in future works.

4.2 Compact line emitters associated with the extended Lyman α emission

The targets of QSO MUSEUM have been chosen without any prior constraint on their environment.[14] However, the morphology, extent, and level of the Ly α emission could be influenced by the presence of active companions, satellites, nearby systems, and large-scale structures (e.g. Møller & Fynbo 2001, Cai et al. 2017; Arrigoni Battaia et al. 2018). It has indeed been shown as a tendency of ELANe to be associated with overdensities of galaxies and QSOs (Hennawi et al. 2015; Cai et al. 2017; Arrigoni Battaia et al. 2018, Arrigoni Battaia et al., in preparation). Some of the fields of ELAN

(Hennawi et al. 2015) appear to be even more dense than the fields of HzRGs (Kurk et al. 2000; Miley et al. 2004; Venemans et al. 2007). In this section we thus report on our attempt to find associated compact emitters. Given the depth of our data and the FOV probed, this analysis is not conclusive but is intended as a first attempt to characterizing the small-scale environment in which our objects reside.

To identify galaxies at the same redshift of the targeted quasars, we rely on the identification of emission or absorption lines at the redshift of interest. Specifically, we search for (i) compact continuum sources with clear line features and (ii) compact Ly α emitters (LAEs) whose continuum might have been too faint to be detected in the former case. Thus, here, we do not attempt to obtain the redshift of continuum objects with no clear emissions or absorptions as it would be highly uncertain given the depth of our data. To avoid contamination from the noisy edges of the datacubes, we restrict this analysis to the central 55 arcsec × 55 arcsec (or 418 kpc × 418 kpc).

More specifically, we proceed as follows. First, we obtained a catalogue of continuum source candidates by running CUBEXTRACTOR on the white-light images shown in Fig. 5 with a threshold of 2σ above the background root mean square and with a minimum detection area of 5 pixels. Using the segmentation maps produced by CUBEXTRACTOR, we have then extracted the 1D spectra for each identified source from the MUSE datacubes, resulting in an average of 54 sources per field for a total of 3280 sources. The inspection of such spectra has been conducted to identify emission or absorption within ±3000 km s⁻¹ from the systemic redshift of each targeted quasars. This large velocity window should allow us to find systems associated with most of the quasars and nebulosities even though their current redshifts significantly differ (see Table 1 and Section 4.1). This search resulted in the discovery of 11 continuum selected sources characterized by some line emission close to the location of expected transitions for the redshift of interest. Apart from the contamination of six foreground objects with detected [O II], or Hδ line emission, we found (i) four active companions with detected Ly α, and tentative C IV, He II, and (ii) one object with only one line emission that we interpreted as Ly α. In addition, for each field, we look for signatures of AGN activity for all the continuum-detected sources, identifying two higher z quasars and one lower z quasar. For all these sources,[15] we show their spectra in Appendix C, while we indicate their positions with the corresponding names on the NB images in Fig. 5, and listed them in Table C2. In particular, we note that the quasar with the larger number (2, of which 1 is a type-I) of active companions detected (ID 13 or PKS 1017 + 109) also presents the more extended and brightest of the Ly α nebulosities (see Arrigoni Battaia et al. 2018).

The aforementioned analysis however misses all the line emitters whose faint continua were not detected in the white-light image. To search for such objects, we run CUBEXTRACTOR to select groups of contiguous voxels within the PSF and continuum subtracted MUSE datacubes. Specifically, we search for line emitters within a window of ±3000 km s⁻¹. To avoid contamination from spurious sources, we conservatively extract candidate sources with a minimum volume of 50 voxels at S/N ≥ 5, and masking the location of residuals from stars that would otherwise contaminate

---

[14]We remind the reader that we selected our targets by avoiding very crowded fields in optical observations (see Section 2). This should not bias our selection as most of the optical sources for which a field result to be crowded at the depth of SDSS-DR12, DSS2, and USNO-A2/B1 are low z objects.

[15]Two companions (AGN1 and QSO2) and the continuum object with Ly α emission (LAE1) have been discovered around the quasar with ID 13, and already reported in Arrigoni Battaia et al. (2018). We do not show them again here (the same applies for LAE2 associated with the same system).
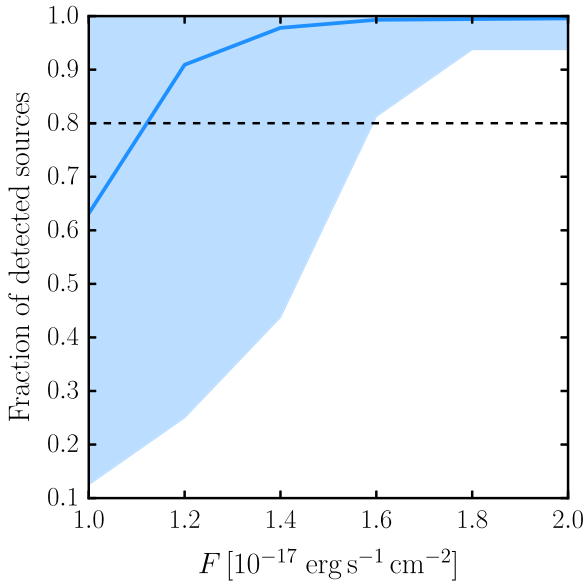
Figure 8. Results of a completeness test for the detection of Ly α emitters associated with the targeted systems. The blue solid line indicates the average recovered fraction, while the blue shaded region indicates the spread between the maximum and minimum of the recovered fraction for the individual fields. With our selection criteria, we are thus ≥ 80 per cent complete for fluxes $> 1.1 \times 10^{-17}$ erg s^{-1} cm^{-2}.

our catalogue. Note that the selected threshold would allow us to surely detect bright ($F > 1.1 \times 10^{-17}$ erg s^{-1} cm^{-2}) line emitters associated with the quasars in most of our fields, if present. We have indeed tested our selection criteria by introducing 100 mock sources with fluxes in the range $(1-2) \times 10^{-17}$ erg s^{-1} cm^{-2} into the PSF and continuum subtracted datacube for each targeted field. Each of the mock sources has a profile defined by a 2D Gaussian in the spatial direction with full width at half-maximum (FWHM) equal to the estimated seeing (on average FWHM =1.07 arcsec), and a Gaussian with FWHM = 2.5 Å in the spectral direction. As it is clear from Fig. 8, the aforementioned selection criteria allow us to be, on average, ≥ 80 per cent complete for line fluxes $F > 1.1 \times 10^{-17}$ erg s^{-1} cm^{-2}. Note however that for ten of our fields, the completeness is ≥ 80 per cent only at higher fluxes $F \gtrsim 1.3 \times 10^{-17}$ erg s^{-1} cm^{-2}.

Applying this method to the data, we identify an average of 1 source per field. To avoid the selection of spurious sources, we have then visually inspected the 'optimally extracted' line flux images, and extracted a 1D spectrum for each of the selected sources. We classify as Ly α emitters only those compact sources that appear to not have other emission lines identifiable as e.g. H α, [O III], H β, [OII]. In addition, for some fields, our selection criteria identify small portions of the Ly α nebulosities. We classify such portions as additional LAEs only when they appear to be compact, centrally concentrated sources. This last choice, which happens in 9 cases out of 20 detected portions of nebulae,[16] has to be confirmed with additional data targeting the continuum emission of such candidate companions.

Following this procedure, we identify a total of 22 LAEs when considering all our sample. We list their coordinates, their redshifts,

[16]LAE2 in ID 8 (or UM683); LAE1, LAE2, AGN1 in ID 13 or (PKS 1017+109); LAE1 and LAE2 in ID 46 (or Q2355+0108); LAE1 in ID 47 (or 6dF J0032-0414); LAE1 and LAE3 in ID 56 (or TEX1033 + 137).

and information on the Ly α line emission in Appendix C, while we indicate them with their respective numbers on the NB images shown in Fig. 5.

Overall, following our selection criteria, most of our fields (48) do not show the presence of LAEs down to our sensitivity limits and apertures used.[17] If we use the luminosity function for field LAEs by Cassata et al. 2011 (bin $3 < z < 4.55$) and assume a comoving volume of 231 Mpc^3 defined by the MUSE FOV and the window of ± 3000 km s^{-1}, we find that we would expect 0.6 ± 0.3 LAEs per field.[18] A similar value, 0.7 ± 0.4, is obtained by adopting the more recent luminosity function of Drake et al. (2017). If we thus take into account the estimates of the expected number of LAEs per field (ranging between about 0.3 and 1) and the fact that we are 80 per cent complete, we obtain a total expected number of LAEs in the range $24 - 30$, not far from the total of 22 found.[19] Therefore, at these luminosities, our quasar environments seem to be similar to the field, suggesting that on average quasars do not inhabit the most dense environments at their redshift (Trainor & Steidel 2012b; Fanidakis et al. 2013). Nevertheless, the fields with more than one detection are clear outliers, and probably reflect the presence of underlying overdensities and/or effects of powering mechanisms, e.g. chance alignment between the position of the LAE and the ionization cones of the quasars (e.g. Haiman & Rees 2001).

Some of the detected LAEs, especially the one with high equivalent widths (EW$_{rest}$ > 240 Å; Cantalupo, Lilly & Haehnelt 2012) might indeed represent candidates for the so-called 'dark galaxies', i.e. dense pockets of gas fluorescently illuminated by the targeted quasars (e.g. Haiman & Rees 2001). Using the luminosity function from Cantalupo et al. (2012), who reported candidate LAEs[20] around one $z \sim 2.4$ hyperluminous quasar (bolometric luminosity $L_{bol} > 10^{47}$ erg s^{-1}), we would expect to see 1 LAE per field above our luminosity limit.[21] Cantalupo et al. (2012) found indeed only 1 LAE with luminosity high enough to be detected by our observations, and at a 'MUSE distance' from the quasar. This LAE has an exceptional EW$_{rest}$ = 327 ± 28 Å. Recently, Marino et al. (2018) also searched for 'dark galaxy' candidates with deep MUSE observations around a sample of 5 QSOs (4 at $z \gtrsim 3.7$ and 1 at $z \approx 3.2$) and 1 type-II AGN. Unfortunately, from the unprecise redshifts reported for their LAEs in their Table 5, we are not able to verify how many LAEs they detected down to our luminosity limit and within our velocity window for the whole sample. However, we can see that they detected only two LAEs for their four QSOs at $z \gtrsim 3.7$ matching our criteria (see their Fig. 7, right-hand panel). Both of these sources are classified as candidate 'dark-galaxies' (see their Table 3). On the contrary, no bright 'dark-galaxy' candidates are reported within ± 3000 km s^{-1} for their $z \approx 3.2$ QSO (see their Table 3 and Fig. 4). In our sample, we only have 1 LAE (LAE2 in the SDSS J1209 + 1138 field; see Table C1) with an exceptional equivalent width of EW$_{rest}$ > 420 Å that could be considered as a

[17]For the quasar with ID 58 (Q1205-30) we were able to compare our analysis with NB data reaching the same depth (Fynbo, Thomsen & Møller 2000; Appendix C), confirming that there are no LAEs in this particular field down to out limits.

[18]The errors listed for the expected number of LAEs in this paragraph encompass the different estimates due to the sensitivity of each individual field, log($L_{Ly\alpha}$/[erg~s^{-1}]) = 42 − 42.1.

[19]Note that also the five objects with continuum detection reported in this section (4 companions + 1 Ly α emitter) could be classified as LAE from their Ly α EW$_{rest}$, summing up to 27 LAEs in total.

[20]The LAEs in Cantalupo et al. (2012) are not spectroscopically confirmed.

[21]Note however that not all our quasars are hyperluminous.

Table 5. Exponential fit of the Ly α surface brightness profiles of the two radio-quiet subsamples after correction for SB dimming and normalization of physical distance with $R_{\rm vir}$ (right-hand panel in Fig. 13).

Sample	#	$\langle z_{\rm Ly\alpha} \rangle$	$C_{\rm e}^a$ (10^{-14})	$x_{\rm h}^a$	$\chi_{\rm e}^{2\ b}$
Higher z^c	18	3.336	1.95	0.16	7.1
Lower z^c	17	3.114	1.36	0.15	0.3

Notes. ^{a}Best-fitting parameters assuming SB profile $SB(x) = C_{\rm e} \exp(-x/x_{\rm h})$, where $x = R/R_{\rm vir}$. $C_{\rm e}$ is in unit of 10^{-14} erg s^{-2} cm^{-2} arcsec^{-2}. Note that the SB has been multiplied by $(1 + z)^4$ before the fit (Fig. 13).
^{b}Reduced chi square for the exponential fit.
^{c}Both subsamples include only radio-quiet quasars (see Section 5.2 for details on the selection).

'dark-galaxy' candidate as usually done in the literature. We conclude that object-to-object variations can play an important role at these high luminosities, and within our small FOV, explaining the difference with Cantalupo et al. (2012).

Finally, we stress that the analysis presented in this section is inevitably limited in identifying companions within the Ly α nebulosities themselves, unless they are characterized by a brighter emission than the extended Ly α. We thus do not exclude the presence of faint galaxies embedded within the extended Ly α emission surrounding each quasar in our sample.

4.3 Kinematic information from the extended Lyman α emission

In this section we present the maps for the flux-weighted velocity centroid and the flux-weighted velocity dispersion of the extended Ly α emission calculated as explained in Section 3.1 (following the same analysis of Borisova et al. 2016). We reiterate that we do *not* fit any function to the line profile to avoid neglecting fundamental information on the gas properties imprinted by the Ly α resonant scattering, which is likely in play here.

Fig. 9 shows the atlas of the 61 maps for the flux-weighted velocity centroid with respect to $z_{\rm peak\ Ly\alpha}$ (Table 1).[22] In agreement with Borisova et al. (2016), the majority of the maps looks noisy and difficult to interpret as ordered motions of any kind (rotation, infall, or outflow), though each nebulosity shows peculiar structures. On the other hand, the largest and brightest nebula (ID 13) show a remarkable velocity pattern on hundreds of kpc, with the furthest portion clearly redshifted. This coherent velocity pattern has been interpreted as signature of inspiraling motions within the quasar's halo (Arrigoni Battaia et al. 2018).

The difference in complexity between the maps of very extended neulosities and smaller systems could be due to the resonant nature of the Ly α line which sample more turbulent regions on scales of tens of kpc. Such small scales around the quasars are likely more affected by both turbulent motions due to galaxy formation processes (feedback, interactions) and the resonant scattering of Ly α photons coming from the quasar itself (see Section 5.3 for further discussion).

Fig. 10 shows the atlas of the 61 maps for the flux-weighted velocity dispersion. In the bottom left corner of each image we indicate the average velocity dispersion $\langle \sigma_{\rm Ly\alpha} \rangle$ within each nebulosity. We

---

[22]Following the analysis in Section 4.1, all the discovered Ly α nebulosities would appear mainly as red in Fig. 9, i.e. as largely redshifted, if the flux-weighted velocity centroid would have been calculated with respect to the quasars systemic redshifts (see Fig. 3 for the velocity shifts).

find that the extended Ly α emission has $\langle \sigma_{\rm Ly\alpha} \rangle < 400$ km s^{-1} (or FWHM < 940 km s^{-1}) in all the cases, irrespective of the radio-loudness of the targeted quasars. These estimates are similar to the velocity widths observed in absorption in the CGM surrounding $z \sim 2$ quasars ($\Delta v > 300$ km s^{-1}; Prochaska & Hennawi 2009; Lau et al. 2018).

As done in Lau et al. (2018), we can compare these values with the expected velocity dispersion for a dark matter halo hosting quasars. In particular, it has been found that the maximum of the average 1D root-mean-square (rms) velocity $\sigma_{\rm rms\text{-}1D}$ is related to the maximum circular velocity within a dark matter halo by $\sigma_{\rm 1D} = V_{\rm circ}^{\rm max}/\sqrt{2}$ (Tormen, Bouchet & White 1997). If we assume dark matter haloes of $M_{\rm DM} \sim 10^{12.5}$ M$_\odot$ (White et al. 2012) at $z \sim 3$, an NFW profile (Navarro, Frenk & White 1997) with a concentration parameter of $c = 3.7$ (Dutton & Macciò 2014), the maximum circular velocity is $V_{\rm circ}^{\rm max} = 360$ km s^{-1}. Hence $\sigma_{\rm rms\text{-}1D} = 250$ km s^{-1}. The motions within all these Ly α nebulae have thus amplitudes consistent with gravitational motions expected in dark matter haloes hosting quasars, with part of the velocity dispersion likely due to Ly α resonant scattering and instrument resolution (FWHM ≈ 2.83 Å or 170 km s^{-1} at 5000 Å).

To check for any dependence on the quasar luminosity and on the strength of the radio emission, in Fig. 11 we plot the average flux-weighted velocity dispersion for each nebulosity as a function of $M_i(z = 2)$ for each targeted quasar. On the same plot, we differentiate between objects with measured radio fluxes and radio-quiet object (red and blue), and use larger symbols for quasars characterized by stronger radio emission. It is clear that there are no trends in both luminosity or radio strengths, confirming that the mechanisms responsible for the broadening of the Ly α line on 50 kpc scales do not depend on these properties for at least our observed ranges ($F_{\rm Radio} < 900$ mJy; $M_i(z = 2) \gtrsim -29$ for radio-loud objects, and $M_i(z = 2) > -29.7$ for radio-quiet).

We note however that the relatively quiescent Ly α nebulosities around all the 15 radio-loud quasars in our sample run counter to the two radio-loud systems with $\sigma > 425$ km s^{-1} (or FWHM > 1000 km s^{-1}) showed by Borisova et al. (2016). Specifically, the two radio-loud objects in Borisova et al. (2016), PKS 1937-101 and QB 2000-330, have a peak flux at 1.4 Ghz of 838.8 ± 25.2 mJy and 446.8 ± 15.7 mJy (Condon et al. 1998), and a magnitude of $M_i(z = 2) = -30.35$ and -29.77, respectively. Even though we have in our sample quasars as strong in radio emission as these two, i.e. ID 49 and 54 (>700 mJy), our quasars are 2.4 magnitudes fainter and show $\langle \sigma_{\rm Ly\alpha} \rangle = 221$, and 287 km s^{-1} (or FWHM = 519, and 647 km s^{-1}). This difference thus suggests that – if an outflow is present in the radio-loud systems – (i) the winds are driven by the radiative output of the AGN rather than by a jet, and/or (ii) the coupling between the Ly α emitting gas on large scales (tens of kpc) and an outflow is more effective around more luminous AGN, and/or (iii) more luminous radio-loud AGN are able to sustain coherent winds (or jets) for longer time-scales.

It is interesting to note that also in the radio-quiet population there can be extended Ly α nebulosities showing broad emission. In particular, Borisova et al. (2016) showed one radio-quiet quasar in their sample, J0124 + 0044 ($z = 3.783$), with broad extended Ly α emission. The statistics from our work together with Borisova et al. (2016) suggests a very low rate, 1 out of 56 (39 + 17), which seems to not depend on the current quasar luminosity.[23] We further discuss

---

[23]The object in Borisova et al. (2016) with broad Ly α emission has $M_i(z = 2) = -28.98$
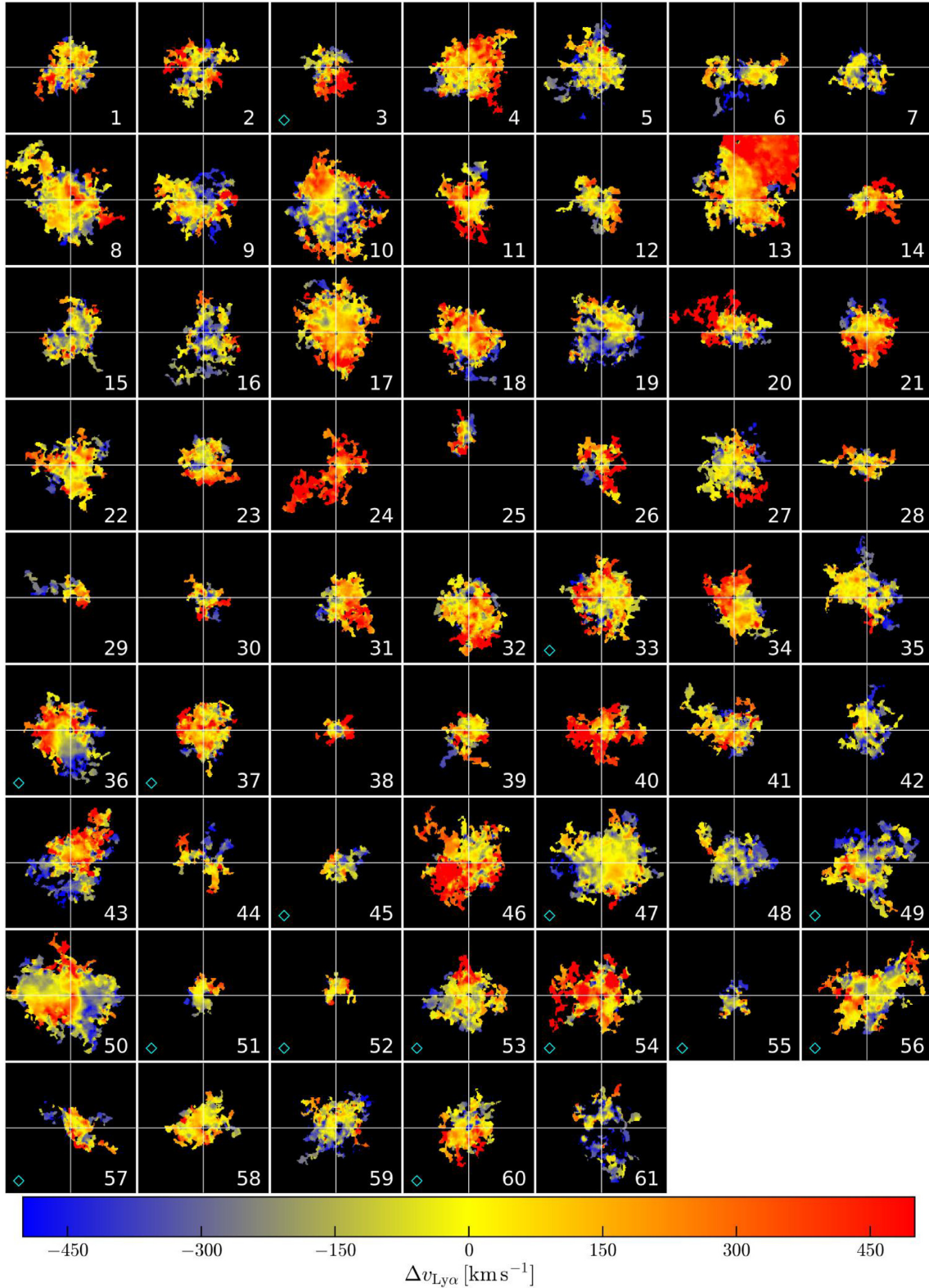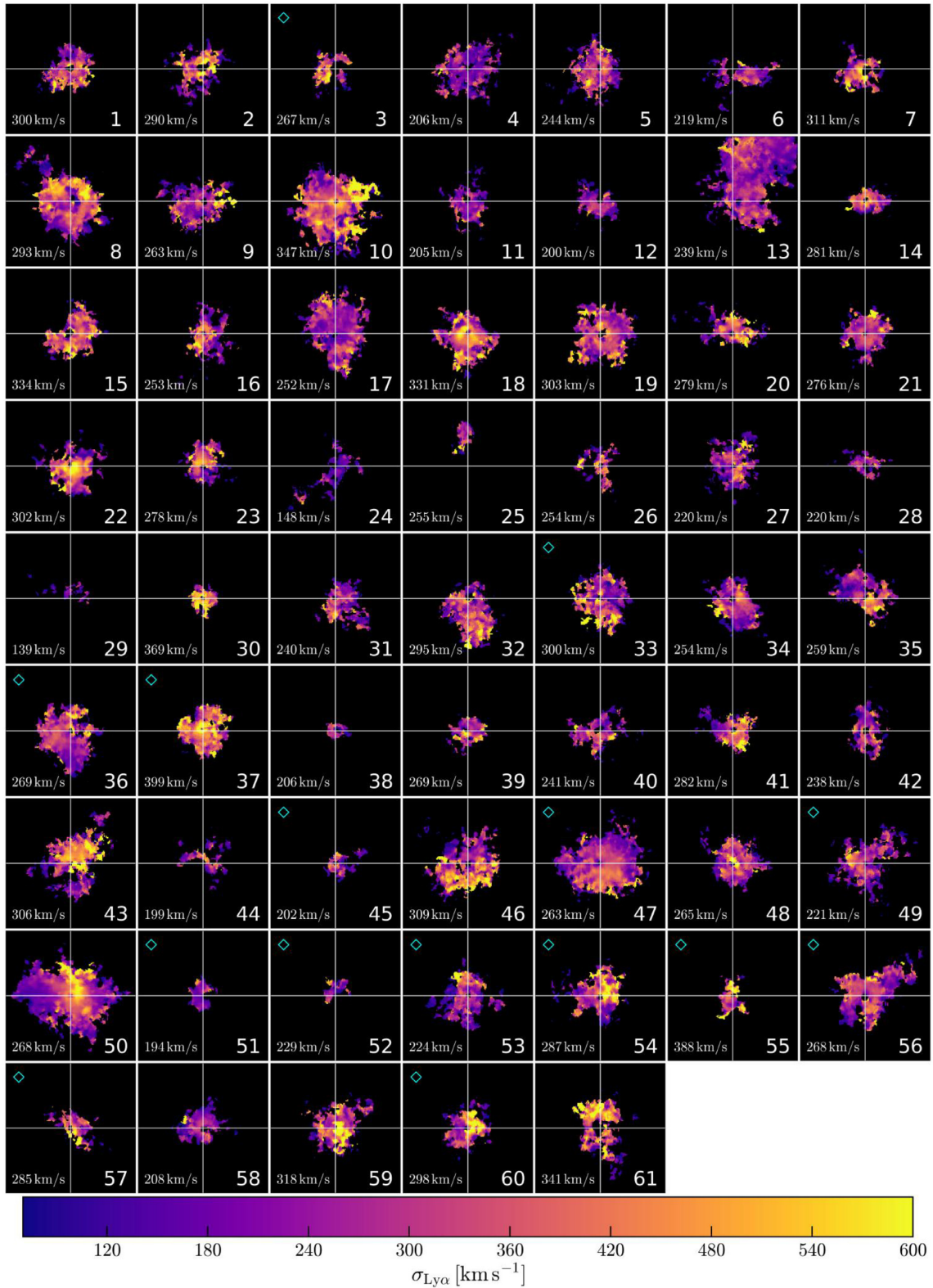
Figure 9. Atlas of the 61 maps for the flux-weighted velocity centroid of the Ly α emission around the quasars in the QSO MUSEUM sample. The flux-weighted centroid is calculated as first moment of the flux distribution with respect to the peak of the Ly α emission of each nebulosity $z_{\mathrm{peak\,Ly\alpha}}$ (Table 1). Each image is presented on the same scale of Fig. 1, 30 arcsec × 30 arcsec (or about 230 kpc × 230 kpc), even though we use only the information within the extracted 3D masks to compute these 'velocity maps' (see Section 3.1). In each image the white crosshair indicates the position of the quasar prior to PSF subtraction. A cyan diamond in the bottom left corner indicates that the quasar is radio-loud. The detected extended Ly α emission shows complex and noisy maps on tens of kpc, while it shows more coherent patterns on larger scales (see ID 13).

Figure 10. Atlas of the 61 maps for the flux-weighted velocity dispersion of the Ly α emission around the quasars in the QSO MUSEUM sample. The velocity dispersion is calculated as second moment of the flux distribution. Each image is presented on the same scale of Fig. 1, 30 arcsec $\times$ 30 arcsec (or about 230 kpc $\times$ 230 kpc), even though we use only the information within the extracted 3D masks to compute these 'velocity-dispersion maps' (see Section 3.1). In each image the white crosshair indicates the position of the quasar prior to PSF subtraction. A cyan diamond in the top left corner indicates that the quasar is radio-loud. We indicate in the bottom left corner of each image the average velocity dispersion $\langle \sigma_{Ly\alpha} \rangle$ for each map. The extended Ly α nebulae show an average velocity dispersion $\langle \sigma_{Ly\alpha} \rangle < 400 \, \mathrm{km \, s^{-1}}$ (or FWHM $< 940 \, \mathrm{km \, s^{-1}}$), irrespective of the radio-loudness of the targeted quasars.
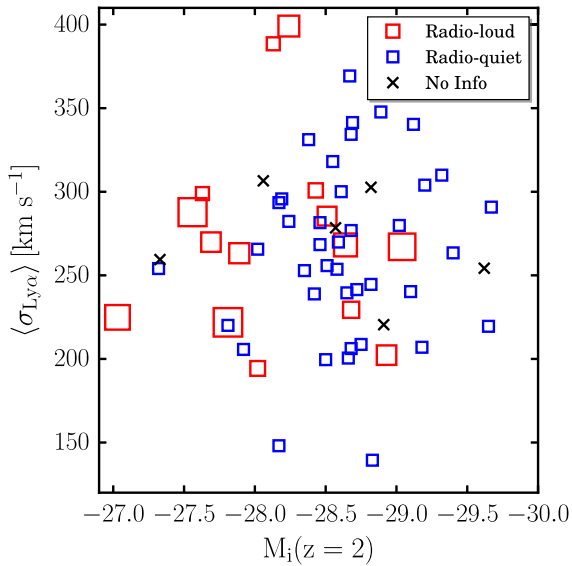
Figure 11. Plot of the average flux-weighted velocity dispersion $\langle \sigma_{\text{Ly}\alpha} \rangle$ of each Ly α nebulosity versus the absolute i-band magnitude normalized at $z = 2$, $M_i(z = 2)$, using Ross et al. (2013). We indicate in blue the radio-quiet systems, while in red the radio-loud objects. The size of the symbol for the radio-loud objects symbolizes the flux listed in Table 1, i.e. larger symbols mean larger fluxes following the relation size$_{\text{radio}}$ = size$_{\text{quiet}}$ + $5 \times \log(F_{\text{Radio}})$. The crosses indicate the objects for which we do not have information on their radio flux. The average flux-weighted velocity dipersion do not depend on the current quasar luminosity or strength of radio emission.

these rare broad extended Ly α nebulosities (for both radio-quiet and radio-loud systems) in Section 5.4.

4.4 Spectral shape and asymmetry of the extended Lyman α emission

As the Ly α photons are expected to experience frequency excursions in the scattering process (Dijkstra 2017 and references therein), and the resulting change in frequency depends both on local and unrelated structures, the shape of the Ly α line can be fundamental in understanding the astrophysics of the studied system, e.g. presence of inflows/outflows (e.g. Laursen, Razoumov & Sommer-Larsen 2009), absorption from the foreground IGM. For this reason, it is particularly important to quantify the asymmetries of the Ly α line profile, and/or the presence of different peaks (e.g. Gronke & Dijkstra 2016).

Unfortunately, our data lack the necessary sensitivity to clearly assess the presence of asymmetric wings in the line profile. This has been indeed tested by calculating the third moment of the flux distribution for the extended Ly α emission as done for the smaller moments, leading to poorly constrained and inconclusive values. By averaging over the whole nebulae we could achieve higher sensitivity, but we would complicatedly mix, and washed out the low S/N features we are looking for.

In addition, we do not detect clear double-peaks profile – expected in the case of optically thick gas (e.g. Neufeld 1990) – in any of the discovered Ly α nebulosities. However, this result may be driven by the spectral resolution of MUSE at these wavelengths (FWHM $\approx$ 2.83 Å or 170 km s^{-1} at 5000 Å).

Therefore, for this kind of detailed analysis, we would need a data set with a much higher S/N for the wings of the Ly α emission,

and with higher spectral resolution. Now that the level of the Ly α emission is known, we can plan such experiments.

5 DISCUSSION

From the analysis presented in the previous sections, it is clear that we have detected extended Ly α emission on tens of kpc scales around each of the targeted quasars. In this section we discuss some of the implications of the observations presented in this work, relying only on the information coming from the Ly α emission. In future studies, we will revisit these points with the use of additional diagnostics.

5.1 Small detection rate for enormous Lyman α nebulae

Recent observations have shown the existence of ELAN (Cantalupo et al. 2014; Hennawi et al. 2015; Cai et al. 2017; Arrigoni Battaia et al. 2018) extending for hundreds of kpc around $z \sim 2$ quasars, with SB$_{\text{Ly}\alpha} \sim 10^{-17}$ erg s^{-1} cm^{-2} arcsec^{-2}. Current statistics suggest that the ELAN are very rare structures that are found around a few per cent of the targeted radio-quiet quasars at $z \sim 2$ (Hennawi & Prochaska 2013; Hennawi et al. 2015). One of the aim of the QSO MUSEUM survey, together with ongoing efforts (e.g. Cai et al. 2018), is to better characterize the frequency of this phenomenon, and understand why these nebulae are so uncommon (e.g. presence of companions, halo mass, illumination).

Thanks to our QSO MUSEUM survey, and the previous work of Borisova et al. (2016), we have now amassed a sample of 80 (61 + 19) quasars at $z \sim 3$ down to SB$_{\text{limit}} \sim$ few $\times$ 10^{-18} erg s^{-1} cm^{-2} arcsec^{-2}. Of all these quasars, only one object shows the extreme observed surface brightnesses and extents found in the ELAN at $z \sim 2$, i.e. the ID 13 in this work or PKS 1017 + 109. All the other nebulosities show lower levels of Ly α emission or extends only to much smaller distances from the central quasar down to the same SB limits (see Fig. 4). The ELAN around the quasar PKS 1017 + 109 has been studied in detail in Arrigoni Battaia et al. (2018), where we have indicated the common peculiarities with the other ELAN discovered at $z \sim 2$, with particular emphasis on the identification of active companions in their surroundings.

It has been proposed that the higher SB$_{\text{Ly}\alpha}$ in these ELAN traces patches with higher volume densities than the average population at both redshifts (Hennawi et al. 2015; Arrigoni Battaia et al. 2016) and/or gas reprocessing the additional contribution to the ionizing radiation from the active companions (Arrigoni Battaia et al. 2018) in the environment of ELAN. The higher density patches could be due to substructures interacting with the main halo hosting the targeted quasars (Arrigoni Battaia et al. 2018).

Further, to clarify how easy it is to detect ELAN with current facilities and how a detected Ly α nebulosity around a quasar could 'grow' with longer integration times, in Fig. 12 we show the histogram of the area spanned by each of the Ly α nebulosities in our sample for different S/N detection threshold (the different colours). For each histogram, we indicate the position of the nebula around the quasar with ID 13, or PKS 1017 + 109 (Arrigoni Battaia et al. 2018). It is clear that ELAN are clearly visible as extended objects even with shorter integration times than used here, as the area for S/N = 10 is already >200 arcsec^2 for ID 13. In the same figure, an additional x-axis indicates the corresponding radius for a circular nebula with the same area, i.e. $R = \sqrt{(\text{Area}/\pi)}$. Even with the threshold of S/N = 10 this ELAN has $R > 60$ kpc.

The plot in the inset of Fig. 12 shows how the area grows for each nebulosity as a function of S/N with respect to the area for

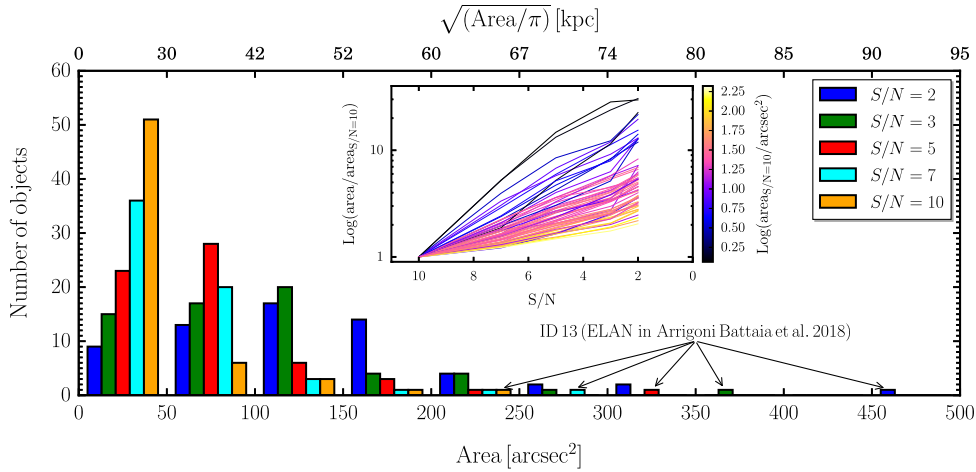**Figure 12.** Histogram of the variation of the area for each Ly α nebulosity for different S/N thresholds (different colours as indicated in the legend). The ELAN discovered in QSO MUSEUM is indicated with arrows. The plot in the inset shows the logarithmic variation of the area (normalized to the area for S/N = 10) of the Ly α nebulae with respect to the S/N threshold. In this plot, we colour-coded the lines for each nebula following the area for S/N = 2 as listed in Table 3. This plot clearly states that ELAN can be detected with very fast integrations with current facilities. Smaller Ly α nebulae have the potential of 'growing' faster than ELAN when the exposure time is increased, probably reflecting the different scales sampled (CGM versus CGM + IGM).

S/N = 10. In the same plot, we colour coded the line for each Ly α nebula depending on the final observed area for S/N = 2. This plot shows that the nebulae with the larger sizes (lines with lighter colours) do not increment their extent as fast as smaller nebulae if deeper observations are conducted. This occurrence could reflect the different scales probed by the different nebulae. Indeed, while small Ly α nebulae most probably trace the gas within the central portion of the dark matter halo hosting a quasar, nebulae with 100 kpc sizes start to probe IGM regions where the densities are expected to be lower. This has also been the case for the nebula around UM 287 (Cantalupo et al. 2014), which was detected after only 20 min of NB imaging with the Low Resolution Imaging Spectrograph (Oke et al. 1995) instrument on the Keck telescope. The size of the nebula did *not* increase significantly with the total observing time acquired in those observations of ∼10 h.

If the relation for the large nebulosities shown in the inset of Fig. 12 holds for even larger areas, one would need to increase the S/N by a factor of 8 to roughly double the detected area. This would then require additional ∼64 h on a previously detected 200 arcsec² Ly α nebula in data as deep as our survey. However, the characteristics of the powering mechanisms and the volume density of the gas can both change on larger scales, most probably requiring longer integration times to detect the IGM.

5.2 Is there a redshift evolution of extended Lyman α emission around quasars?

As anticipated in Section 4.1.3 and shown in Fig. 6, the current observations of Ly α haloes around radio-quiet quasars hint to a clear difference between the $z \sim 3$ and $z \sim 2$ population. Indeed, the Ly α emission seems to be much stronger at $z \sim 3$ than at $z \sim 2$, maybe suggesting a larger mass in the cool ($T \sim 10^4$ K) phase of the CGM at $z \sim 3$ than at $z \sim 2$ ($M_{cool} > 10^{10}$ M⊙; Prochaska et al. 2013a, 2014). Here we investigate this hypothesis.

To further check the presence of a redshift evolution, we split our large sample of radio-quiet quasars into two redshift bins, and look for any trend that would confirm the strong difference between $z \sim 2$ and $z \sim 3$. Given the large uncertainties on the systemic redshift of our sample (see Section 3.2), we built the two redshift

bins by maximizing the number of objects in each bin, while excluding quasars whose redshift is so uncertain that they could sit in the other bin both because of the uncertainty on the systemic redshift $z_{systemic}$, and/or the difference in redshift between the Ly α nebula $z_{peak Lyα}$ and $z_{systemic}$. We find that a cut $z_{peak Lyα} < 3.191$ and $z_{peak Lyα} > 3.229$ satisfies our conservative criteria, resulting in two almost equally populated subsamples of 17 and 18 objects each, respectively. The selected quasars cannot change their bin even with a 3σ deviation from their current redshift. The median redshift for the two samples is $z_{low} = 3.114$, and $z_{high} = 3.336$. Such a redshift difference corresponds to about 0.15 Gyr in the standard cosmology assumed in this work. For each bin, we then computed the average profile as performed in Section 4.1.3.

The left-hand panel in Fig. 13 shows the comparison of the average surface brightness profiles for the two redshift bins with the profile for the whole sample, and the profile at $z \simeq 2.25$ (Arrigoni Battaia et al. 2016) after correcting all for the SB dimming. A difference between the higher and the lower redshift bin is evident, with the lower-z profile being always below the data points for higher-z. The average ratio between the data points for the two subsamples is 1.5 ± 0.1, while the profile for $z \simeq 2.25$ is a factor of about 17 ± 8 lower (two central points) with respect to the lower z subsample. These differences are thus significant given the estimated uncertainties.

What is the cause of such strong variations? We first explore the possibility that such differences are due to the cosmological evolution of densities and scales. Mas-Ribas & Hennawi (2018) investigated the redshift scaling of a low SB signal in the case of electron-scattering around quasars. They show that the cosmological evolution of densities and scales cancel out the cosmological effect of surface brightness dimming $(1 + z)^{-4}$ in their particular case. Here, we perform a similar calculation, but in the case of Ly α emission from gas clouds that are optically thin to Lyman continuum photons (neutral Hydrogen column density $N_{H I} \ll 10^{17.2}$ cm⁻²). This emission scenario is indeed the most favoured scenario for extended Ly α emission around AGN (e.g. Heckman et al. 1991a; Arrigoni Battaia et al. 2015, 2016; Cai et al. 2017; see also discussions in Hennawi & Prochaska 2013; Cantalupo et al. 2014).
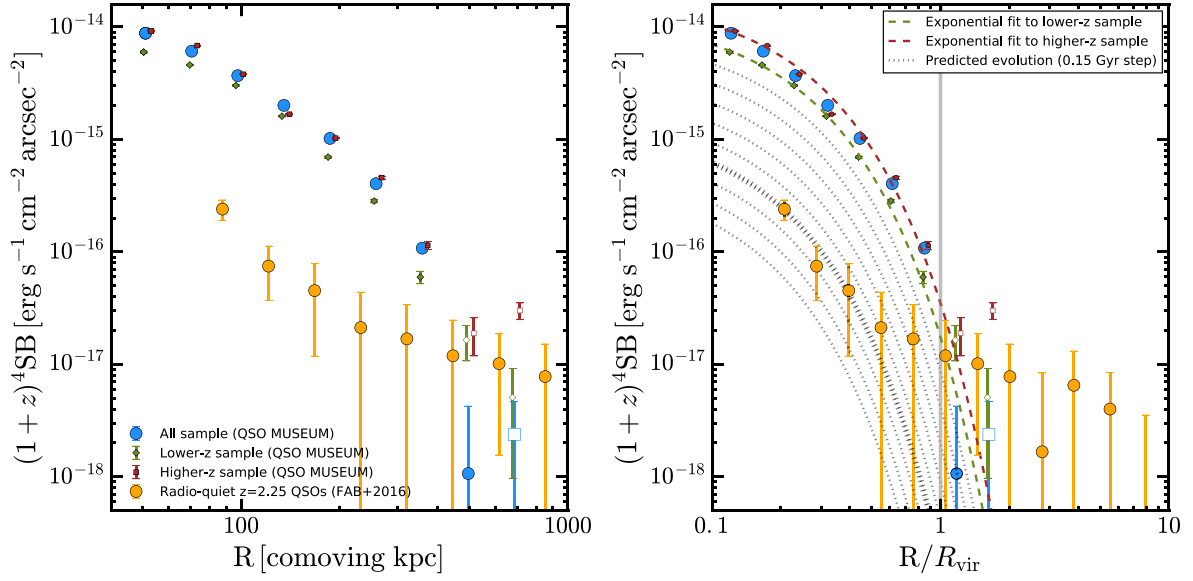
Figure 13. Redshift evolution of Ly α emission around quasars. Left-hand panel: we show the average profile for the whole sample (large blue; 61 targets), the radio-quiet lower z subsample (small dark green diamond; 17 quasars), and radio-quiet higher z subsample (small brown squares; 18 quasars) after correcting the SB for the cosmological dimming and using comoving units for the radii. For each profile, open symbols indicate negative data points. We compare our data set with the average profile for $z \simeq 2.25$ quasars by Arrigoni Battaia et al. (2016). Right-hand panel: the average SB profiles presented in the left-hand panel are now plotted with respect to the proper radius normalized to the virial radius $R_{\rm vir} = [3M_{\rm halo}/(800\pi\,\rho_{\rm crit}(z))]^{1/3}$ expected for haloes hosting quasars at these redshifts (see Section 5.2 for details). We show the best exponential fit to the two subsamples (coloured dashed lines). Using the ratio between the parameters of these two fits we predict the evolution for lower-redshifts in steps of about 0.15 Gyr (dotted lines). The thicker dotted line corresponds to about 1.05 Gyr, the difference between the higher z subsample and $z \simeq 2.25$. For reference, the grey vertical line indicates 1 Rvir. Our observations thus suggest a clear evolutionary trend (see Section 5.2 for discussion).

Following the formalism in Hennawi & Prochaska (2013), the observed Ly α surface brightness in an optically thin scenario scales as $\mathrm{SB}_{\mathrm{Ly}\alpha} \propto (1+z)^{-4} n_{\rm H} N_{\rm H}$, where $n_{\rm H}$ is the Hydrogen volume density, and $N_{\rm H}$ is the Hydrogen total column density. It can be shown that $N_{\rm H} \propto n_{\rm H} R_{\rm vir}$ (see e.g. equation 2 in Hennawi & Prochaska 2013), where $R_{\rm vir}$ is the virial radius of the quasars' halo, $R_{\rm vir} \equiv R_{200} = [3M_{\rm halo}/(800\pi\,\rho_{\rm crit}(z))]^{1/3}$.[24] To compute the dependence with redshift we thus need an estimate of the quasars' halo mass at the redshifts of interest. The current consensus in the literature indicates that quasars at $z \sim 2$ and $z \sim 3$ inhabits dark-matter haloes with similar masses ($M_{\rm halo} = 10^{12.5}\,{\rm M}_\odot$) independent of their luminosities, though with large uncertainties (e.g. da Ângela et al. 2008; Kim & Croft 2008; Trainor & Steidel 2012a; White et al. 2012). If we then assume the same halo mass for the different redshifts, $R_{\rm vir}$ changes only because of the evolution of the critical density $\rho_{\rm crit}(z)$, thus increasing by a factor $(1+z)$ towards lower redshifts. Therefore, because the cosmological evolution sets $n_{\rm H} \propto (1+z)^3$, and $N_{\rm H} \propto n_{\rm H} R_{\rm vir} \propto (1+z)^2$, we find an overall scaling of $\mathrm{SB}_{\mathrm{Ly}\alpha} \propto (1+z)$ or $\mathrm{SB}_{\mathrm{Ly}\alpha}^{\rm no\ dimming} \propto (1+z)^5$ when taking out the factor for the SB dimming as in Fig. 13. If the changes in the Ly α profiles were caused simply by the cosmological evolution of density and scales, we would thus expect a ratio of 1.3 and 3, respectively, between the two subsamples at $z \sim 3$, and between $z \simeq 2.25$ and the lower z subsample. These values differ with the aforementioned observed ratios (1.5 ± 0.1 and 17 ± 8), suggesting that the profile evolution is much stronger than expected from the cosmological density evolution. This result matches well with the high densities ($n_{\rm H} >$

1 cm^{-3}) invoked to explain the levels of the observed Ly α emission (Heckman et al. 1991a; Cantalupo et al. 2014; Arrigoni Battaia et al. 2015; Hennawi et al. 2015). Such a high density gas most likely does not trace the evolution of the cosmic mean density.

We then focus on physical processes that could act on CGM scales. To have a better handle on the profiles evolution on such scales, we plot the SB values with respect to the physical distance normalized to the virial radius of the quasars' halo at each redshift, $R_{\rm vir}$. As previously done, we assumed the same halo mass for the redshift subsamples, finding $R_{\rm vir}^{z\sim2} \simeq 130$ kpc and $R_{\rm vir}^{z\sim3} \simeq 100$ kpc, respectively, for $z \simeq 2.25$ and $z \sim 3$. The right-hand panel of Fig. 13 shows this test. At $z \sim 3$ the exponential behaviour of the SB profiles now seems to well describe the presence of emitting gas within a halo of radius $R_{\rm vir}$, with a consequent dimming of the Ly α emission at larger distances. At $z \sim 2$ the Ly α emission seems instead more concentrated in the central portion of the haloes, with tentative indications of a fainter signal at larger separations.

To quantitatively constrain the difference between profiles and check if there is any relation between their shapes, we proceed as follows. First, we fit the two subsamples at $z \sim 3$ with an exponential function $\mathrm{SB}(x) = C_{\rm e} \exp(-x/x_{\rm h})$ (coloured dashed lines in Fig. 13 and Table 5). Being ≈ 0.15 Gyr one from the other, the ratio between the parameters of these profiles ($C_{\rm e}$ and $x_{\rm h}$) could define a trend for the evolution towards lower z. We then construct other exponential functions by using such ratios (thus in steps of 0.15 Gyr; dotted lines in the right-hand panel of Fig. 13). A profile at $z = 2.25$ should be at 1.05 Gyr (or about seven steps; thicker dotted line) from the profile of the higher z sample. Surprisingly we find the data points of Arrigoni Battaia et al. (2016) at this location. Fig. 13 thus shows a striking agreement between the profile reported by Arrigoni Battaia et al. (2016) and the predictions based on $z \sim 3$. The difference we

---

[24]Here we use as virial radius the radius R_{200} at which the average density of a matter overdensity is 200 times the cosmic mean density.

detect for the subsamples at $z \sim 3$ is then possibly due to the same physical mechanism(s) that cause the difference between $z \sim 3$ and $z \sim 2$, and these most likely act on CGM scales.

Given the currently favoured optically thin scenario for the Ly α emission, the abrupt decrease in $SB_{Ly\alpha}$ – which follows $SB_{Ly\alpha} \propto n_H N_H$ – could be due to a strong variation in n_H and/or N_H. We have shown however that variations in densities have to be larger than the cosmological density evolution, making it unlikely that only variations in n_H are responsible for the differences between $z \sim 2$ and $z \sim 3$. Variations in N_H – or in other words in the mass of the cool optically thin gas phase within the CGM, $M_{cool} \propto N_H$ (e.g. Hennawi & Prochaska 2013) – are thus a more plausible explanation.

Intriguingly, theoretical works have predicted just such a scenario for haloes with masses above the critical halo mass for shock stability $M_{shock} \simeq 10^{12}$ M$_\odot$ (roughly constant with redshift; Dekel & Birnboim 2006; Dekel et al. 2009). As mentioned above, the quasars here studied should be indeed in this regime. In this theoretical framework, if $M_{halo} > M_{shock}$ there are two possible scenarios for the CGM: (i) the presence of cool streams embedded in a hot phase, and (ii) the prevalence of the hot phase. The smooth transition between these two scenarios, or the maximum halo mass for cold streams, is a function of redshift, and is set by the shock stability criterion for the cool streams to balance the virial shock-heating (see Section 4.3 in Dekel & Birnboim 2006). At the quasar's halo mass at $z \sim 2$ and $z \sim 3$, $M_{halo} = 10^{12.5}$ M$_\odot$, the threshold between the two scenarios is at $z = 2$ (see fig. 7 in Dekel & Birnboim 2006). As one expects a smooth transition from the presence of cool streams to their absence, we conclude that the observed decrease in Ly α emission around quasars from $z \sim 3$ to $z \sim 2$ could be due to this phenomenon, namely the inability of cool dense gas to survive the shock-heating process in similarly massive haloes at lower z. It is important to stress that this scenario would hold for any powering mechanism for the Ly α emission (see Section 5.3). In other words, a decrease with redshift in the mass of the cool gas component within the CGM would result in a decrease of the level of Ly α emission.

Finally, our result could be linked to the evolution of the space density of bright quasars as a function of redshift (e.g. Richards et al. 2006). It has been shown indeed that the space density of quasars steadily increases from $z = 5$ to lower redshifts, peaking between redshift $z = 2$ and $z = 3$. After this peak, the space density drops significantly, reaching at $z = 1$ roughly the same value of $z = 5$ (e.g. fig. 20 in Richards et al. 2006). This trend, together with the level of star-formation of the quasars' hosts, could be related to the drastic changes within the quasars CGM that we start to witness. If the cool phase within the CGM cannot be replenished by infalling gas from the IGM or from the transformation of hot gas into cool gas within the CGM, the mass of cool CGM gas would thus drastically decrease, probably preventing future episodes of quasar activity as this gas is also the fuel for the high star-formation rates estimated for quasars' hosts (e.g. Rosario et al. 2013). This scenario finds additional confirmation in the fact that the IGM becomes more tenuous at lower redshift (e.g. Davé et al. 2010; McQuinn 2016), and the halo gas is expected to warm up while structure evolution progresses (e.g. Dekel & Birnboim 2006; van de Voort et al. 2011).

We stress again that our result is based on heterogeneous techniques and thus requires a confirmation with current IFU instruments at $z \sim 2$ (e.g. KCWI) and higher redshifts. Sensitive current facilities, such as MUSE and KCWI, will allow us to tackle these hypothesis with statistical and homogeneous samples, painting a clear picture for the evolution of the cool gas phase around quasars across cosmic time.

5.3 What is the combination of mechanisms powering the Lyman α emission?

To better understand the astrophysics of the Ly α emitting gas, it is key to determine the primary mechanism (or constrain the combination of mechanisms) that power the observed Ly α luminosities. While studying LABs, i.e. Ly α nebulae with area > 16 arcsec[2] and $L_{Ly\alpha} \sim 10^{43} - 10^{44}$ erg s^{-1} at $z \sim 2 - 6$, several studies have usually invoked four mechanisms to power the extended Ly α emission: (i) shocks powered by outflows (e.g. Mori, Umemura & Ferrara 2004), (ii) Ly α collisional excitation or so-called gravitational cooling radiation (e.g. Haiman, Spaans & Quataert 2000; Rosdahl & Blaizot 2012), (iii) photoionization by a central AGN or star formation (e.g. Overzier et al. 2013; Prescott et al. 2015), (iv) resonant scattering of Ly α photons from embedded sources (e.g. Dijkstra & Loeb 2008). In addition, when the Ly α emission encompasses very large scales and radio-loud objects are within the sample, additional processes could inevitably affect the observed levels, e.g. presence of multiple active sources, shocks from radio jets. All of these processes may contribute together to the observed Ly α emission, but due to the complexity to simulate them simultaneously, they are usually assessed individually. Given the similar levels of Ly α emission of LABs and the nebulosities around quasars, we here consider in turn all the aforementioned processes.

As anticipated in Section 4.3, the relatively quiescent ($\langle \sigma_{Ly\alpha} \rangle$ < 400 km s^{-1}) Ly α line of the discovered nebulosities seems to be consistent with gravitational motions within the massive haloes currently expected to host quasars. These large-scale nebulosities are thus unlikely powered by very fast outflows driven by the quasar (v_s > 1000 km s^{-1}). Due to our spatial resolution and to our analysis technique, we cannot however rule out the presence of winds on smaller scales (few kpc). Such small-scale winds could act as additional sources of ionizing photons ($F_{UV} \propto v_s^3$; e.g. Allen et al. 2008), and thus contribute to power the Ly α emission on large scales through the recombination channel. In addition, especially in the case of radio-loud objects, a collimated jet may be responsible for part of the emission. As stated in Section 4.3, we do not find evidences for violent kinematics in radio-loud objects. However, in Appendix B we show that the extended Ly α emission for the radio-loud objects with detections from the FIRST survey (spatial resolution of 5 arcsec) matches well the extent of the detected radio emission. This occurrence probably reveals a link between the Ly α emission and the synchrotron radiation usually invoked to explain the radio data (see e.g. van Ojik et al. 1996; Miley & De Breuck 2008 for the alignment seen in HzRGs).

Further, it has been routinely shown that collisional excitation of the Ly α line would require a fine tuning between the density and the temperature of the gas to reproduce the observations (e.g. Dijkstra & Loeb 2009). This is due to the exponential dependence on temperature of the collisional excitation coefficient and, being a collisional process, to the dependence on density squared in the ionized case. Thus, as it has been stressed previously in the case of Ly α nebulae (e.g. Borisova et al. 2016), collisional excitation seems to be unlikely the dominant mechanism when strong ionizing sources are present.

Indeed, the only requirement for a photoionization scenario (by the quasar or other ionizing sources) is at least a partial illumination of the cool emitting gas by the targeted AGN. As explained in Hennawi & Prochaska (2013), we can solve for two limiting
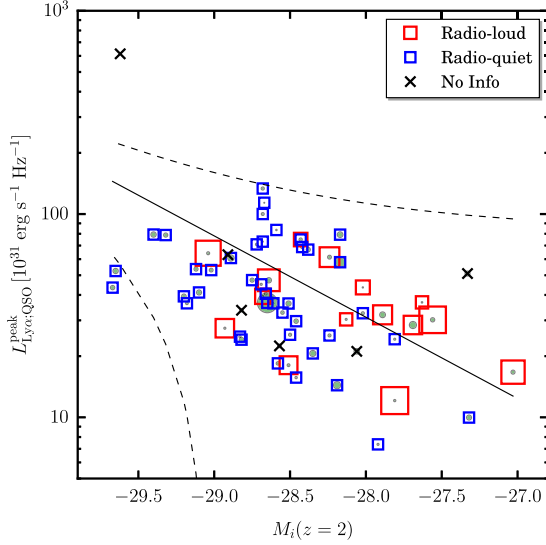
Figure 14. Plot of the peak Ly α luminosity of the targeted quasars $L_{Ly\alpha;QSO}^{peak}$ versus their absolute *i*-mag normalized at $z = 2$, $M_i(z = 2)$. As done in Fig. 11, we indicate in blue the radio-quiet systems, while in red the radio-loud objects (larger sizes = larger F_{Radio}). The crosses indicate the objects for which we do not have information on their radio flux. The green circles are drawn for all the objects and their sizes indicate a product of the area of the nebulosities and of the distance between the centre of the nebulosities and the targeted quasars (see Fig. 4). The solid and dashed black lines show a linear fit to the data and the 1 rms distance from the fit, respectively (see Section 5.3 for details).

regimes in the case of photoionization from a source with ionizing luminosity $L_{\nu_{LL}}$. In the first case, the source or the level of radiation is not strong enough to highly ionize the gas, allowing a large fraction of neutral Hydrogen to be present, i.e. the gas is optically thick to Lyman continuum photons ($N_{HI} \gg 10^{17.2}$ cm^{-2}). In this approximation the cool gas will behave like a 'mirror', converting a portion of the impinging ionizing radiation into Ly α emission. The SB thus follows the relation $SB_{Ly\alpha} \propto L_{\nu_{LL}}$. In the second case instead, the source of radiation is bright enough to keep the gas highly ionized, i.e. the gas is optically thin to Lyman continuum photons ($N_{HI} \ll 10^{17.2}$ cm^{-2}). In this regime, as anticipated in Section 5.2, it can be shown that $SB_{Ly\alpha} \propto n_H N_H$. Therefore, in the optically thin regime, the observed surface brightness should not depend on the luminosity of the targeted quasars, but only on the physical properties of the gas, i.e. the volume density n_H, and the column density N_H.

In addition, if there is enough neutral Hydrogen (i.e. the gas is optically thick in the Ly α transition, $N_{HI} \gtrsim 10^{14}$ cm^{-2}), the resonant scattering of Ly α photons emitted by the central AGN or embedded sources could be a viable process to produce extended Ly α emission (e.g. Dijkstra 2017, and references therein). In this case, the Ly α emission on large scales is due to a 'random walk' in frequency and in space of centrally produced Ly α photons. This process is caused by the absorption and consequent re-emission of photons by neutral hydrogen atoms in the quasar CGM. If scattering of Ly α photons from the quasar is the main powering mechanism, we would thus expect the observed $SB_{Ly\alpha}$ to be proportional to the Ly α emitted by the quasar, $SB_{Ly\alpha} \propto L_{Ly\alpha}^{QSO}$.

On top of this, $L_{Ly\alpha}^{QSO}$ is expected to increase with increasing quasar's $L_{\nu_{LL}}$. We show this trend in Fig. 14 where we plot the peak Ly α luminosity of each quasar $L_{Ly\alpha;QSO}^{peak}$ against their absolute *i*-mag normalized at $z = 2$. The first quantity has been calculated

by considering the maximum at the Ly α transition of the quasar's spectra shown in Fig. 2. In this plot we indicate the radio-loudness of our targets (red and blue) and we associate a green circle to each data point. This green circle indicates the product of the area of each nebulosity and the distance between the centre of the nebulosity and the targeted quasars as defined in Section 4.1.1. The data in Fig. 14 appear to be slightly correlated but a linear regression through the data points resulted in a Pearson correlation coefficient of $r_{PCC} = 0.4$, which is not statistically meaningful. We however overlay in the figure the obtained fit to the data, $L_{Ly\alpha;QSO}^{peak}/(10^{31}$ erg s Hz$^{-1}) = 12.376 \times 10^{-(M_i(z=2)+27)/2.5}$ (black solid line), together with the 1 rms distance from the fit (dahsed lines).

The aforementioned last three cases, namely photoionization of optically thick or thin gas, and resonant scattering are thus closely related, difficult to disentangle, and possibly present simultaneously. However, if any of these mechanisms plays a dominant role in the production of extended Ly α around quasars with no effect from the other mechanisms, it should naively imprint a well-defined dependence in the observed Ly α levels as explained previously. We have thus explored our data to find any of the aforementioned relations for the $SB_{Ly\alpha}$. In particular, we checked for variation of the average $SB_{Ly\alpha}$ with current ionizing luminosity, and with the peak Ly α luminosity of the targeted quasars $L_{Ly\alpha;QSO}^{peak}$. In addition, we have also looked for any dependence for the peak of the Ly α emission from the nebulosities $L_{Ly\alpha;Neb}^{peak}$ against the same quantities. Consistently with $L_{Ly\alpha;QSO}^{peak}$, we have computed the peak of the Ly α emission of the nebulosities using the spectra shown in Fig. 2.

Fig. 15 shows this test. The two left-hand panels of this figure reveal that there is no clear dependence on the quasar luminosity (spanning roughly three magnitudes) for both the $SB_{Ly\alpha}$ and for $L_{Ly\alpha;Neb}^{peak}$, with a consistent number of the nebulosities sitting at similar values around $\sim 0.4 \times 10^{-17}$ erg s^{-1} cm^{-2} arcsec^{-2} and $\sim 0.8 \times 10^{31}$ erg s^{-1} Hz^{-1}, respectively, for $SB_{Ly\alpha}$ and $L_{Ly\alpha;Neb}^{peak}$. Given the absence of any dependence with quasar luminosity, this occurrence seems to rule out a fully optically thick regime for the Ly α emitting gas, while hints to the possibility of this gas being optically thin to the ionizing radiation. This is usually found to be indeed the case if one assumes the quasar to shine on gas at distances comparable with halo scales (hundreds of kpc; Arrigoni Battaia et al. 2015, 2018). The nebulosities however are characterized by a wide scatter around the aforementioned values, especially for $SB_{Ly\alpha}$, indicating that other processes probably drive the level of the Ly α emission.

The two right-hand panels of Fig. 15 show our test for the dependence of the Ly α emission of the nebula (peak and average) with respect to the Ly α luminosity of the quasars, and thus probe a pure scattering scenario. In an attempt to verify the presence of a linear correlation within the data set, we have performed a linear fit to the data and calculated the Pearson correlation coefficient r_{PCC}. For both plots, we do not find any strong correlation, with $r_{PCC} = 0.2$ and $r_{PCC} = 0.3$ for the upper right-hand panel and lower right-hand panel, respectively. For completeness, we indicate in the plots our linear fits that resulted to be $L_{Ly\alpha;Neb}^{peak} = 0.02121 \times 10^{31}(L_{Ly\alpha;QSO}^{peak}/10^{31}[$erg s^{-1} Hz$^{-1}])$ erg s^{-1} Hz^{-1}, and $SB_{Ly\alpha}^{Nebula} = 0.00891 \times 10^{-17}(L_{Ly\alpha;QSO}^{peak}/10^{31}[$erg s^{-1} Hz$^{-1}])$erg s^{-1} cm^{-2} arcsec^{-2}. On the same plots, we also indicate the 1 rms distance from the fits with the dashed lines. The absence of clear correlations could indicate that the resonant scattering of Ly α photons is not a dominant mechanism in shaping the emission from the discovered nebulosities on the full scales encompassed by the 2σ isophote used to calculate the $SB_{Ly\alpha}$ for each nebula. This can be due to the fact that (i) additional powering mechanisms (i.e. recom-
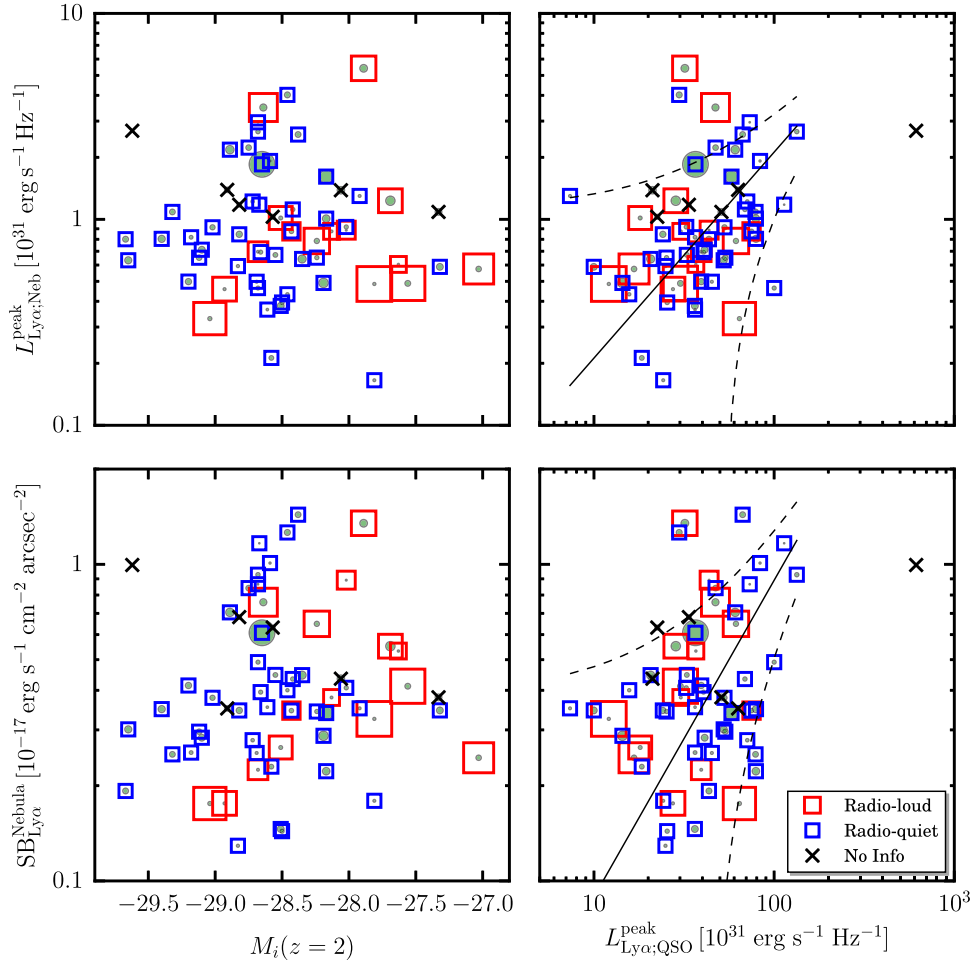
Figure 15. Lower left-hand panel: plot of the average Ly α surface brightness (SB$_{\mathrm{Ly}\alpha}$) of all the discovered nebulosities versus the absolute *i*-mag normalized at $z = 2$ for the targeted quasars. Lower right-hand panel: plot of the SB$_{\mathrm{Ly}\alpha}$ versus the peak Ly α luminosity for the targeted quasars (as derived from our MUSE data). Upper left-hand panel: plot of the peak Ly α luminosity for the discovered nebulosities versus $M_i(z = 2)$ for the targeted quasars. Upper right-hand panel: plot of the peak Ly α luminosity for the discovered nebulosities versus the peak Ly α luminosity for the targeted quasars (as derived from our MUSE data). As done in Fig. 11, we indicate in blue the radio-quiet systems, while in red the radio-loud objects (larger sizes = larger F_{Radio}). The crosses indicate the objects for which we do not have information on their radio flux. The green circles are drawn for all the objects and their sizes indicate a product of the area of the nebulosities and of the distance between the centre of the nebulosities and the targeted quasars (see Fig. 4). In the right-hand panels, the solid and dashed black lines show a linear fit to the data and the 1 rms distance from the fit, respectively (see Section 5.3 for details).

bination) and/or (ii) the variability of the quasar luminosity (e.g. Peterson et al. 2004) could have washed out a clearer dependance. The two right-hand panels of Fig. 15 and the quality of the PSF subtraction on small scales ($\sim$10 kpc) prevent us to probe the presence of a tighter relation at smaller scales. However, a signature of the relation between the Ly α emitted by the quasar and each Ly α nebula could be represented by the small velocity difference between the quasar Ly α and the nebulae themselves shown in Section 4.1. Indeed this small difference in velocity could reflect that the Ly α emission from the quasar and the peak of the nebula (always at small projected separation from the quasar) follow the same path of least resistance to escape the system in the scattering process. It is important to stress that – if resonant scattering is the only mechanism in play – only a very small fraction of the Ly α emission produced by the central quasar is needed to match the total Ly α emission observed in the detected extended nebulae, i.e. the Ly α luminosity of a nebula is $\approx$3 per cent of the peak of the Ly α emission of the quasar (average of our whole sample).

Finally, as done in Fig. 14, in Fig. 15 we associate a green circle to each data point to indicate the extent and spatial asymmetry of each nebulosity. By looking at these data points, we do not find

any correlation between the quasar ionizing luminosity and Ly α emission and the size/spatial asymmetry of the nebulae.

Summarizing, the current data at the Ly α line location suggest a scenario in which the Ly α emission is powered by a combination of photoionization of relatively optically thin gas, and resonant scattering. In addition, we cannot rule out a contribution from small-scale winds or jets in ionizing the surrounding gas distribution. We will investigate the powering mechanisms in a future work focused on additional diagnostics covered by our observations.

5.4 Insights on the observability of fast AGN winds on large scales

Our study, together with Borisova et al. (2016), has shown that we can routinely detect Ly α nebulosities for tens of kpc with fast MUSE observations, and we have argued in Section 5.3 that these nebulosities are likely powered by a combination of mechanisms dominated by the radiation of the central quasar. As already noticed in Section 4.3, the same samples result in only 1 broad Ly α nebulosity around a radio-quiet quasar out of 56 (17 + 39), and only 2

out of 17 (15 + 2) for radio-loud objects. If the broad Ly α emission is a signature of AGN winds on large scales (tens of kpc), these observations suggest a low probability of detecting them out to 50 kpc, i.e. 2 per cent and 12 per cent, respectively, for the radio-quiet and radio-loud samples.

Such low probabilities could reflect (i) a bad coupling between a relatively hot wind and the cool gas phase and/or (ii) that winds do not emit Ly α emission or emit Ly α at much fainter levels than here probed, and/or (iii) the difficulties to propagate coherent winds on large scales (tens of kpc) for long period of times[25] by the observed stochastic and episodic AGN winds generated on much smaller scales (e.g. King & Pounds 2015).

The first two options seem quite unlikely given that fast winds (with shifts and line widths $>1000\,\mathrm{km\,s^{-1}}$) on scales of tens of kpc have been reported also in cold tracers around quasars (e.g. [C II] 158 μm; Cicone et al. 2015), and the shock front should behave like a quite hard ionizing source, thus powering strong Ly α emission (e.g. Allen et al. 2008). Our snapshot observations could however be missing a broad and diffuse Ly α component.

Regarding the propagation of winds on large scales, in addition to the uncertainties in the triggering of a sustained wind, we would expect a lag between the light propagation from the quasar and the wind propagation due to the different times at which they probably switch on, and at the different speeds (light versus shock). This lag could be the cause of the observed low probabilities. Indeed, young quasars or quasars with an inefficient propagation of the wind would be characterized by a quiescent Ly α nebula (due to the quasar illumination) more extended than a turbulent region affected by the wind (if any). This scenario has been illustrated around HzRGs, where large velocity dispersion in Ly α are found within the smaller scales perturbed by the jet (FWHM > $1000\,\mathrm{km\,s^{-1}}$), but smaller velocities dispersions on larger scales beyond the radio structures or in closer regions not affected by the jet (FWHM $\sim$ $300 - 700\,\mathrm{km\,s^{-1}}$; e.g. Villar-Martín et al. 2003; Vernet et al. 2017).

If this is indeed the case, we would expect already in our data to see intermediate nebulae with large velocity dispersions on few kpc, and smaller (quiescent) velocity dispersions on larger scales. Given the current spatial resolution of our data, and the PSF subtraction algorithm used, we cannot firmly assess this scenario below approx. $1-2$ arcsec from the quasar with the current data.

We note however that several authors argued for ubiquitous extreme kinematics ($>1000\,\mathrm{km\,s^{-1}}$) around quasars on tens of kpc scales (usually <30 kpc) from low to very high redshift ($z \sim 6$), and basically along the whole electromagnetic spectrum and thus gas phases (e.g. Greene et al. 2011; Greene et al. 2014; Liu, Zakamska & Greene 2014; Brusa et al. 2015; Cicone et al. 2015; Perna et al. 2015; Rupke, Gültekin & Veilleux 2017). Such scales would correspond to about 4 arcsec at $z \sim 3$. Nevertheless, both our flux-weighted dispersion maps (Fig. 10) and the maps presented in Borisova et al. (2016; their fig. 7), do not show at face value higher widths close to the central quasars. This result would even be exacerbated if the Ly α line that we observe is broadened by scattering, as is expected. The observed Ly α line width could then be even smaller if measured through non-resonant tracers. As noted in Section 4.3, the motions within the Ly α nebulae thus seem to be consistent with gravitational motions.

This evidence thus encourage a new effort in characterizing the small-scale gas phase around quasars, while linking it to the larger scales (100 kpc) targeted in this study. The new AO system GALACSI (Stuik et al. 2006) on MUSE will be fundamen-

tal to addressing the aforementioned points, while taking into account known issues dealing with small-scale emission around bright quasars (e.g. PSF deblending; Husemann et al. 2016; Husemann & Harrison 2018). Indeed, Husemann et al. (2016) showed that previously reported spatially resolved [O III] emission-line widths on kpc scales around a sample of $z \sim 0.5$ quasars (Liu et al. 2014) are significantly narrower than the one before PSF deblending.

6 SUMMARY AND CONCLUSIONS

To characterize the CGM of massive haloes and to uncover additional ELAN, we exploit the unprecedented capabilities of the MUSE instrument on the ESO/VLT to build the 'fast' survey (45 min source^{-1}) QSO MUSEUM targeting 61 quasars at a median redshift of $z = 3.17$ ($3.03 < z < 3.46$). With quasars characterized by different radio-loudness (39 radio-quiet; 15 radio-loud; 6 with currently no radio information) and spanning roughly three magnitudes $-29.67 \leq M_i(z=2) \leq -27.03$, this survey expands previous works targeting quasars at these cosmic epochs (e.g. Borisova et al. 2016). In this work we present the results of our survey for the Ly α emission only. We plan to present the results for additional diagnostics in future works. By analysing the datacubes at the location of the Ly α transition, we thus find that

(i) After PSF and continuum subtraction, each of the targeted quasars show a Ly α nebulosity whose bulk emission is on radii $R < 50$ kpc above our detection limits (SB$_{\mathrm{Ly}\alpha}$ = 8.8×10^{-19} erg s^{-1} cm^{-2} arcsec^{-2}; 2σ in 1 arcsec^2 in a single channel of 1.25 Å), with an average surface brightness of the order of SB$_{\mathrm{Ly}\alpha} \sim 0.4 \times 10^{-17}$ erg s^{-1} cm^{-2} arcsec^{-2}. The average maximum projected distance covered by the Ly α emission from each quasar is 80 kpc. This extended Ly α emission is characterized by diverse morphologies. In particular, most of the discovered nebulae appear to be symmetric (median asymmetry $\alpha = 0.71$), while few exceptions show more elongated morphologies.

(ii) Given the diverse morphologies, the discovered Ly α nebulosities show very diverse radial profiles, which however result in a stacked profile best described by an exponential fit, SB(r) = $C_{\mathrm{e}}\exp^{-r/r_{\mathrm{h}}}$ with scale length of $r_{\mathrm{h}} = 15.7 \pm 0.5$ kpc (whole sample). This radial profile is consistent till $R \simeq 60$ kpc with the profile shown in Borisova et al. (2016), at larger radii our profile better indicates an exponential behaviour. The radio-loud sample has a slight excess in SB at 20 kpc $<R<$ 50 kpc, resulting in a tentatively larger scale length $r_{\mathrm{h}} = 16.2 \pm 0.3$ kpc, with respect to the radio-quiet sample $r_{\mathrm{h}} = 15.5 \pm 0.5$ kpc.

(iii) Down to our detection limits, the gas emitting Ly α emission covers a fraction > 30 per cent of the area around the quasars for radii $R < 50$ kpc. At larger distances, the covering fraction rapidly decrease (Fig. 7).

(iv) The peak of the Ly α emission of the nebulosities appear to be closer in redshift to the peak of the Ly α emission of the quasars $z_{\mathrm{peak\,QSO\,Ly}\alpha}$ than to the current systemic redshift of the quasars z_{systemic}. We find a median shift of the Ly α emission of $\Delta v = 782\,\mathrm{km\,s^{-1}}$, and $\Delta = 144\,\mathrm{km\,s^{-1}}$ from $z_{\mathrm{peak\,QSO\,Ly}\alpha}$ and z_{systemic}, respectively. More precise systemic redshift are needed to verify this occurrence.

(v) We discovered 27 LAEs with $F > 1.1 \times 10^{-17}$ erg s^{-1} cm^{-2} (our ≥ 80 per cent completeness level). This low detection rate agrees with the currently known luminosity functions for field LAEs (Cassata et al. 2011; Drake et al. 2017), which would predict $24 - 30$ LAEs to be found. We find fields with more than one detection that appear to be clear outliers and probably reflecting the presence of underlying overdensities, and/or effects of powering mechanisms,

---

[25] A wind with a velocity of 0.01c would require $\sim 10^7$ yr to reach 50 kpc.

e.g. chance alignment between the position of the LAE and the ionization cones of the quasars. In addition, only three fields show the presence of active companions. We note that the quasar with the larger number (2, of which 1 type-I) of active companions detected (ID 13; Arrigoni Battaia et al. 2018) also presents the more extended and brightests of the discovered Ly α nebulosities [see point (ix)].

(vi) The velocity maps obtained from the first moment of the flux distribution of the discovered Ly α nebulosities appear to be noisy and difficult to interpret as ordered motions of any kind (rotation, infall, or outflow; see also Borisova et al. 2016), though each nebulosity show peculiar structures on velocities of the order of few hundreds km s^{-1} (Fig. 9). Nebulae with larger extents than the average easily show coherent velocity structures (e.g. ID 13; Arrigoni Battaia et al. 2018). The difference in complexity between the maps of very extended nebulosities and smaller systems could be due to the resonant nature of the Ly α line that sample more turbulent regions on tens of kpc around the quasar.

(vii) All the discovered Ly α nebulosities, irrespective of the radio-loudness, are characterized by relatively quiescent kinematics ($\langle\sigma_{Ly\alpha}\rangle < 400$ km s^{-1} (or FWHM < 940 km s^{-1}). These estimates are similar to the velocity widths observed in absorption in the CGM surrounding $z \sim 2$ quasars ($\Delta v > 300$ km s^{-1}; Prochaska & Hennawi 2009; Lau et al. 2018). The motions within all these Ly α nebulae have amplitudes consistent with gravitational motions expected in dark matter haloes hosting quasars (M$_{DM} \sim 10^{12.5}$ M$_\odot$; White et al. 2012; Trainor & Steidel 2012a). This point is even strengthened by the fact that part of the velocity dispersion could be due to Ly α resonant scattering and instrument resolution (FWHM ≈ 2.83 Å or 170 km s^{-1} at 5000 Å).

(viii) The relatively quiescent Ly α nebulosities around all the 15 radio-loud quasars in our sample run counter to the two radio-loud system with $\sigma_{Ly\alpha} > 425$ km s^{-1} showed by Borisova et al. (2016). This occurrence might be driven by the higher luminosity of the Borisova's quasars for equal radio emission (see Section 4.3), and/or might reflect the probabilities of propagating a coherent AGN winds on halo scales (see Section 5.4). Note that this would also be valid in the case of radio-quiet systems (Section 5.4).

(ix) Of all the discovered Ly α nebulosities, only ID 13 (or PKS 1017 + 109) shows the extreme observed surface brightnesses and extent found in the case of $z \sim 2$ ELAN (Cantalupo et al. 2014; Hennawi et al. 2015). The ELAN around PKS 1017 + 109 has been studied in detail in Arrigoni Battaia et al. (2018). In this work we clearly show that ELAN are indeed easily detected as extended sources even with faster observations than used here (Fig. 12).

(x) The current statistics of Ly α nebulae around radio-quiet quasars at $z \sim 2$ (Arrigoni Battaia et al. 2016) suggests a lower level of Ly α emission with respect to the nebulae in the QSO MU-SEUM sample and other surveys at $z \sim 3$ (Borisova et al. 2016). Even though the current statistics at $z \sim 2$ still rely on a relatively small sample of NB data and have thus to be confirmed with ongoing campaigns using IFU instruments, we here show that such a difference would fit well with a decrease in cool halo mass in the CGM of similarly massive haloes from $z \sim 3$ to $z \sim 2$ (Dekel & Birnboim 2006). These changes in Ly α profiles can thus reflect a different balance between cool and hot gas phase at different redshifts (see discussion in Section 5.2). Future statistical surveys at different redshift are key in testing this hypothesis.

(xi) There are hints suggesting that the discovered Ly α nebulosities are powered by recombination and scattering of Ly α photons in optically thin gas (Section 5.3). The presence of fast outflows ($v_s > 1000$ km s^{-1}) on $R \sim 50$ kpc seems to be disfavoured for majority of the sample. However we cannot exclude the presence of winds or jets on scales of few kpc.

As shown by the aforementioned list of results, the large data set of QSO MUSEUM allowed us to reveal the common features characterizing the extended Ly α emission around quasars, but also to find extreme and rare outliers, i.e. the brightest and more extended nebulosities or ELAN. Given their high surface brightnesses, these objects are the ideal laboratory for the study of the astrophysics in play on halo scales.

Overall, QSO MUSEUM unveils the complexity inherent in the study of large-scale (hundreds of kpc) systems. Each of the discovered Ly α nebulosities would indeed require a detailed individual study using multiwavelength and deeper observations to firmly characterize them (e.g. geometry, environment, powering mechanisms), and understand the particular moment at which these systems are observed (e.g. ongoing AGN outflow, merger(s), quasar lifetime). Notwithstanding this complexity, our survey open the path to a better comprehension on how massive systems form and evolve along the cosmic history, and would be the benchmark for future statistical and homogeneous investigations.

REFERENCES

Alam S. et al., 2015, ApJS, 219, 12

Allen M. G., Groves B. A., Dopita M. A., Sutherland R. S., Kewley L. J., 2008, ApJS, 178, 20

Anglés-Alcázar D., Davé R., Özel F., Oppenheimer B. D., 2014, ApJ, 782, 84

Arrigoni Battaia F., Hennawi J. F., Prochaska J. X., Cantalupo S., 2015, ApJ, 809, 163

Arrigoni Battaia F., Hennawi J. F., Cantalupo S., Prochaska J. X., 2016, ApJ, 829, 3

Arrigoni Battaia F., Prochaska J. X., Hennawi J. F., Obreja A., Buck T., Cantalupo S., Dutton A. A., Macciò A. V., 2018, MNRAS, 473, 3907

Bacon R. et al., 2010, in McLean I. S., Ramsay S. K., Takami H., eds, Proc. SPIE Conf. Ser. Vol. 7735, Ground-based and Airborne Instrumentation for Astronomy III. SPIE , Bellingham, p. 274

Becker R. H., White R. L., Helfand D. J., 1994, in Crabtree D. R., Hanisch R. J., Barnes J., eds, ASP Conf. Ser. Vol. 61, Astronomical Data Analysis Software and Systems III. Astron. Soc. Pac., San Francisco, p. 165

Bergeron J., Petitjean P., Cristiani S., Arnouts S., Bresolin F., Fasano G., 1999, A&A, 343, L40

Bergeron J., Aracil B., Petitjean P., Pichon C., 2002, A&A, 396, L11

Booth C. M., Schaye J., 2009, MNRAS, 398, 53

Borisova E. et al., 2016, ApJ, 831, 39

Brooks A. M., Governato F., Quinn T., Brook C. B., Wadsley J., 2009, ApJ, 694, 396

Brusa M. et al., 2015, MNRAS, 446, 2394

Bunker A. J., Marleau F. R., Graham J. R., 1998, AJ, 116, 2086

Cai Z. et al., 2017, ApJ, 837, 71

Cai Z. et al., 2018, ApJ, 861, L3

Cantalupo S., Lilly S. J., Haehnelt M. G., 2012, MNRAS, 425, 1992

Cantalupo S., Arrigoni-Battaia F., Prochaska J. X., Hennawi J. F., Madau P., 2014, Nature, 506, 63

Cassata P. et al., 2011, A&A, 525, A143

Christensen L., Jahnke K., Wisotzki L., Sánchez S. F., 2006, A&A, 459, 717

Cicone C. et al., 2015, A&A, 574, A14

Condon J. J., Cotton W. D., Greisen E. W., Yin Q. F., Perley R. A., Taylor G. B., Broderick J. J., 1998, AJ, 115, 1693

Croft R. A. C., Weinberg D. H., Bolte M., Burles S., Hernquist L., Katz N., Kirkman D., Tytler D., 2002, ApJ, 581, 20

da Ângela J. et al., 2008, MNRAS, 383, 565

Davé R., Oppenheimer B. D., Katz N., Kollmeier J. A., Weinberg D. H., 2010, MNRAS, 408, 2051

Dekel A., Birnboim Y., 2006, MNRAS, 368, 2

Dekel A. et al., 2009, Nature, 457, 451

Di Matteo T., Khandai N., DeGraf C., Feng Y., Croft R. A. C., Lopez J., Springel V., 2012, ApJ, 745, L29

Dijkstra M., 2017, preprint (arXiv:1704.03416)

Dijkstra M., Loeb A., 2008, MNRAS, 386, 492

Dijkstra M., Loeb A., 2009, MNRAS, 400, 1109

Drake A. B. et al., 2017, MNRAS, 471, 267

Dubois Y., Pichon C., Devriendt J., Silk J., Haehnelt M., Kimm T., Slyz A., 2013, MNRAS, 428, 2885

Dutton A. A., Macciò A. V., 2014, MNRAS, 441, 3359

Erlund M. C., Fabian A. C., Blundell K. M., Celotti A., Crawford C. S., 2006, MNRAS, 371, 29

Fanidakis N., Macciò A. V., Baugh C. M., Lacey C. G., Frenk C. S., 2013, MNRAS, 436, 315

Farina E. P., Falomo R., Decarli R., Treves A., Kotilainen J. K., 2013, MNRAS, 429, 1267

Farina E. P., Falomo R., Scarpa R., Decarli R., Treves A., Kotilainen J. K., 2014, MNRAS, 441, 886

Feng Y., Di Matteo T., Croft R., Khandai N., 2014, MNRAS, 440, 1865

Fumagalli M., Cantalupo S., Dekel A., Morris S. L., O'Meara J. M., Prochaska J. X., Theuns T., 2016, MNRAS, 462, 1978

Fynbo J. U., Møller P., Warren S. J., 1999, MNRAS, 305, 849

Fynbo J. U., Thomsen B., Møller P., 2000, A&A, 353, 457

Gaskell C. M., 1982, ApJ, 263, 79

Ginolfi M., Maiolino R., Carniani S., Battaia F. A., Cantalupo S., Schneider R., 2018, MNRAS

Goerdt T., Ceverino D., 2015, MNRAS, 450, 3359

Gould A., Weinberg D. H., 1996, ApJ, 468, 462

Greene J. E., Zakamska N. L., Ho L. C., Barth A. J., 2011, ApJ, 732, 9

Greene J. E., Pooley D., Zakamska N. L., Comerford J. M., Sun A. L., 2014, ApJ, 788, 54

Gronke M., Dijkstra M., 2016, ApJ, 826, 14

Gronke M., Dijkstra M., McCourt M., Peng Oh S., 2017, A&A, 607, A71

Haiman Z., Rees M. J., 2001, ApJ, 556, 87

Haiman Z., Spaans M., Quataert E., 2000, ApJ, 537, L5

Heckman T. M., Miley G. K., Lehnert M. D., van Breugel W., 1991a, ApJ, 370, 78

Heckman T. M., Lehnert M. D., Miley G. K., van Breugel W., 1991b, ApJ, 381, 373

Hennawi J. F., Prochaska J. X., 2007, ApJ, 655, 735

Hennawi J. F., Prochaska J. X., 2013, ApJ, 766, 58(QPQ4)

Hennawi J. F. et al., 2006a, AJ, 131, 1

Hennawi J. F. et al., 2006b, ApJ, 651, 61

Hennawi J. F., Prochaska J. X., Cantalupo S., Arrigoni-Battaia F., 2015, Science, 348, 779

Hewett P. C., Wild V., 2010, MNRAS, 405, 2302

Humphrey A., Villar-Martín M., Fosbury R., Binette L., Vernet J., De Breuck C., di Serego Alighieri S., 2007, MNRAS, 375, 705

Husband K., Bremer M. N., Stanway E. R., Lehnert M. D., 2015, MNRAS, 452, 2388

Husemann B., Harrison C. M., 2018, Nat. Astron., 2, 196

Husemann B., Wisotzki L., Sánchez S. F., Jahnke K., 2013, A&A, 549, A43

Husemann B., Scharwächter J., Bennert V. N., Mainieri V., Woo J.-H., Kakkad D., 2016, A&A, 594, A44

Husemann B., Worseck G., Arrigoni Battaia F., Shanks T., 2018, A&A, 610, L7

Hu E. M., Cowie L. L., 1987, ApJ, 317, L7

Hu E. M., Songaila A., Cowie L. L., Stockton A., 1991, ApJ, 368, 28

Ivezić Ž. et al., 2002, AJ, 124, 2364

Ji S., Oh S. P., McCourt M., 2018, MNRAS, 476, 852

Kellermann K. I., Sramek R., Schmidt M., Shaffer D. B., Green R., 1989, AJ, 98, 1195

Kim Y.-R., Croft R. A. C., 2008, MNRAS, 387, 377

King A., Pounds K., 2015, ARA&A, 53, 115

Kurk J. D. et al., 2000, A&A, 358, L1

Lasker B. M., Doggett J., McLean B., Sturch C., Djorgovski S., de Carvalho R. R., Reid I. N., 1996, in Jacoby G. H., Barnes J., eds, ASP Conf. Ser. Vol. 101, Astronomical Data Analysis Software and Systems V. Astron. Soc. Pac., San Francisco, p. 88

Laursen P., Razoumov A. O., Sommer-Larsen J., 2009, ApJ, 696, 853

Lau M. W., Prochaska J. X., Hennawi J. F., 2018, ApJ, 857, 126

Leclercq F. et al., 2017, A&A, 608, A8

Lee K.-G. et al., 2014, ApJ, 795, L12

Liu G., Zakamska N. L., Greene J. E., 2014, MNRAS, 442, 1303

Lowenthal J. D., Hogan C. J., Leach R. W., Schmidt G. D., Foltz C. B., 1990, ApJ, 357, 3

Mandelker N., Padnos D., Dekel A., Birnboim Y., Burkert A., Krumholz M. R., Steinberg E., 2016, MNRAS, 463, 3921

Marino R. A. et al., 2018, ApJ, 859, 53

Mas-Ribas L., Hennawi J. F., 2018, AJ, 156, 66

McCourt M., Oh S. P., O'Leary R., Madigan A.-M., 2018, MNRAS, 473, 5407

McIntosh D. H., Rieke M. J., Rix H.-W., Foltz C. B., Weymann R. J., 1999, ApJ, 514, 40

McQuinn M., 2016, ARA&A, 54, 313

Meiksin A. A., 2009, Rev. Mod. Phys., 81, 1405

Miley G., De Breuck C., 2008, A&ARv, 15, 67

Miley G. K. et al., 2004, Nature, 427, 47

Monet D., 1998, USNO-A2.0.

Monet D. G. et al., 2003, AJ, 125, 984

Mori M., Umemura M., Ferrara A., 2004, ApJ, 613, L97

Morrissey P. et al., 2012, in McLean I. S., Ramsay S. K., Takami H., eds, Proc. SPIE Conf. Ser. Vol. 8446, Ground-based and Airborne Instrumentation for Astronomy IV. SPIE, Bellingham, p. 844613

Møller P., 2000, Messenger, 99, 31

Møller P., Fynbo J. U., 2001, A&A, 372, L57

Møller P., Warren S. J., Fall S. M., Jakobsen P., Fynbo J. U., 2000, Messenger, 99, 33

Navarro J. F., Frenk C. S., White S. D. M., 1997, ApJ, 490, 493

Nelson D., Genel S., Pillepich A., Vogelsberger M., Springel V., Hernquist L., 2016, MNRAS, 460, 2881

Nesvadba N. P. H., De Breuck C., Lehnert M. D., Best P. N., Collet C., 2017, A&A, 599, A123

Neufeld D. A., 1990, ApJ, 350, 216

North P. L., Courbin F., Eigenbrod A., Chelouche D., 2012, A&A, 542, A91

Obreja A. et al., 2018, preprint (arXiv:1804.06635)

Oke J. B., 1974, ApJS, 27, 21

Oke J. B. et al., 1995, PASP, 107, 375

Overzier R. A., Nesvadba N. P. H., Dijkstra M., Hatch N. A., Lehnert M. D., Villar-Martín M., Wilman R. J., Zirm A. W., 2013, ApJ, 771, 89

Pâris I. et al., 2017, A&A, 597, A79

Perna M. et al., 2015, A&A, 583, A72

Péroux C., Rahmani H., Arrigoni Battaia F., Augustin R., 2018, MNRAS, 479, L50

Peterson B. M. et al., 2004, ApJ, 613, 682

Prescott M. K. M., Momcheva I., Brammer G. B., Fynbo J. P. U., Møller P., 2015, ApJ, 802, 32

Prochaska J. X., Hennawi J. F., 2009, ApJ, 690, 1558

Prochaska J. X., Hennawi J. F., Simcoe R. A., 2013a, ApJ, 762, L19(QPQ5)

Prochaska J. X. et al., 2013b, ApJ, 776, 136

Prochaska J. X., Lau M. W., Hennawi J. F., 2014, ApJ, 796, 140

Rauch M. et al., 2008, ApJ, 681, 856

Richardson M. L. A., Scannapieco E., Devriendt J., Slyz A., Thacker R. J.,
    Dubois Y., Wurster J., Silk J., 2016, ApJ, 825, 83
Richards G. T., Vanden Berk D. E., Reichard T. A., Hall P. B., Schneider D.
    P., SubbaRao M., Thakar A. R., York D. G., 2002, AJ, 124, 1
Richards G. T. et al., 2006, AJ, 131, 2766
Richards G. T. et al., 2011, AJ, 141, 167
Rosario D. J. et al., 2013, A&A, 560, A72
Rosdahl J., Blaizot J., 2012, MNRAS, 423, 344
Ross N. P. et al., 2013, ApJ, 773, 14
Rudie G. C., Steidel C. C., Shapley A. E., Pettini M., 2013, ApJ, 769, 146
Rupke D. S. N., Gültekin K., Veilleux S., 2017, ApJ, 850, 40
Schlafly E. F., Finkbeiner D. P., 2011, ApJ, 737, 103
Schlegel D. J., Finkbeiner D. P., Davis M., 1998, ApJ, 500, 525
Shen S., Madau P., Guedes J., Mayer L., Prochaska J. X., Wadsley J., 2013,
    ApJ, 765, 89
Shen Y. et al., 2016, ApJ, 831, 7
Sijacki D., Springel V., Di Matteo T., Hernquist L., 2007, MNRAS, 380,
    877
Silk J., Rees M. J., 1998, A&A, 331, L1
Silva M. et al., 2018, MNRAS, 474, 3649
Stewart K. et al., 2017, ApJS, 843, 47
Stoughton C. et al., 2002, AJ, 123, 485
Stuik R., Bacon R., Conzelmann R., Delabre B., Fedrigo E., Hubin N., Le
    Louarn M., Ströbele S., 2006, New Astron. Rev., 49, 618
Tormen G., Bouchet F. R., White S. D. M., 1997, MNRAS, 286, 865
Trainor R. F., Steidel C. C., 2012a, ApJ, 752, 39
Trainor R. F., Steidel C. C., 2012b, ApJ, 752, 39
Tumlinson J. et al., 2011, Science, 334, 948
Turner M. L., Schaye J., Steidel C. C., Rudie G. C., Strom A. L., 2014,
    MNRAS, 445, 794
Tytler D., Fan X.-M., 1992, ApJS, 79, 1
van de Voort F., Schaye J., Booth C. M., Dalla Vecchia C., 2011, MNRAS,
    415, 2782
van Ojik R., Roettgering H. J. A., Carilli C. L., Miley G. K., Bremer M. N.,
    Macchetto F., 1996, A&A, 313, 25
van Ojik R., Roettgering H. J. A., Miley G. K., Hunstead R. W., 1997, A&A,
    317, 358
Venemans B. P. et al., 2007, A&A, 461, 823
Venemans B. P. et al., 2017, ApJ, 845, 154
Vernet J. et al., 2017, A&A, 602, L6
Véron-Cetty M.-P., Véron P., 2010, A&A, 518, A10
Villar-Martín M., Vernet J., di Serego Alighieri S., Fosbury R., Pentericci
    L., Cohen M., Goodrich R., Humphrey A., 2002, MNRAS, 336, 436
Villar-Martín M., Vernet J., di Serego Alighieri S., Fosbury R., Humphrey
    A., Pentericci L., 2003, MNRAS, 346, 273
Villar-Martín M., Humphrey A., De Breuck C., Fosbury R., Binette L.,
    Vernet J., 2007, MNRAS, 375, 1299
Weidinger M., Møller P., Fynbo J. P. U., 2004, Nature, 430, 999
Weidinger M., Møller P., Fynbo J. P. U., Thomsen B., 2005, A&A, 436, 825
Weilbacher P. M., Streicher O., Urrutia T., Pécontal-Rousset A., Jarno A.,
    Bacon R., 2014, in Manset N., Forshay P., eds, ASP Conf. Ser. Vol. 485,
    Astronomical Data Analysis Software and Systems XXIII. Astron. Soc.
    Pac., San Francisco, p. 451 (arXiv:1507.00034)
White M. et al., 2012, MNRAS, 424, 933
Wisotzki L. et al., 2016, A&A, 587, A98
Woods R. M., Wadsley J., Couchman H. M. P., Stinson G., Shen S., 2014,
    MNRAS, 442, 732
Zafar T. et al., 2011, A&A, 532, A51

APPENDIX A: QUASAR PSF SUBTRACTION AWAY FROM THE LYMAN α LINE

In this appendix, we show how our procedure for the subtraction of the continuum and the PSF of the quasar works in a wavelength range where no line emission is expected at the quasar redshift. At such a location we thus expect no residual emission at the levels probed by our observations. We proceed as follows. We focus on the
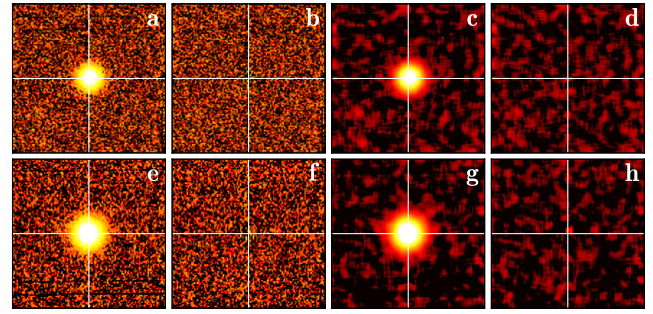
Figure A1. Quasar PSF subtraction off the Ly α line. For the first two quasars in our sample (SDSSJ 2319-1040, top; UM 24, bottom) we show 30 Å NB images centred at the quasar position (white crosshair), and at rest-frame 1260 Å for (i) the final datacube ('a' and 'e'), (ii) the final datacube after continuum and PSF subtraction ('b' and 'f'), (iii) the final datacube smoothed with a boxcar kernel of three spaxel ('c' and 'g'), and (iv) the the final datacube after continuum and PSF subtraction smoothed with a boxcar kernel of three spaxel ('d' and 'h'). Each image is 30 arcsec × 30 arcsec. Clearly there are no significant residuals that could contaminate our analysis.

portion of the final datacube at rest-frame 1260 Å, and we construct NB images by collapsing the layers within 30 Å. We then construct NB images of the same wavelength range for the continuum and PSF subtracted datacube. In Fig. A1 we show the results of this test for the first two quasars of our sample (SDSSJ 2319-1040, top; UM 24, bottom). Panel 'a' and 'e' of Fig. A1 present the central 30 arcsec × 30 arcsec of the final datacube with the clear PSF of the quasar at the centre of the image. Panels 'b' and 'f' show the same FOV, but after the continuum and PSF subtraction. The other panels show the same images but smoothed with a boxcar kernel of three spaxels. From these images, it is clear that there is no significant systematic underestimation of the PSF of the quasar, which could lead to residuals. We are thus confident that the extended Ly α emission detected around our sample is real.

APPENDIX B: COMPARISON BETWEEN RADIO EMISSION AND LY α EMISSION

In this appendix we focus on the radio-loud objects in our sample, and compare the extended Lyα emission detected in this work with the radio emission. Of the 15 radio-loud quasars, only 10 have radio data taken with a spatial resolution good enough to be compared with our observations. Indeed, five sources have been detected in the NVSS (Condon et al. 1998) which is characterized by a resolution of 45 arcsec, while 10 in the FIRST survey (Becker et al. 1994) at a resolution of 5 arcsec. The resolution of FIRST thus approaches the resolution of our observations, allowing us to qualitatively compare the two types of emission. Further, quasar with ID 17 has a FIRST detection at close separation. Here, we will investigate the nature of such source to understand if it is physically associated to the quasar.

In Fig. B1 we show the comparison between the optimally extracted images of these 11 Ly α nebulae and the S/N = 3, 10, 100 isophotes for the 1.4 GHz emission detected with FIRST (blue). Overall, the extended Ly α emission matches well the location and extent of the radio emission, with the bulk of the Ly α emission concentrated within the radio region. Exceptions to this are ID 56 and ID 17. ID 56 shows an elongated morphology towards the North in the FIRST data, suggesting the likely presence of a radio-jet. The Ly α emission however presents a different orientation, possibly
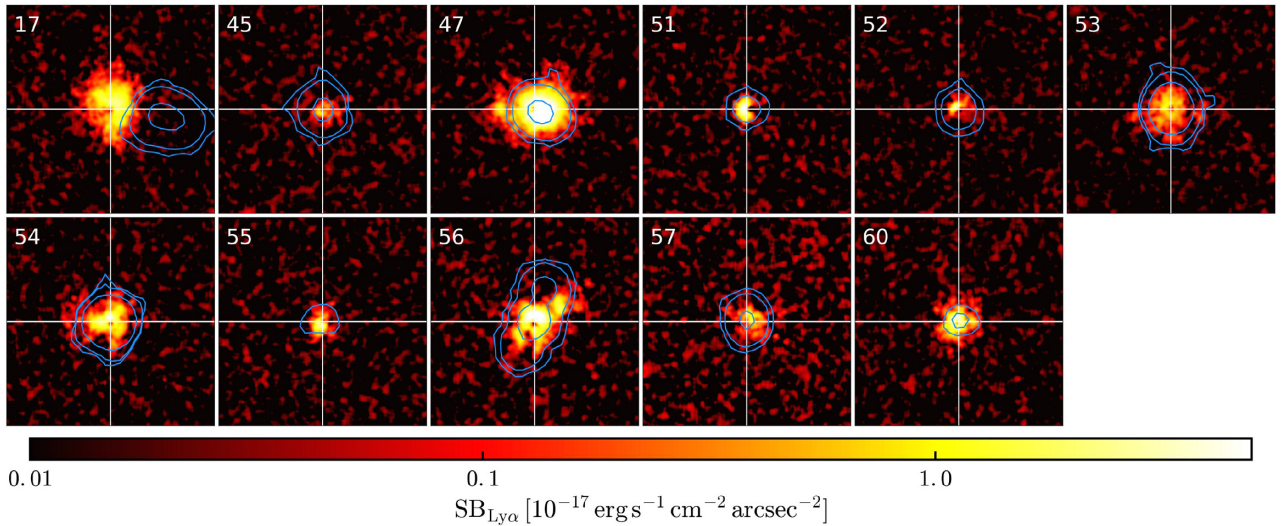
Figure B1. Comparison between the detections within the FIRST survey (Becker et al. 1994) and the discovered Ly α nebulae in our sample. We show the 50 arcsec × 50 arcsec (or approx. 380 kpc × 380 kpc) 'optimally extracted' NB maps for the targets detected in the FIRST survey with overlayed contours for S/N = 3, 10, 100 for the radio emission. Down to the current spatial resolutions and sensitivity limits, the Ly α emission and the radio emission are well matched for objects whose radio emission is centred at the quasar location. North is up, east is to the left.
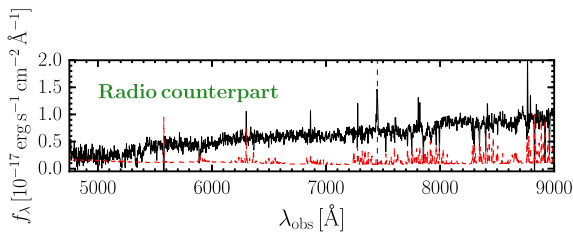
Figure B2. Spectrum of the counterpart to the radio emission at 13.5 arcsec (or 100 kpc) from the quasar with ID 17. The spectrum has been extracted from a circular region with a 2 arcsec radius at the peak of the radio emission. The red dashed line indicates the error spectrum within the same aperture. At this location some sky lines are still visible as residuals. The source is characterized by a continuum with a red upturn, and an emission line at about 7450 Å (blue dashed). Some absorption lines are tentative at the current depth (see e.g. at about 5200 and 5340 Å).

reflecting the position of a close LAE or substructure (see Fig. 5) rather than following the radio emission. ID 17 instead shows radio emission displaced by ≈13.5 arcsec (or 100 kpc) from the quasar position. We have checked the MUSE datacube at that location and found a morphologically disturbed continuum source (see Fig. 5) with a red continuum slope, and only a strong line emission at about 7450 Å (see Fig. B2). Given the presence of only one line emission and no clear absorption at the current depth, we are not able to firmly classify this object. However, it is likely that such object is not at the same redshift of the quasar with ID 17. The radio emission is thus not physically associated to this system. We thus include ID 17 in our radio-quiet sample.

All the firmly selected radio-loud objects thus show a similarity between the radio contours and the Ly α emission at the current resolutions. Future works are needed to investigate the relation between the Ly α emission, the synchrotron radiation usually invoked to explain the radio data, and other mechanisms responsible for hard photons over large scales around radio sources (e.g. extended X-rays from inverse Compton; Erlund et al. 2006). Future efforts will have to take into account the similarities in velocity dispersion and velocity shifts for the extended Ly α emission between the radio-loud and radio-quiet samples (Sections 4.3 and 5.4).

APPENDIX C: ADDITIONAL NOTES ON SOME INDIVIDUAL FIELDS

In this appendix we report (i) the information on the LAEs discovered, (ii) the spectra and coordinates for the companion AGN, for the line emitters discovered during our search for LAEs, and for the foreground or background quasars discovered. In addition, we discuss the field of Q1205-30 (or ID 58) that had been previously observed (Fynbo et al. 2000; Weidinger et al. 2004, 2005), and that thus provide a great sanity check of our analysis.

C1 The LAEs sample

In Table C1 we list the coordinates, and several properties for the discovered LAEs in the 61 fields (see Section 4.2 for the details on the LAEs selection). Note that we do not list here the LAEs around the quasar with ID 13 as those are already listed in Arrigoni Battaia et al. (2018).

C2 The continuum detected sources and the low-redshift line-emitters contaminants

In Table C2 we list the coordinates of the continuum detected sources (companions or background and foreground quasars), and of the low z line emitters that were found in our search for LAEs. The companions of ID 13 are not listed here, but they could be found in Arrigoni Battaia et al. (2018). We show the spectra of these sources in Figs C1–C9.

C3 The field of the quasar Q1205-30 (or ID 58)

The extended Ly α emission around the quasar Q1205-30 (or ID 58) has been discovered and analysed in detail by Fynbo et al. (2000) and Weidinger et al. (2004, 2005). These works relied on NB imaging and spectroscopic observations with two position angles down to

Table C1. Information on the Ly α emission for the LAEs discovered around the targeted quasars.

Object	QSO-field ID (name)	RA (J2000)	Dec (J2000)	d (arcsec)	Line centre (Å)	Redshift	$F_{Ly\alpha}$ (10^{-17} cgs)	f_λ (10^{-20} cgs)	EW$_{rest}$ (Å)	σ_v (km s^{-1})	Δv_{Neb} (km s^{-1})	Δv_{QSO} (km s^{-1})
LAE1	7 (SDSSJ1209 + 1138)	12:09:17.742	11:38:44.56	13.7	5004.91 ± 0.03	3.117 ± 0.001	1.88 ± 0.02	5.6 ± 12.8	>81	137 ± 3	− 654 ± 73	0 ± 421
LAE2	7 (SDSSJ1209 + 1138)	12:09:17.298	11:38:48.77	20.2	5004.91 ± 0.03	3.117 ± 0.001	2.76 ± 0.03	1.6 ± 18.2	>420	172 ± 2	− 654 ± 73	− 5 ± 421
LAE3	7 (SDSSJ1209 + 1138)	12:09:17.623	11:38:54.89	24.2	5023.15 ± 0.03	3.132 ± 0.001	3.02 ± 0.03	3.9 ± 14.2	>183	176 ± 2	436 ± 73	1092 ± 421
LAE4	7 (SDSSJ1209 + 1138)	12:09:16.759	11:38:47.85	24.6	5029.23 ± 0.03	3.137 ± 0.001	3.13 ± 0.03	− 9.8 ± 10.2	>74	152 ± 2	799 ± 73	1456 ± 421
LAE5	7 (SDSSJ1209 + 1138)	12:09:19.090	11:38:17.78	21.0	5012.21 ± 0.03	3.123 ± 0.001	2.53 ± 0.03	− 8.6 ± 11.4	>54	184 ± 3	− 218 ± 73	437 ± 421
LAE1	8 (UM683)	03:36:28.701	−20:19:24.97	27.0	5023.15 ± 0.03	3.132 ± 0.001	1.10 ± 0.02	− 7.9 ± 4.8	>56	112 ± 3	0 ± 73	0 ± 421
LAE2	8 (UM683)	03:36:27.484	−20:19:32.29	9.2	5023.15 ± 0.03	3.132 ± 0.001	1.35 ± 0.02	− 4.4 ± 5.1	>64	128 ± 2	0 ± 73	0 ± 421
LAE1	11 (Q-N1097.1)	02:46:35.498	−30:04:35.22	26.9	4981.82 ± 0.03	3.098 ± 0.001	2.92 ± 0.03	− 3.8 ± 10.9	>65	157 ± 2	− 73 ± 73	1470 ± 421
LAE1	20 (SDSSJ1429-0145)	14:29:02.011	−01:45:14.14	16.6	5386.63 ± 0.04	3.431 ± 0.001	3.12 ± 0.03	− 5.0 ± 8.3	>84	259 ± 3	407 ± 68	2456 ± 420
LAE1	21 (CT-669)	20:34:25.781	−35:37:36.46	11.6	5134.99 ± 0.03	3.224 ± 0.001	2.26 ± 0.04	− 4.6 ± 10.8	>50	314 ± 6	426 ± 71	355 ± 421
LAE1	26 (Q-2204-408)	22:07:33.216	−40:37:00.16	12.8	5077.85 ± 0.03	3.177 ± 0.001	31.40 ± 0.07	− 119 ± 150	>50	98 ± 4	− 143 ± 72	− 287 ± 421
LAE1	35 (CTS-C22.31)	02:04:37.863	−45:59:16.16	25.7	5162.95 ± 0.03	3.247 ± 0.001	3.66 ± 0.03	− 1.8 ± 8.2	>106	221 ± 2	71 ± 71	0 ± 421
LAE1	39 (SDSSJ0100 + 2105)	01:00:27.486	21:05:24.91	18.5	4964.80 ± 0.03	3.084 ± 0.001	6.37 ± 0.03	− 20.6 ± 11.1	>141	116 ± 1	− 951 ± 73	− 1170 ± 421
LAE1	42 (SDSSJ0219-0215)	02:19:39.060	−02:15:59.59	18.5	4907.66 ± 0.03	3.037 ± 0.001	3.63 ± 0.03	6.6 ± 17.8	>136	202 ± 2	74 ± 74	− 371 ± 422
LAE1	46 (Q2355 + 0108)	23:58:08.881	01:25:12.86	5.3	5346.52 ± 0.04	3.398 ± 0.001	3.19 ± 0.02	− 1.9 ± 11.0	>66	129 ± 1	205 ± 68	889 ± 421
LAE2	46 (Q2355 + 0108)	23:58:08.913	01:25:08.05	5.1	5357.46 ± 0.04	3.407 ± 0.001	2.73 ± 0.03	4.1 ± 18.6	>151	197 ± 3	819 ± 68	1504 ± 421
LAE1	47 (6dFJ0032-0414)	00:32:05.856	−04:14:15.02	8.5	5048.68 ± 0.03	3.153 ± 0.001	2.92 ± 0.03	− 1.0 ± 14.4	>49	167 ± 2	− 648 ± 72	− 216 ± 421
LAE1	56 (TEX1033 + 137)	10:36:26.554	13:26:56.87	6.7	4978.17 ± 0.03	3.095 ± 0.001	8.33 ± 0.03	− 12.7 ± 13.6	>149	280 ± 1	− 146 ± 73	440 ± 421
LAE2	56 (TEX1033 + 137)	10:36:27.405	13:26:42.61	12.7	4976.95 ± 0.03	3.094 ± 0.001	3.70 ± 0.03	− 6.7 ± 30.3	>30	200 ± 2	− 220 ± 73	367 ± 421
LAE3	56 (TEX1033 + 137)	10:36:27.219	13:26:49.75	5.4	4980.60 ± 0.03	3.097 ± 0.001	4.14 ± 0.03	− 0.8 ± 27.7	>36	240 ± 2	0 ± 73	587 ± 421

We list the coordinates and the distance d (arcsec) from the quasar for each LAE discovered. For the Ly α emission-line in the spectrum of each LAE, we report the line centre, the redshift, the line flux (in unit of 10^{-17} erg s^{-1} cm^{-2}), the underlying continuum flux f_λ (in unit of 10^{-20} erg s^{-1} cm^{-2} Å^{-1}), the rest-frame equivalent width, and the line width as σ_v of a Gaussian fit to the line. In addition, Δv_{Neb} and Δv_{QSO} are the velocity shift from the peak of the Ly α emission of the nebula and the systemic of the quasar targeted, respectively. The uncertainty on the latter is dominated by the uncertainty on the systemic redshift of the quasar.
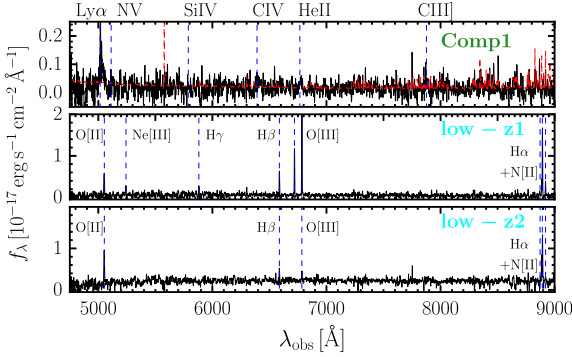

Figure C1. 1D spectrum of the companion AGN of ID 14 (or SDSSJ2100-0641), together with the two spectra of two lower redshift [O II] emitters discovered during our LAEs search. The spectra are obtained from circular apertures with 1.5 arcsec radius at the coordinates indicated in Table C2. As the companion AGN is quite faint, we plot the noise spectrum within the same aperture (red). C IV and He II emission are present at a very faint level. The location of important line emissions is indicated by blue vertical dashed lines.
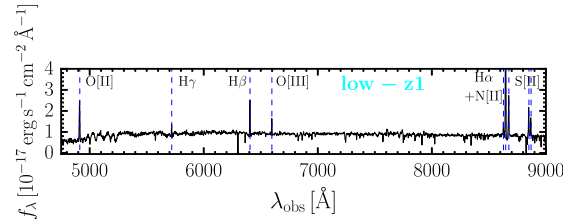

Figure C2. 1D spectrum of a lower redshift [O II] emitter discovered during our LAEs search around ID 15 (or SDSSJ1550 + 0537). The spectrum is obtained from a circular aperture with 1.5 arcsec radius at the coordinates indicated in Table C2. The location of important line emissions is indicated by blue vertical dashed lines.

surface brightness limits of about 4.4×10^{-18} erg s^{-1} cm^{-2} arcsec^{-2} (2σ; Fynbo et al. 2000), and 6×10^{-18} erg s^{-1} cm^{-2} arcsec^{-2} (2σ; at the Ly α line location, see e.g. fig. 4 in Weidinger et al. 2005), respectively, for the NB and spectroscopic data. The Ly α emission
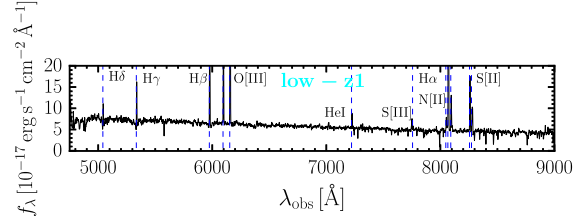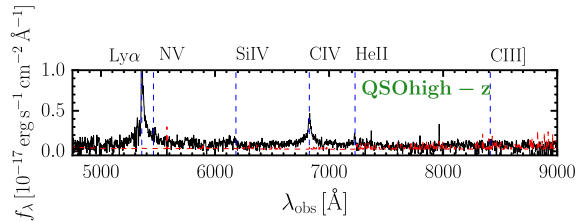
Figure C3. 1D spectrum of a lower redshift Hδ emitter discovered during our LAEs search around ID 26 (or Q-2204-408). The spectrum is obtained from a circular aperture with 1.5 arcsec radius at the coordinates indicated in Table C2. The location of important line emissions is indicated by blue vertical dashed lines.

Figure C4. 1D spectrum of a higher redshift QSO ($z = 3.407 \pm 0.006$) discovered around ID 31 (or UM670). The spectrum is obtained from a circular aperture with 1.5 arcsec radius at the coordinates indicated in Table C2. The location of important line emissions is indicated by blue vertical dashed lines. The noise spectrum within the same aperture is shown in red.
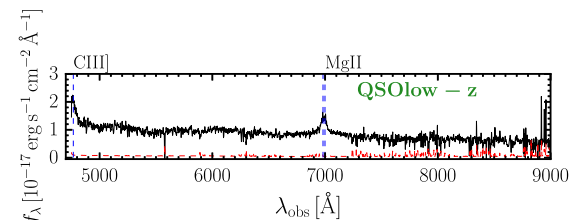

Figure C5. 1D spectrum of a lower redshift QSO ($z = 1.497 \pm 0.003$) discovered around ID 32 (or Q-0058-292). The spectrum is obtained from a circular aperture with 1.5 arcsec radius at the coordinates indicated in Table C2. The location of important line emissions is indicated by blue vertical dashed lines. The noise spectrum within the same aperture is shown in red.
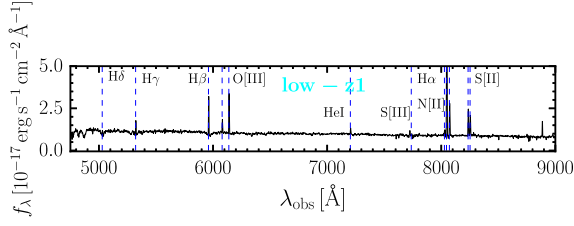
Figure C6. 1D spectrum of a lower redshift Hγ emitter discovered during our LAEs search around ID 46 (or Q2355 + 0108). The spectrum is obtained from a circular aperture with 1.5 arcsec radius at the coordinates indicated in Table C2. The location of important line emissions is indicated by blue vertical dashed lines.
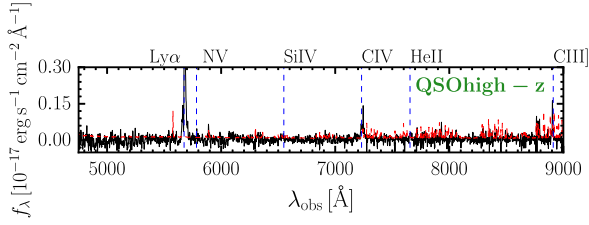

Figure C7. 1D spectrum of a higher redshift QSO ($z = 3.67 \pm 0.01$) discovered around ID 48 (or UM679). The spectrum is obtained from a circular aperture with 1.5 arcsec radius at the coordinates indicated in Table C2. The location of important line emissions is indicated by blue vertical dashed lines. The noise spectrum within the same aperture is shown in red. Note that strong sky lines are present at the location of the C IV and C III] lines, making their characterization more uncertain.
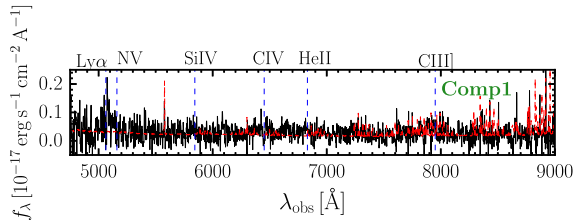

Figure C8. 1D spectrum of the very faint companion AGN of ID 53 (or SDSSJ0905 + 0410). The spectrum is obtained from a circular aperture with 1.5 arcsec radius at the coordinates indicated in Table C2. We plot the noise spectrum within the same aperture (red). The location of important line emissions is indicated by blue vertical dashed lines. There are tentative evidences for C IV and He II emissions at a very faint level, while Lyα appear to be broad.
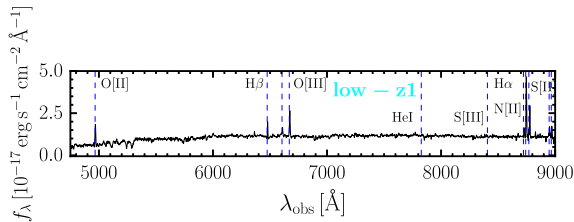

Figure C9. 1D spectrum of a lower redshift [O II] emitter discovered during our LAEs search around ID 61 (or LBQS1209 + 1524). The spectrum is obtained from a circular aperture with 1.5 arcsec radius at the coordinates indicated in Table C2. The location of important line emissions is indicated by blue vertical dashed lines.

Table C2. Coordinates of the continuum detected sources reported in Section 4.2 and shown in Fig. 5.

Object	QSO field ID (name)	RA (J2000)	Dec (J2000)
Comp1	14 (SDSSJ2100-0641)	21:00:25.459	− 06:42:05.97
low-z1	14 (SDSSJ2100-0641)	21:00:24.327	− 06:41:20.15
low-z2	14 (SDSSJ2100-0641)	21:00:26.160	− 06:41:18.82
low-z1	15 (SDSSJ1550 + 0537)	15:50:36.950	05:37:54.38
low-z1	26 (Q-2204-408)	22:07:34.069	− 40:36:33.66
QSOhigh-z	31 (UM670)	01:17:22.359	− 08:41:43.43
QSOlow-z	32 (Q-0058-292)	01:01:05.618	− 28:57:41.14
low-z1	46 (Q2355 + 0108)	23:58:10.253	01:24:53.61
QSOhigh-z	48 (UM679)	02:51:46.350	− 18:14:25.10
Comp1	53 (SDSSJ0905 + 0410)	09:05:48.546	04:09:54.17
low-z1	61 (LBQS1209 + 1524)	12:12:33.919	15:07:16.45

has been reported to extend out to about 30 kpc from the quasar using the spectroscopic data (Weidinger et al. 2004), and has been interpreted as emitted by highly ionized hydrogen falling into the quasar dark-matter halo. We can now compare our MUSE observations of the same system and assess if we recover the same values. This comparison can be regarded as a sanity check for our overall analysis technique.

First, we look at the quasar systemic redshift z_{sys} assumed in those works. Weidinger et al. (2005) reported $z_{\text{sys}} = 3.041 \pm 0.001$ based on blueshift-adjusted wavelengths of the five lines N V, Si II / O I, Si IV / O IV], C IV, and C III] (also used in Tytler & Fan 1992). In particular, they quoted in their Table 3 a redshift from C IV of 3.038 ± 0.003. Both systemic redshifts well agree with z_{sys} assumed in our work and calculated from the C IV line following Shen et al. (2016), $z_{\text{sys}} = 3.037 \pm 0.007$.

In addition, our observations are deeper than their spectroscopic data and NB imaging if individual layers are considered. Nevertheless, the MUSE observations reach similar depths to their NB if we use a 30 Å range (2σ SB limit of 4.3×10^{-18} erg s^{-1} cm^{-2} arcsec^{-2}; Table 2). Accordingly, at our depths the Lyα emission extend out to a larger maximum projected distance from the quasar: 68 kpc (Table 3). However, the profiles in the inner portion (<30 kpc) covered by both works well agree, with the profile approaching SB$_{\text{Ly}\alpha} \approx 10^{-17}$ erg s^{-1} cm^{-2} arcsec^{-2} at about 30 kpc (compare our Fig. 5 with fig. 4 in Weidinger et al. 2005). Also, we find agreement on the redshift calculated from the peak of the Lyα extended emission in close proximity of the quasar. Weidinger et al. (2005) quoted a redshift of 3.049, which is very similar to our $z_{\text{peak Ly}\alpha} = 3.047$ (Table 1). Finally, Fynbo et al. (2000) used their NB imaging data (centred at $z = 3.036$) to search for LAEs in a 315 arcsec × 315 arcsec FOV. Down to basically our same limit ($F = 1.1 \times 10^{-17}$ erg s^{-1} cm^{-2}, 5σ), they did *not* discover any LAE within the MUSE FOV in agreement with our observations. They however discover candidate LAEs at larger projected distances (see e.g. their fig. 1).

Summarizing, our MUSE observations cover in greater details the morphology and kinematics of the system of Q1205-30 (or ID 58) with respect to previous studies. Notwithstanding the slightly different depths, we find very good agreement between the works in the literature and our overall analysis. This test thus confirm the reliability of our analysis tools.

This paper has been typeset from a TEX/LATEX file prepared by the author.